Reversibility of Sea Ice and Climate under Global Change

Kyle C. Armour

A dissertation submitted in partial fulfillment of
the requirements for the degree of

Doctor of Philosophy

University of Washington

2012

LuAnne Thompson, Chair

Cecilia M. Bitz

Gerard H. Roe

Stephen D. Ellis

Program Authorized to Offer Degree:
Department of Physics

University of Washington

Abstract

Reversibility of Sea Ice and Climate under Global Change

Kyle C. Armour

Chair of the Supervisory Committee:
Professor LuAnne Thompson
School of Oceanography

We present work on several topics in physical climatology. Motivated by recent satellite observations of Arctic sea ice age, we investigate how the properties of first-year and multiyear ice regulate sea ice area and volume. Using an autoregressive model of sea ice and numerical simulation with a global dynamic-thermodynamic sea ice model that traces first-year and multiyear, we show that the sea ice mean state, variability, and sensitivity to forcing may be related to sea ice age. Ice age observations may thus offer insights into Arctic sea ice changes under warming.

We next investigate the plausibility of sea ice threshold behavior and irreversible loss under global warming, a subject of much speculation following rapid sea ice declines in recent years. Within a state-of-the-art global climate model (GCM), carbon dioxide is increased until the oceans become ice-free and subsequently decreased until the ice cover returns. We find no evidence of irreversibility over the range of simulated sea ice conditions in the summer or winter ice cover in either hemisphere.

We then shift our focus to quantification of the climate commitment—the warming that would still occur given no further emissions of greenhouse gases or aerosols. We show that elimination of emissions would cause global temperature to increase rapidly as aerosols are quickly washed from the atmosphere, and that large uncertainty in the present aerosol forcing implies large uncertainty in the climate commitment. The multi-millennial atmospheric lifetime of anthropogenic carbon dioxide causes global temperature to remain elevated for

the indefinite future, making climate change from greenhouse gas emissions irreversible on human timescales.

Finally, we propose a mechanism for the time-variation of global climate feedback as diagnosed within GCMs. Using a GCM and a low-order energy balance model, we show that the global climate feedback is fundamental related to the geographic patterns of regional feedbacks and surface warming. Its time-variation arises naturally when the pattern of surface warming evolves, activating regional feedbacks of different strengths. These findings have implications for our ability to constrain future climate changes from past and present observations, and for the quantification of climate sensitivity within models and observations.

TABLE OF CONTENTS

LIST OF FIGURES

LIST OF TABLES

ACKNOWLEDGMENTS

First and foremost I would like to express my sincerest thanks to my advisors, LuAnne Thompson and Cecilia Bitz, for fostering an environment in which I was free to learn and explore, and for critical and constructive guidance throughout. I thank Gerard Roe for teaching me to seek simple answers to complex problems, and for helping me to grow as a thinker and writer. Relatedly, I thank the CIP staff for their heroic hydration efforts during the writing of *Chap. 4*. I thank Steve Ellis for his support and guidance during formative years, and a host colleagues for engaging collaborations and many insightful discussions: Ian Eisenman, David Battisti, Dargan Frierson, Marcia Baker, Eric Steig, Eduardo Blanchard-Wrigglesworth IV, Kelly McCusker, Paul Hezel, Aaron Donohoe, Angie Pendergrass, Nicole Feldl, Yen-Ting Hwang, Stuart Evans, Brian Rose, Harry Stern, David Darr, Michael Winton, Mark Zelinka, Alex Jonko, and Jennifer Kay. I thank my many friends in my many departments for making graduate school enjoyable, and, finally, my family for their loving encouragement and support while I avoided getting a real job.

DEDICATION

PREFACE

The necessary background and motivation is presented in Chapter 1, along with a brief outline of the novel material presented herein. Chapter 2 presents an analysis of Arctic sea ice age characteristics in recent decades. Chapter 3 presents a direct test of the reversibility of sea ice loss within a fully-coupled global climate model. Chapter 4 quantifies committed climate warming from our to-date cumulative greenhouse gas emissions. Chapter 5 examines the mechanisms responsible for an apparent time-variation of climate sensitivity under transient global warming.

The chapters borrow from or are largely derived from work that has either been published or is in preparation. The list below summarizes the relationships between this thesis and various manuscripts:

Chapter 2

Kyle C. Armour, Cecilia M. Bitz, LuAnne Thompson and Elizabeth C. Hunke (2011), Controls on Arctic sea ice from first-year and multiyear ice survivability. *Journal of Climate*, 24, 2378-2390, doi: 10.1175/2010JCLI3823.1.

Chapter 3

Kyle C. Armour, Ian Eisenman, Eduardo Blanchard-Wrigglesworth IV, Kelly E. McCusker and Cecilia M. Bitz (2011) The reversibility of sea ice loss in a state-of-the-art climate model. *Geophysical Research Letters*, 38, L16705, doi: 10.1029/2011GL048739.

Chapter 4

Kyle C. Armour and Gerard H. Roe (2011) Climate commitment in an uncertain world. *Geophysical Research Letters*, 38, L01707, doi: 10.1029/2010GL045850.

Gerard H. Roe and Kyle C. Armour (2011) How sensitive is climate sensitivity? *Geophysical Research Letters*, 38, L14708, doi: 10.1029/2011GL047913.

Chapter 5

Kyle C. Armour *et al.* (2012) Time-varying climate sensitivity from regional feedbacks. *In prep.*

Chapter 1

INTRODUCTION

1.1 Summary

We present advances in two areas of physical climatology:

1. The nature of recent and future sea ice loss in a warming climate, and its potential for recovery should global climate be stabilized and returned toward its pre-industrial state.

2. The sensitivity of global climate to variations in radiative forcing, and the quantification of committed climate warming from our to-date cumulative greenhouse gas emissions.

Our work in these two areas listed above is motivated by several outstanding issues in climate prediction: unexpectedly-rapid Arctic sea ice decline in recent years has raised concerns about our ability to predict future Arctic climate and generated speculation that critical thresholds may be irreversibly crossed; and insufficient knowledge of the modern climate state precludes strong constraints on global-scale climate changes in the coming centuries. We take the overall view that navigating the complexities of the physical climate system necessitates a variety of research methods. These include the construction of idealized physical theories, numerical simulation with a range of climate models of varying levels of sophistication, and the incorporation of climate observations.

This chapter provides the essential background material required to engage meaningfully with the following chapters. For each area, there is an introduction to the key concepts and a brief review of the state of the field, providing the context in which the work developed.

We conclude this chapter with a discussion on the structure of the thesis and a brief preview of the novel results therein.

1.2 Sea ice decline and reversibility

The ongoing decline of the Arctic sea ice cover is one of the most visible signs of greenhouse-gas induced global climate change. Continuous satellite-based observations since 1979 show substantial sea ice loss in all seasons [1], consistent with a signal of rapid Arctic warming in recent decades [2]. Given the importance of sea ice in the global climate system and its emerging role on the front lines of the climate policy debate[1], a deep understanding of past and future Arctic change is essential.

The fully-coupled global climate models[2] (GCMs) participating in the Intergovernmental Panel on Climate Change (IPCC) Assessment Reports (AR) represent our most sophisticated tools for climate simulation and prediction. Comparing modeled Arctic sea ice conditions to observations reveals the observed September sea ice decline to be 'faster than forecast' [5] by the IPCC model ensemble (Fig. 1.1a). However, the simulations show considerable spread in both mean ice cover and trends: while some models show little sea ice loss at present or in the near future, others—such as the Community Climate System Model version 3 (CCSM3) [9] (highlighted in blue in Fig. 1.1a)—have ensemble members that nearly keep pace with the observations. Note that CCSM3 shows substantial biases in March Arctic sea ice cover (Fig. 1.1b) but not in September, consistent with the largely independent controls on sea ice extent in different seasons [10, 11].

Discrepancies between modeled and observed sea ice changes are not straightforward to interpret, however. Natural Arctic climate variability plays a substantial role on sea-

[1]For example, on May 15, 2008 the U. S. Department of the Interior added the polar bear to the list of threatened species under the Endangered Species Act (ESA), based on evidence that Arctic sea ice loss due to greenhouse gas emissions poses an immediate threat to the polar bear's habitat. The 'threatened' distinction protects the polar bear from activities jeopardizing its existence or adversely modifying its critical habitat. However, Secretary of the Interior Dirk Kempthorne emphasized that the ruling, "should not open the door to use of the ESA to regulate greenhouse gas emissions from automobiles, power plants, and other sources" [3], and on that same day the U. S. Fish and Wildlife Service issued a special rule that "any incidental take of polar bears resulting from an activity that occurs outside the current range of the polar bear is not a prohibited act under the ESA" [4], thus ensuring protection for greenhouse gas emitters instead.

[2]Also known as general circulation models.

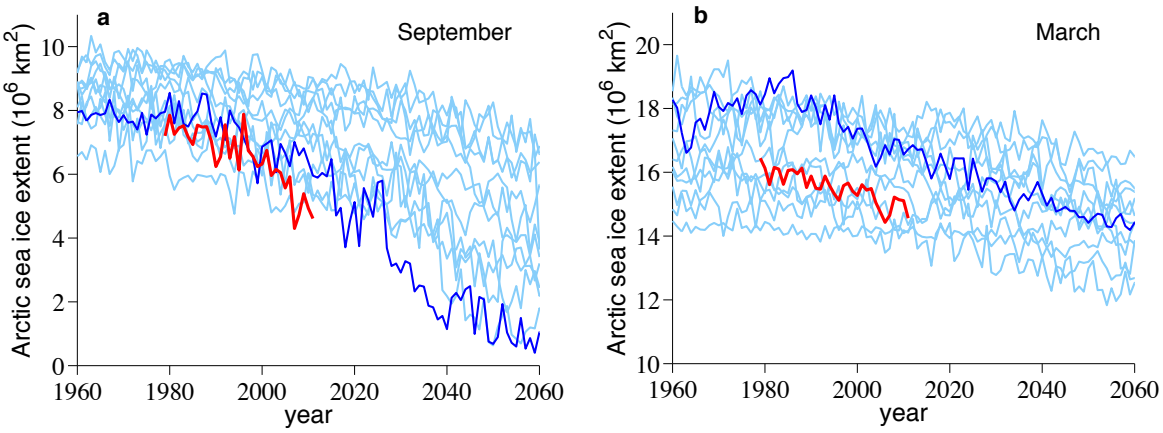

Figure 1.1: September Arctic sea ice extent from observations and climate models. a, September and **b,** March Arctic sea ice extent from 1979-2011 satellite observations [1] (red) and from the global climate models participating in the Intergovernmental Panel on Climate Change Fourth Assessment Report [6, 7] (light blue). The models are forced by 20th Century and Special Report on Emissions Scenarios A1B emissions [8], and only those with 1979-2011 September mean ice extent within ±30% of observations are shown. For reference, ice extent calculated from the Community Climate System Model version 3 (CCSM3) is shown in blue. Ice extent is defined here as the total ice area within the 15% ice concentration contour.

sonal to multi-decadal timescales [12], making direct inter-model and model-observation comparisons difficult and complicating quantification of the long-term sea ice sensitivity to global warming [13]. Moreover, models simulate a range of global warming rates, directly contributing to their variable rates of sea ice loss in Fig. 1.1 [14].

Reconciling modeled and observed sea ice conditions is further limited by the lack of continuous and long-term records of Arctic sea ice thickness. Submarine ice draft data from upward-looking sonar [15, 16] suggest an overall thinning of Arctic sea ice over 1958–2000, but these observations are limited to the particular regions and timing of individual submarine transects. From 2003–2008 the Ice, Cloud, and land Elevation Satellite (ICESat) provided laser altimetry data over much of the Arctic Ocean, from which sea ice thickness estimates show rapid thinning [17, 18]. While these data provide an important view of recent large-scale sea ice thickness trends, the second generation satellite (ICESat-2) is not scheduled for launch until 2016, ensuring a gap in observations over the coming years. More-

over, interpretation of such a short record is complicated by the long (multiyear) memory timescale and associated natural decadal variability of sea ice thickness (see *Chap. 2*).

1.2.1 Sea ice age characteristics

In light of observational limitations, alternative perspectives on changing Arctic sea ice properties under climate warming are useful. For instance, a variety of studies estimate the age of Arctic sea ice over past decades, based on direct observation or model simulation of the amount of perennial (or multiyear (MY)) and seasonal (or first-year (FY)) ice types within the total ice cover: From satellite, passive microwave sensors distinguish between FY and MY ice types based on surface emissivity data [19–21] and scatterometers determine ice types based on surface roughness characteristics [17, 18, 22]; sea ice drift models track ice parcels throughout their lifetime based on ice motion fields derived from satellite and buoy data [22–24]; and dynamic-thermodynamic sea ice models forced by observed atmospheric conditions (e.g., observed surface temperature, winds, and downwelling shortwave and longwave radiation) simulate past sea ice age and conditions [25, 26].

A common feature of the satellite-based sea ice age observations is an ambiguous 'mixed' ice category that often characterizes regions where comparable amounts of FY and MY ice exist, or where FY ice has been thickened and roughened due to rafting and ridging giving it a MY-ice-like signature. Also, each of these studies use different definitions of FY and MY ice types and sea ice age, making them difficult to compare directly. (MY ice will be defined here as that ice which has survived at least one summer melt season, and FY ice as that which has grown over a given winter—see *Chap. 2* for details). Despite these caveats, the studies robustly show a substantial reduction in the MY ice cover and an overall expansion of the FY ice cover since 1979.

Arctic sea ice age has been found to be highly correlated with several important sea ice properties, such as thickness [17, 18, 22, 24] and surface albedo [27]. The transition from a MY to seasonal ice cover thus has relevance for the sea ice mass budget, and for primary productivity in the Arctic ocean due to changes in the amount of sunlight transmitted through the ice [27]. However, the implications of sea ice age changes for future sea ice

evolution under climate warming has not been investigated outside of the observational literature. Moreover, IPCC AR4 GCMs have not kept account of sea ice age or tracked FY and MY ice types individually, instead characterizing the ice cover in terms of total ice area only. Thus, valuable opportunities exist to better understand recent sea ice conditions in terms of ice age characteristics and perhaps to validate climate models with observational data sets that have not (directly) contributed to their construction.

The importance of partitioning Arctic sea ice into its FY and MY ice components is investigated in *Chap. 2* using (i) a simple model for September sea ice area and volume, based on the survivability of FY and MY ice types, and (ii) a comprehensive dynamic-thermodynamic sea ice model (the Los Alamos sea ice model CICE, modified to keep account of FY and MY ice types separately), forced by a reconstruction of past atmospheric conditions to simulate realistic sea ice conditions over past decades.

1.2.2 Is sea ice loss reversible?

The ongoing transition to a younger, thinner and less extensive Arctic sea ice cover, and the apparent increasing rate of loss in the past decade, has generated ample speculation that Arctic sea ice may be at or near a critical threshold (or 'tipping point'), beyond which abrupt and irreversible loss of ice will occur [2, 24, 28–39]. The possible existence of such a tipping point has enormous implications for the future of the Arctic: if critical temperature thresholds were to be crossed, climate change mitigation efforts could do little to prevent an irreversible collapse of the sea ice cover, and a reduction of global temperature substantially below present may then be needed to recover the present Arctic climate.

The focus of the discussion has largely been on the summer sea ice cover, due in part to the striking September ice declines of recent years (Fig. 1.1a) and an emphasis on the role of ice-albedo feedback in the climate literature [40–42]. However, based on the results of a thermodynamic sea ice and atmosphere column model, Eisenman and Wettlaufer [43] (hereafter EW09) suggest that if an irreversible sea ice threshold exits, it is more likely to occur for the loss of winter ice than summer ice. The reason is that the stabilizing effects of nonlinear sea ice thermodynamics [44] help to mitigate the destabilizing effects of the

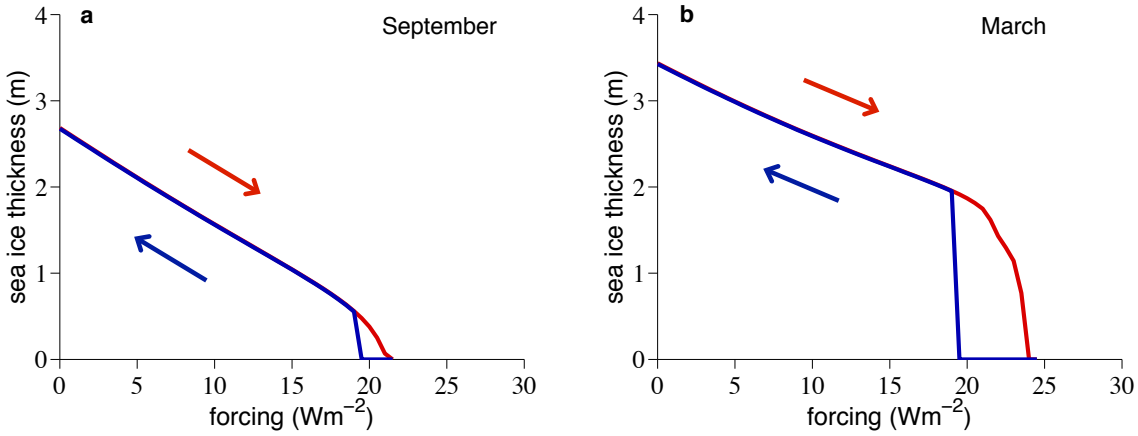

Figure 1.2: Illustration of sea ice hysteresis with respect to greenhouse gas forcing. a, September, and **b,** March sea ice thickness as a function of greenhouse gas forcing, as calculated by the EW09 thermodynamic sea ice model. Hysteresis is demonstrated by the gap between decreasing (red) and increasing (blue) sea ice thickness trajectories; beyond a critical threshold, multiple sea ice cover states under the same forcing are possible.

ice-albedo feedback, provided that enough ice grows over winter to cover the Arctic for a sufficient fraction of the year [43]. For illustrative purposes, results from the EW09 model (using the standard set of parameters) are shown in Fig. 1.2. A substantial hysteresis in winter sea ice cover occurs when climate forcing is raised and subsequently lowered, indicating multiple ice-cover states and irreversible threshold behavior. Other parameter regimes can be found that eliminate this threshold behavior, leading to a loss of sea ice that is fully reversible [43, 45].

The simplicity of the EW09 model permits evaluation and physical interpretation of the dominant sea ice feedback mechanisms via stability analysis. However, it lacks many complex features of Arctic climate that may also play a substantial role (e.g., a spatial sea ice distribution and sea ice motions, radiative cloud feedbacks, and dynamic atmospheric and oceanic heat transports), making the extension of its results to GCM simulations, and nature, difficult—though efforts to do so are ongoing [45]. Prior to the work presented here, only indirect assessments of sea ice reversibility had been made within fully-coupled GCMs. Several studies examine evidence for nonlinear threshold behavior under global

climate warming [46–49]. Alternatively, Tietsche *et al.* [50] remove the summer sea ice cover periodically throughout a climate warming simulation and report the recovery of the ice cover in subsequent years. In sum, these GCM-based studies suggest that a tipping point in summer Arctic sea ice cover is unlikely, but that a winter tipping point may be plausible, in good agreement with EW09.

Chapter 3 reports the results of a direct assessment of sea ice reversibility within CCSM3; evidence for hysteresis is examined when radiative forcing is raised until the oceans become annually ice-free and subsequently lowered until the initial ice cover returns. CCSM3 was selected for this study primarily based on familiarity from the work in *Chap. 2*. However, it is ideally suited for this task due to its tendency to exhibit periods of rapid sea ice loss, comparable to observations (Fig. 1.1), that have often been interpreted as evidence for tipping point behavior [30, 34, 37]. This work is viewed as a first step toward the goal of a broader community effort to directly assess sea ice reversibility in a range of state-of-the-art GCMs.

1.3 Global climate change and committed warming

Section 1.2 introduced the portions of this thesis that focus on the decline of Arctic sea ice under climate warming and its potential for reversibility should global climate (broadly characterized by global mean surface temperature) be stabilized and ultimately cooled. A key question is, to what extent is global climate stabilization possible? Due to the long (multi-millennial) lifetime of carbon dioxide (CO_2) in the atmosphere [51, 52] some amount of human-induced climate warming will persist well beyond the point where greenhouse gas emissions cease, making climate change (since pre-industrial) essentially irreversible on human timescales [53]. Moreover, due to the large thermal inertia of the Earth's oceans and ice sheets, global climate is presently out of equilibrium with atmospheric greenhouse gas levels, suggesting the possibility that substantial warming may yet occur [54]. The remaining portions of this thesis concern this and other questions in global climate change, focusing on what can broadly be described as global climate predictability and the reversibility of global climate change with respect to anthropogenic emissions.

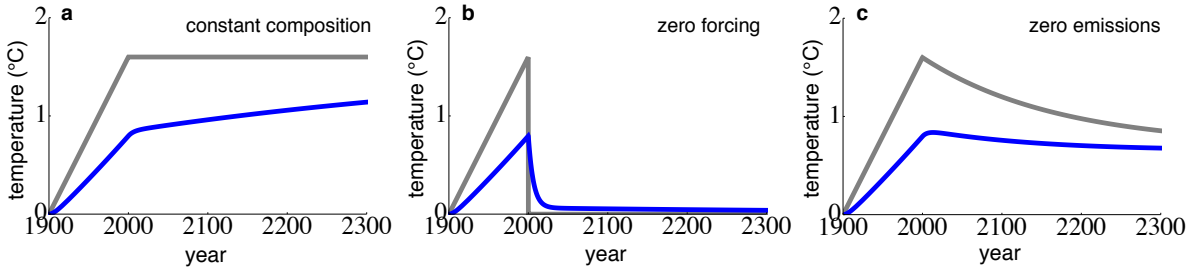

Figure 1.3: Schematic of the different measures of climate commitment. a, Constant-composition commitment, **b,** zero-forcing commitment, and **c,** zero-emissions commitment, with respect to present day. The gray line illustrates the climate forcing in each scenario, and the blue line shows the global temperature response. The difference between gray and blue curves at any given time is a measure of the temperature change required to achieve equilibrium if forcing were held fixed at that value.

1.3.1 Measures of climate commitment

The *climate commitment*—the future warming to which we are committed by human activities already undertaken—has proved a useful framework for addressing issues of climate stabilization. The climate commitment represents a fundamental metric for both science and policy: it may be regarded as the best case scenario for climate change mitigation (absent the active and deliberate management of the Earth's radiative budget) and thus provides a benchmark against which to compare all future emissions scenarios and mitigation efforts.

Several different measures of the climate commitment have been considered, as sketched in Fig. 1.3. The most commonly used measure is the *constant-composition commitment* [54–56], which represents the additional warming that would occur as the climate system comes into equilibrium with the present atmospheric composition and radiative forcing (Fig. 1.3a). Under this assumption, an additional warming of about 0.6 °C is 'in the pipeline' due to the thermal inertia of the world oceans [54–56].

An alternative measure is the *zero-forcing commitment*, which represents the transient evolution of climate if the atmospheric composition were abruptly returned to its pre-industrial level (Fig. 1.3b). In this case, global temperature would decline from present day, but remain above its pre-industrial level for decades to centuries as the heat that has built up in the deep ocean is slowly radiated away (coined 'recalcitrant' warming by Held

et al. [57]). Although this definition has received little attention, it may yet have relevance for climate engineering scenarios in which future climate forcing could be quickly reduced by a variety of possible methods.

Both of these measures of commitment, however, conflate the physical response of the climate system to past emissions with the response to the direct human influence required to maintain a constant atmospheric composition (at either present-day or pre-industrial levels). Indeed, if all anthropogenic emissions were ceased, the atmospheric composition would change according to natural processes (e.g., a partial drawdown of atmospheric CO_2 by the oceans would occur over several centuries [52,53,58]). Arguably, then, the correct measure of our present committed warming is the the *zero-emissions commitment* (Fig. 1.3c). Following zero emissions, future warming is determined by a combination of the physical inertia of the climate system and the natural evolution of climate forcing.

Studies that have considered the zero-emissions commitment [53, 59, 60] have done so only with respect to CO_2 emissions, neglecting the non-CO_2 greenhouse gases (such as methane and nitrous oxide) and aerosols. However, since the non-CO_2 greenhouse gases and aerosols contribute substantially to the modern net radiative forcing, and are removed from the atmosphere over a range of timescales (all faster than that of CO_2), they play a primary role in the future evolution of climate following zero-emissions. Moreover, the global radiative effect of aerosols[3] is the chief uncertainty in the modern climate forcing [58], and thus the cessation of aerosol emissions must imply a change in radiative forcing by an uncertain amount.

Chapter 4 quantifies the zero-emissions climate commitment, taking into consideration the full influence of all primary drivers of the modern climate and their respective changes following the cessation of emissions. Methods involve the use of global-scale energy conservation, constrained by observations of the modern climate state (these tools are introduced in *Section 1.4*), and the use of a simple upwelling-diffusive ocean energy balance model. The results have important implications for what future climate states are possible under even the most stringent climate mitigation efforts.

---

[3]Sometimes referred to as 'errorsols' (Emily Newsom, personal communication 2012).

1.4 Climate sensitivity, feedbacks and global energy balance

This section summarizes the background information necessary to describe the global-scale temperature response to variations in radiative forcing[4], for use in *Chaps. 4* and *5*. Let N be the net top-of-atmosphere (TOA) radiation flux[5], equal to the sum of absorbed shortwave radiation Q and outgoing longwave radiation F (each in units of Wm^{-2}). If over long timescales $N = Q + F = 0$, global climate is said to be in equilibrium and characterized by global-mean, annual-mean, near-surface air temperature T. In response to a sustained radiative forcing ΔR, climate must adjust until a new equilibrium is attained, at which point $\Delta R + \Delta N = 0$.

For sufficiently small climate perturbations (of a few degrees or less), the TOA radiative response can be approximated as a linear function of the surface temperature change [61–65]:

$$\begin{aligned} \Delta N &= \frac{dN}{dT}\Delta T + \mathcal{O}(\Delta T^2) \\ &= \ \lambda\ \Delta T + \mathcal{O}(\Delta T^2), \end{aligned} \tag{1.1}$$

If higher order temperature terms are neglected, λ (referred to here as the *climate feedback parameter*) relates the radiative forcing to the resulting equilibrium change in temperature:

$$\Delta R = -\lambda \Delta T. \tag{1.2}$$

λ is negative by convention and the sensitivity of climate to forcing is inversely proportional to its value.

Climate sensitivity ($\equiv\ \Delta T_{2\times}$)—defined as the equilibrium response of global-mean, annual-mean, near-surface air temperature to a doubling of carbon dioxide above pre-industrial concentrations—is a useful metric for comparing different estimates of climate change, be they instrumental, proxy, or model derived [66–72]. To the extent that λ is an unvarying measure of the relationship between ΔR and ΔT, as is often assumed, it is essentially interchangeable with climate sensitivity via

$$\Delta T_{2\times} = -\lambda^{-1}\Delta R_{2\times}, \tag{1.3}$$

[4]See the review by Roe [61] for a thorough discussion of the details. Note that while several different conventions are used here to describe global feedbacks, the underlying physics is the same.

[5]By convention, we take downward fluxes to be positive.

where $\Delta R_{2\times} \approx 3.7$ Wm^{-2} is the radiative forcing due to a doubling of carbon dioxide [73].

1.4.1 Radiative feedbacks

A well-developed description of the global climate sensitivity exists in terms of so-called *radiative feedbacks* [61–65, 74–78]. The idea is that the net TOA radiative response (ΔN) arising from a change in climate can be decomposed into the individual radiative contributions (ΔN_α) arising from changes in different components of the climate system. The usefulness of such a decomposition is the identification and quantification of the main radiative pathways by which climate adjusts to forcing, thus improving our understanding of the total climate response.

Again assuming that the TOA radiative response is linear in surface temperature, a change in an individual climate field α gives

$$\begin{aligned} \Delta N_\alpha &= \frac{dN_\alpha}{dT}\Delta T + \mathcal{O}(\Delta T^2) \\ &= \lambda_\alpha\, \Delta T + \mathcal{O}(\Delta T^2), \end{aligned} \tag{1.4}$$

where $\alpha = P$, lr, wv, c, a, corresponds to changes in temperature, lapse rate, water vapor, clouds and surface albedo, respectively. Then

$$\lambda = \sum_\alpha \lambda_\alpha = \lambda_P + \lambda_{lr} + \lambda_{wv} + \lambda_c + \lambda_a + r, \tag{1.5}$$

where the residual term r, arising from any nonlinear contributions not taken into account by the linear decomposition, is typically small [76]. The Planck feedback λ_P assumes a vertically uniform temperature change throughout the troposphere, and the lapse rate feedback λ_{lr} quantifies departures from that scenario [78].

Each λ_α may be interpreted as a feedback in the sense that it contributes an additional radiative 'nudge' (positive or negative) that is itself a function of the climate system response ΔT [61]. The definition of radiative feedbacks used here is widespread in the climate literature [65, 75–81], but equivalent definitions exist that make a more formal connection to traditional feedback analysis (i.e., related to the concept of 'gain' in control theory [61, 63]).

It is conceptually useful to identify those radiative adjustment pathways that appear more fundamental than the rest. For instance, the Planck feedback λ_P is the dominant

negative (stabilizing) feedback in Eq. (1.5); it works toward efficient global climate adjustment under forcing by increasing outgoing longwave radiation to space. In contrast, changes in surface albedo due to losses of snow and sea ice under warming has a small but positive radiative contribution to the global mean response. The shortwave radiative impact of cloud changes is the chief uncertainty in the net climate feedback [65, 78]. Locally, positive feedbacks may dominate (see *Chap. 5*), in which case attaining local equilibrium relies on the dynamical transport of heat within the climate system. In the global average, however, λ must be negative for climate to radiatively adjust and come into equilibrium with global forcing.

Within climate models, individual feedbacks can be calculated by a variety of techniques, such as the partial radiative perturbation [77] and radiative kernel methods [65, 75, 76, 78]. λ_α is often further decomposed as

$$\lambda_\alpha = \frac{\partial N_\alpha}{\partial \alpha} \frac{d\alpha}{dT}. \tag{1.6}$$

The term $\partial N_\alpha / \partial \alpha$ represents perturbations in TOA flux associated with perturbations in a particular climate field α; calculations are performed independently for each α, while all other fields are held fixed. The term $d\alpha/dT$ represents the change in climate field α per degree global temperature change; this term is often estimated as $\Delta\alpha/\Delta T$ between two simulated climate states. Feedbacks are calculated by performing this decomposition at every model grid point and integrating vertically from the surface to TOA. Global mean λ_α is given by performing an area weighted global average, and the net feedback λ is given by Eq. (1.5).

Individual feedbacks cannot be cleanly separated in climate observations, and indirect measures must instead be employed. These generally include comparison of observed variability or changes within particular components of the climate system to their counterparts within models (e.g., Hall and Qu [82] and Flanner *et al.* [83]). In this sense, climate feedbacks are inherently a modeling construct, but serve as a conceptually convenient tool to identify and quantify various mechanisms of climate change.

1.4.2 Transient evolution of global climate

Global climate variations can be described simply by conservation of energy at the global scale. Any instantaneous net top-of-atmosphere (TOA) radiative flux imbalance ($\Delta R + \Delta Q + \Delta F$) must result in a change in global heat content ($C\,\Delta T$), where C is a measure of the (time-dependent) effective heat capacity of the climate system. We drop the symbol Δ from now on, so each variable should be interpreted as an anomaly from a previous equilibrium state.

In its most general form, the equation describing the time-evolution of global surface temperature under variations in radiative forcing is then:

$$d(CT)/dt = R + Q + F. \tag{1.7}$$

$R+Q+F$ depends on climate forcing and the details of how surface temperature variations drive the TOA radiative response (*Section 1.4.1*). C depends on the details of how global heat content variations are distributed throughout the climate system. On long timescales, the global TOA energy flux is approximately equal to the rate of heat content change within the world ocean ($\equiv H$), the primary heat reservoir in the climate system [84]. Thus, from Eq. (1.1), global energy balance may be linearized to

$$H = \lambda T + R, \tag{1.8}$$

where terms of higher order in T have been neglected. A physical interpretation is that the surface components of the climate system, with mean temperature T, evolve according to a mixture of radiative forcing R and heat exchange with the ocean H. Note that as $H \to 0$, equilibrium is achieved and Eq. (1.8) reduces to Eq. (1.2). This linearization of global energy balance is useful for interpreting global-scale climate changes in both models and nature.

1.4.3 Challenges to the global feedback paradigm

It is generally assumed that the linearized global feedback framework can be consistently applied to a range of climatic variations (e.g., orbitally forced temperature variations through

Earth's history [66, 68], the climate response to volcanic eruptions [70], and the observed warming due to greenhouse gas emissions). This approach is adopted for quantifying the global climate commitment in *Chap. 4*.

However, this assumption may fail in several key ways. For instance, it has been established that climate response depends to some extent on the type of forcing applied (e.g., solar and greenhouse gas forcings drive different global mean temperature changes, per unit global mean forcing) [85–87]. It is also likely that climate feedbacks depend on the mean climate state, so that higher order terms in Eqs. (1.1) and (1.4) should be retained for large climate perturbations—though GCM-based studies have found little agreement on the magnitude or even the sign of the temperature dependence of λ [88–94]. Alternatively, the assumption that feedbacks may be decomposed and added linearly to reconstruct the net global radiative response neglects possibly-important interactions among feedbacks [61]. Exploration of the range over which this linearized global feedback framework holds is an area of ongoing research [80, 81, 95]. *Chap. 5* presents an alternative challenge to the global linear feedback paradigm: the global climate feedback λ, diagnosed by Eq. (1.8), appears to vary substantially over time in GCM simulations of transient warming.

1.5 This thesis

This thesis spans a range of topics, so each is briefly reintroduced at the beginning of its respective chapter. In *Chap. 2* we develop a simple picture of summer Arctic sea ice area and volume, in which the sea ice mean state and sensitivity to climate forcing is related to the climatological properties of FY and MY ice types. An observationally-constrained simulation of past sea ice conditions is used to understand the observed trend toward a younger, thinner sea ice cover in recent decades.

In *Chap. 3* we assess sea ice reversibility within CCSM3 by increasing atmospheric CO_2 until the Arctic Ocean becomes ice-free throughout the year and subsequently decreasing it until the initial ice cover returns. Evidence for irreversibility in the form of hysteresis is explored for the loss of summer and winter ice in both hemispheres. We report no evidence of irreversibility or multiple ice-cover states over the range of simulated sea ice conditions between the modern climate and that with an annually ice-free Arctic Ocean.

In *Chap. 4* we quantify the zero-emissions climate commitment through global energy balance considerations (Eq. (1.8)) informed by observations of the modern climate. We show that elimination of aerosol and greenhouse gas emissions would cause global temperature to increase rapidly in the following decades as aerosols are quickly washed from the atmosphere. The large uncertainty in current aerosol radiative forcing implies a large uncertainty in the climate commitment, and global temperature would remain elevated (above pre-industrial) for the indefinite future due to the long atmospheric lifetime of CO_2, making climate change from CO_2 emissions essentially irreversible on human timescales.

In *Chap. 5* we present a challenge to the global linear climate feedbacks paradigm: the global climate feedback λ appears to vary substantially over time in GCM simulations of transient warming. This time-dependence is not associated with feedback nonlinearities (i.e., higher-order temperature terms in the feedback analysis, or interactions among feedbacks), but instead arises naturally from a geographic pattern of time-independent linear feedbacks and time-evolving spatial patterns of warming in the climate system. This result has implications for our ability to constrain future warming from observations of the modern climate state, and to relate climate sensitivities estimated from different periods.

In *Chap. 6* we conclude, reflect on these results, and discuss future directions.

Chapter 2

CONTROLS ON ARCTIC SEA ICE FROM FIRST-YEAR AND MULTIYEAR ICE SURVIVABILITY

Kyle C. Armour, Cecilia M. Bitz, LuAnne Thompson and Elizabeth C. Hunke (2011) Controls on Arctic sea ice from first-year and multiyear ice survivability. *Journal of Climate*, 24, 2378-2390, doi: 10.1175/2010JCLI3823.1.

2.1 Summary

Recent observations of Arctic sea ice show that the decrease in summer ice cover over the last few decades has occurred in conjunction with a significant loss of multiyear ice. The transition to an Arctic that is populated by thinner, first-year sea ice has important implications for future trends in area and volume. Here, we develop a reduced model for Arctic sea ice with which we investigate how the survivability of first-year and multiyear ice control the mean state, variability, and trends in ice area and volume. A hindcast with a global dynamic-thermodynamic sea ice model that traces first-year and multiyear ice is used to estimate the survivability of each ice type over the period 1979-2006. These estimates of survivability, in concert with the reduced model, yield a persistence timescale of September area and volume anomalies and the characteristics of the sensitivity of sea ice to climate forcing that compare well with a fully coupled climate model. The September area is found to be nearly in equilibrium with the mean survivability of each ice type over periods longer than a few years, suggesting that the observed decline in summer sea ice cover is a clear indication of a changing climate. Keeping an account of first-year and multiyear ice area within global climate models offers a powerful way to evaluate those models with observations, and could help to constrain projections of sea ice decline in a warming climate.

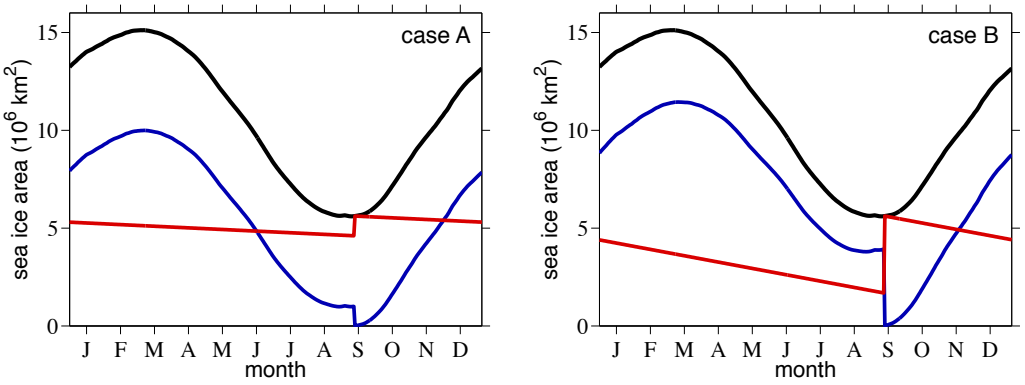

Figure 2.1: Schematic of seasonal cycle of Arctic sea ice area in terms of FY and MY ice. At the end of the melt season, defined by the day on which the total ice area (black) reaches its minimum value in September, all surviving FY ice (blue) is promoted to the MY ice (red) category. The same seasonal cycle of sea ice area is possible with different proportions of FY and MY ice (the total ice area is equal to the sum of FY and MY ice areas). In case A, FY and MY ice areas are consistent with relatively high MY ice survivability and low FY ice survivability. In case B, FY and MY ice areas are consistent with relatively low MY ice survivability and high FY ice survivability.

2.2 Introduction

Sea ice can be viewed in two distinct area categories: First-year (FY) ice that was formed since the summer minimum in the previous September and multiyear (MY) ice that has survived at least one summer melt season (Fig. 2.1). Recent observationally-constrained estimates of Arctic FY and MY ice areas and sea ice age [17, 19, 20, 22–24, 26] invite new perspectives on changing sea ice properties under climate warming.

Studies of Arctic sea ice show that the decrease in September ice area [5, 96] has been accompanied by a drastic reduction in the area of MY ice in all seasons [17, 19, 20, 22, 24]. Total ice area loss has been much larger in summer than winter (Fig. 1.1; [5,97]), consistent with the growth of FY ice to replenish much of the area that was formerly populated by MY ice in winter. Because MY ice is thicker and more able to survive the melt season [24], this transition to a younger, thinner ice pack is presumed to have important future implications.

Less obvious is the strong influence of the seasonal partitioning of FY and MY ice types on the response of summer sea ice cover to climate variability and trends. It is quite possible for a given climatological seasonal cycle of total ice area to be composed of very different

proportions of FY and MY ice. Therefore knowing the partitioning of FY and MY ice in observations and climate modeling could offer valuable information about future ice loss. To explore this concept further, consider the two possible cases illustrated in Fig. 2.1. In case A the climatological season cycle of area is almost entirely a result of expanding and retreating FY ice, while the MY ice is nearly unchanging over the year. In contrast, case B has a considerable seasonal cycle in both the FY and MY ice areas.

Now imagine that a climate perturbation one year were to cause a negative ice area anomaly at the end of summer, which would translate into a negative area anomaly in MY ice the following winter. Because winter anomalies are largely independent of summer anomalies in observations [11], FY ice would fill in much of the gap creating a positive winter FY ice area anomaly. If the mean sea ice cover is more like case A (with low FY ice survival) then we expect little of the anomalous winter FY ice to survive the following summer and the negative area anomaly from the previous summer to persist. In contrast, in case B the survival of FY ice through the end of summer is almost as high as that of MY ice, so the exact partitioning of FY and MY ice in winter matters little; both ice types are about as likely to survive the summer, and thus area anomalies decay quickly.

Systems with high persistence, like case A, recover more slowly from climate perturbations and have relatively higher variability than do systems with low persistence, like case B. Moreover, systems with longer response times have increased sensitivity to long-term climate forcing than do systems with shorter response times [44, 98]. Thus a key question is, do the characteristics of FY and MY ice within the Arctic more closely resemble case A or case B?

In this study, we investigate these basic interactions with the introduction of a reduced sea ice model for area and volume that depends on the survivability of FY and MY ice. We show how the extent to which FY and MY ice survive to summer can control the large-scale sea ice response to climate forcing, which we verify with a comprehensive sea ice model that is widely used in climate modeling. The separation of sea ice into FY and MY ice types leads to a useful framework for understanding current and future trends in Arctic sea ice and yields a novel approach for comparing models with observations in order to improve the accuracy of projections of future ice decline.

At any time of the year the total sea ice area is given by the sum of FY and MY ice areas. At the end of the melt season, here defined by the day on which the total ice area reaches its minimum value, all FY ice that has survived the summer is promoted to the MY ice category. If f_n is the area of FY ice and m_n the area of MY ice on the day of minimum ice area in September (at the instance before the promotion of FY ice to the MY category), then the total summer minimum ice area is $s_n = f_n + m_n$, where the index n denotes the year. If F_n and M_n are the areas of FY and MY ice, respectively, on the day of maximum ice area in March then the winter maximum area in year n is $W_n = F_n + M_n$.

The time evolution of the summer minimum sea ice area can be described in terms of the survivability of FY and MY ice. On average, the total ice area expands during the growth season (September to March) as FY ice grows over open water, and contracts through the melt season (March to September) as both FY and MY ice melt out (Fig. 2.2). We define the *survival ratio* of ice to be the fraction of ice area to survive over key times of the year[1]. For example, the survival ratio of FY ice over the melt season is $\alpha_n = \frac{f_n}{F_n} = \frac{f_n}{W_n - M_n}$. Because FY ice area is zero at the beginning of the growth season, its survival ratio over the growth season is undefined. The survival ratio of MY ice over the melt season is $\beta_n^m = \frac{m_n}{M_n}$ and over the growth season is $\beta_n^g = \frac{M_n}{s_{n-1}}$, where s_{n-1} is equal to the amount of MY ice at the beginning of the growth season. MY ice area decreases during the growth season—by deformation into ridges and by export to the subpolar seas, where it melts—so β_n^g is less than one. The survival ratio of MY ice from September to September (over both the growth and melt seasons) is then $\beta_n = \beta_n^g \beta_n^m = \frac{m_n}{s_{n-1}}$.

2.3 Development of the reduced sea ice model

From these definitions of FY and MY ice survival ratios, f_n and m_n can be written:

$$f_n = \alpha_n \left(W_n - \beta_n^g s_{n-1} \right) \tag{2.1}$$

and

$$m_n = \beta_n^g \beta_n^m s_{n-1}. \tag{2.2}$$

[1]Though unitless, the survival ratio is sometimes referred to as a *survival rate*.

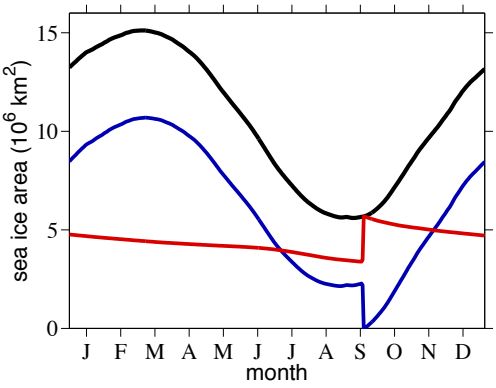

Figure 2.2: Mean seasonal cycle of FY, MY and total sea ice area over the CICE hindcast. In the simulation, FY ice (blue) is promoted to the MY ice (red) category on 15 September, at which time the total ice area (black) is near its minimum value.

The total ice area at the summer minimum is then given by the sum of FY and MY ice areas:

$$s_n = \beta_n^g \left(\beta_n^m - \alpha_n\right) s_{n-1} + \alpha_n W_n. \tag{2.3}$$

This recursion relation shows explicitly how each year's summer minimum ice area is related to that of the previous year, given the FY and MY ice survival ratios (α, β^g and β^m) and winter maximum ice area (W) in that year.

Equations (2.1)–(2.3) can be extended to describe sea ice volume. If t_n^f and t_n^m are the average thicknesses of FY and MY ice, respectively, at the summer minimum, then the total summer minimum volume is

$$\begin{aligned} v_n &= t_n^f f_n + t_n^m m_n \\ &= \beta_n^g \left(t_n^m \beta_n^m - t_n^f \alpha_n\right) s_{n-1} + t_n^f \alpha_n W_n. \end{aligned} \tag{2.4}$$

Equations (2.1)–(2.4) define the reduced sea ice model, describing the time evolution of sea ice area and volume in terms of FY and MY ice survival ratios. The relevant parameters are summarized in Table 2.1.

2.3.1 General properties of AR(1) systems

Equations (2.1)–(2.4) describe sea ice area and volume as a first-order autoregressive (AR(1)) process of the form

$$x_t = \gamma x_{t-\Delta t} + c + \epsilon_t, \tag{2.5}$$

Table 2.1: Definitions of reduced sea ice model variables and values over the CICE hindcast. All variables refer to the northern hemisphere total, and mean values and linear trends (per decade) over 1979–2006 are shown. Ice areas are in $10^6\,\mathrm{km}^2$, thicknesses in m, volumes in $10^{12}\,\mathrm{m}^3$. timescales are in years and survival ratios are unitless. The values for v and t are September averages, and the values for t^f and t^m are our best estimate over the CICE hindcast. The values of τ_s and τ_v are calculated by use of (2.17) and (2.19), respectively.

variable	definition	mean	trend
s	Total summer minimum area	5.62	−0.62
f	FY summer minimum area	2.16	−0.12
m	MY summer minimum area	3.46	−0.50
W	Total winter maximum area	15.04	−0.15
F	FY winter maximum area	10.66	0.34
M	MY winter maximum area	4.38	−0.48
α	FY melt season survival ratio	0.203	−0.017
β^g	MY growth season survival ratio	0.764	−0.007
β^m	MY melt season survival ratio	0.788	−0.028
β	MY Sep-to-Sep survival ratio ($=\beta^g\beta^m$)	0.602	−0.026
v	Total summer minimum volume	13.52	−2.87
t	Mean summer minimum thickness	2.34	−0.26
t^f	FY mean summer minimum thickness	1.5	
t^m	MY mean summer minimum thickness	3	
τ_s	Persistence timescale for September area	1.2	
τ_v	Persistence timescale for September volume	2.7	

where x_t is the value of variable x at time t, $x_{t-\Delta t}$ is its value at a previous time $(t-\Delta t)$, c is a constant, and ϵ_t is white noise (with zero mean and variance σ_ϵ^2). The parameter γ defines the memory of the system, or how much the value of x depends on its value at a previous time. See von Storch and Zwiers [99] for additional details.

The variable x can be separated into its equilibrium and perturbation components: $x_t = \overline{x} + x'_t$. This gives

$$\overline{x} = \frac{c}{1-\gamma}, \tag{2.6}$$

and

$$x'_t = \gamma x'_{t-\Delta t} + \epsilon_t. \tag{2.7}$$

The variance in x about its equilibrium value is given by

$$\sigma_x^2 = \frac{\sigma_\epsilon^2}{1-\gamma^2}. \tag{2.8}$$

The memory timescale (e-folding timescale over which perturbations in x persist, on average) is given by

$$\tau = -\frac{\Delta t}{\ln(\gamma)}. \tag{2.9}$$

Equations (2.5)–(2.9) guide our understanding of the derived relations (2.1)–(2.4) for summer minimum ice area and volume.

2.4 1979–2006 Arctic sea ice hindcast

The reduced sea ice model requires specification of the ice survival ratios in order to determine the time evolution of sea ice area and volume. Here, we use a comprehensive sea ice model that traces FY and MY ice areas in an internally consistent way to estimate the survival ratios and explore these variables. We evaluate a simulation of the Los Alamos sea ice model, CICE version 4.0 [100], to which we have added a FY ice area tracer. The model employs the same grid and much of the sea ice physics as the Community Climate System Model version 3 (CCSM3), including the elastic-viscous plastic dynamics, ice-thickness distribution, snow accumulation, and multi-layer ice and snow thermodynamics. We use the same run as described in Hunke and Bitz [26] labeled "high albedo", which uses prescribed atmospheric forcing from the Common Ocean Reference Experiments (Core) version 2 (1958–2006, [101]) with minor modifications [26]. We refer to this observationally-constrained sea ice simulation as the "CICE hindcast".

The FY ice area tracer, which is area conserving, keeps an account of all ice that grows from 15 September in one year to the next, when all FY ice is promoted to MY ice and the account is reset to zero (Fig. 2.2). We use 15 September (March) as a proxy for the true minimum (maximum) area, which is not practical to estimate on the fly in a model with synoptic-scale variability.

All of our analysis from CICE is on the "satellite era" (1979–2006). The sea ice extent in the CICE hindcast compares well with passive microwave satellite observations over this period (Fig. 2.3a). The overall magnitude and interannual variability in September and

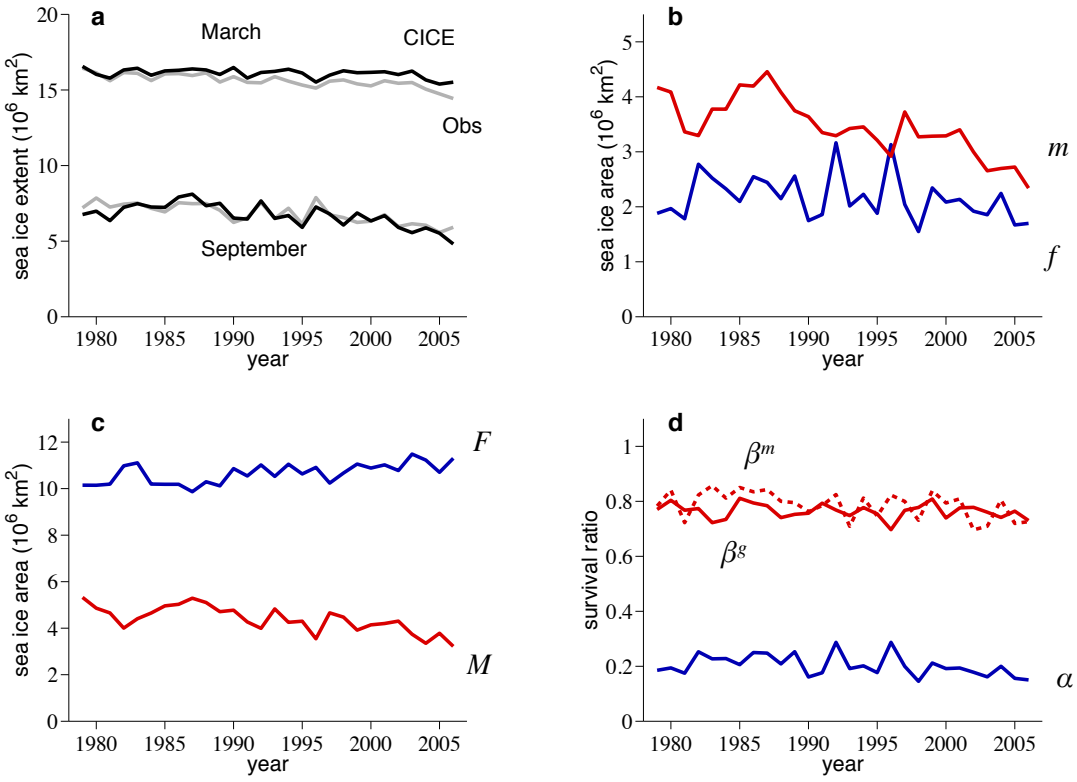

Figure 2.3: Sea ice trends over the CICE hindcast. a, September and March average ice extent from observations (gray) [1] and the CICE hindcast (black). **b,** 15 September FY (f) and MY (m) ice areas. **c,** 15 March FY (F) and MY (M) ice areas. **d,** FY (α) and MY (β^g and β^m) ice survival ratios.

March extent is captured well, as is the trend in September extent. However, the model does not reproduce the observed trend in winter—likely because the winter ice extent is highly sensitive to the ocean heat flux convergence beneath the ice [10], for which the model uses annually repeating forcing. That is, our simulation does not have ocean circulation changes, which act to enhance Arctic warming in winter [102]. The FY and MY ice conditions over the CICE hindcast are summarized in Table 2.1 and Figs. 2.2–2.5.

We also use results of present day and 1%/yr CO_2 ramped integrations of CCSM3, whose sea ice has been described previously [102, 103]. The FY ice area tracer is not yet implemented in CCSM3, so only total Arctic area and volume are used.

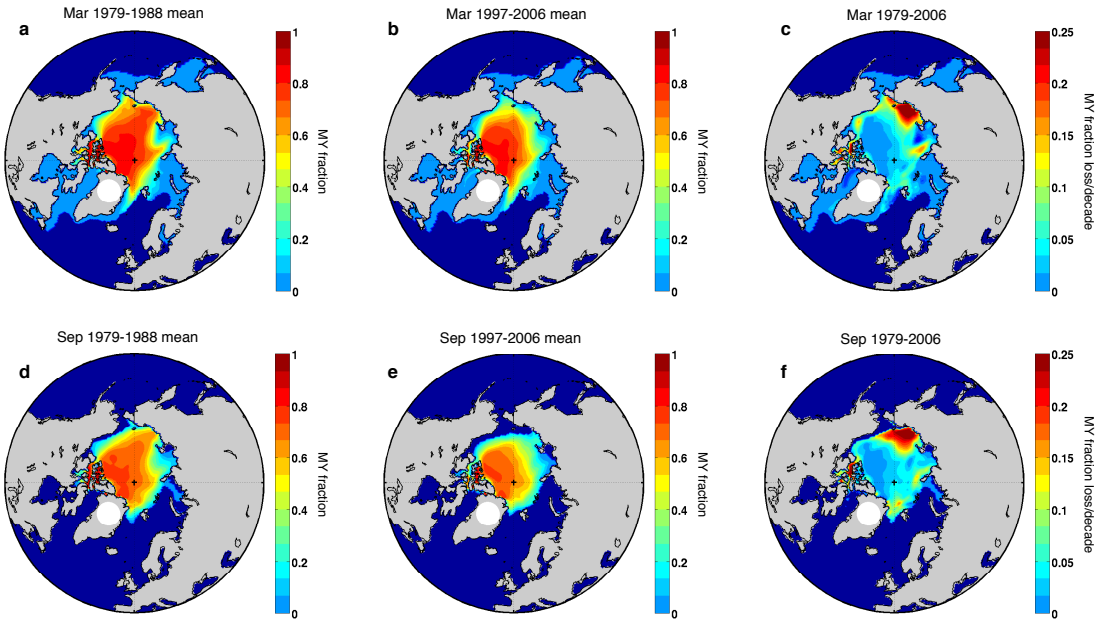

Figure 2.4: Spatial distribution of multiyear sea ice cover trends over the CICE hindcast. 15 March MY ice concentration averaged over the periods **a,** 1979–1988 and **b,** 1997–2006. **c,** March MY ice concentration linear trend. 15 September MY ice concentration averaged over the periods **d,** 1979–1988 and **e,** 1997–2006. **f,** September MY ice concentration linear trend.

2.5 Results

A number of basic relations between survival ratios and sea ice area and volume can be derived from (2.1)–(2.4) and compared with the the results of the CICE hindcast. To do this, each variable in the reduced model is decomposed into equilibrium and perturbation components. For example, the FY ice survival ratio α_n becomes $\alpha_n = \overline{\alpha} + \alpha'_n$. The equilibrium represents the mean state of the sea ice system after fully adjusting to climate forcing. The perturbation represents variability about the mean state. Later we evaluate what is a sufficient period to define the mean state.

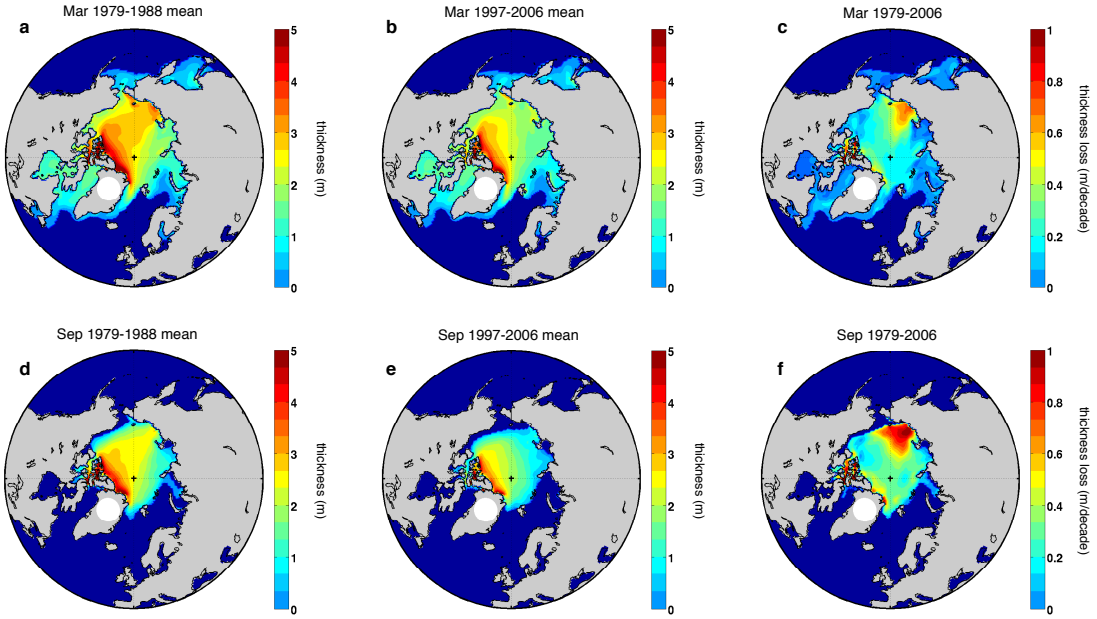

Figure 2.5: Spatial distribution of sea ice thickness trends over the CICE hindcast. 15 March ice thickness averaged over the periods **a,** 1979–1988 and **b,** 1997–2006. **c,** March ice thickness linear trend. 15 September ice thickness averaged over the periods **d,** 1979–1988 and **e,** 1997–2006. **f,** September ice thickness linear trend.

2.5.1 Equilibrium ice area

If the loss of MY ice area over the course of a year—equal to $\overline{s} - \overline{m}$ or, equivalently, $\left(1 - \overline{\beta^g}\,\overline{\beta^m}\right)\overline{s}$—is exactly balanced by the area of FY ice surviving the melt season—equal to $\overline{f}$—then the total area at the summer minimum remains unchanged and the system is in equilibrium. At equilibrium, Eqs. (2.1)–(2.3) become

$$\overline{f} = \overline{\alpha}\left(\overline{W} - \overline{\beta^g s}\right) = \left(1 - \overline{\beta^g}\,\overline{\beta^m}\right)\overline{s}, \tag{2.10}$$

$$\overline{m} = \overline{\beta^g}\,\overline{\beta^m}\overline{s}, \tag{2.11}$$

and

$$\frac{\overline{s}}{\overline{W}} = \frac{\overline{\alpha}}{1 - \overline{\beta^g}\left(\overline{\beta^m} - \overline{\alpha}\right)}. \tag{2.12}$$

The ratio in Eq. (2.12) is of particular importance because $\overline{s}$ and $\overline{W}$ can be readily estimated from passive microwave satellite data (Fig. 2.3a). A further useful relation is the ratio of

MY to FY ice at the summer minimum as it depends only on the survivability of MY ice from one summer to the next ($\overline{\beta} = \overline{\beta^g}\,\overline{\beta^m}$):

$$\frac{\overline{m}}{\overline{f}} = \frac{\overline{\beta}}{1-\overline{\beta}}. \tag{2.13}$$

We can evaluate how well these relations hold with the results of the CICE hindcast. Using 1979-2006 as an example of a mean state, we approximate the equilibrium value of each variable by its average value over that period (see Table 2.1). The left hand side of Eq. (2.12), $\overline{s}/\overline{W} = 0.374$, is in good agreement with the right hand side, $\frac{\overline{\alpha}}{1-\overline{\beta^g}\left(\overline{\beta^m}-\overline{\alpha}\right)} = 0.368$. The left hand side of Eq. (2.13), $\overline{m}/\overline{f} = 1.60$, agrees well with the right hand side, $\overline{\beta}/(1-\overline{\beta}) = 1.51$.

The previous paragraph shows that Eqs. (2.12) and (2.13) hold to within a few percent if we approximate the equilibrium of each variable by its mean over 28 years. We will show in the following section that the area is never long out of equilibrium with the ice survival ratios and the equilibrium area is well estimated by an average over a few years. In addition, we assume that the ice survival ratios are a reflection of Arctic climate, which may contain trends.

We can determine the sensitivity of $\overline{s}/\overline{W}$ to changes in the ice survival ratios by plotting its dependence on $\overline{\alpha}$ and $\overline{\beta}$ as given by Eq. (2.12). This sensitivity, given by the slope of the surface in Fig. 2.6, depends critically on the location of the mean state in $\overline{\alpha}$-$\overline{\beta}$ space (see the appendix for full representations of the slopes). In particular, for a given value of $\overline{s}/\overline{W}$, if $\overline{\beta}$ is large and $\overline{\alpha}$ is small (case A on Figs. 2.6 and 2.1) then $\overline{s}/\overline{W}$ is very sensitive to changes in the survival ratios. However, if $\overline{\beta}$ and $\overline{\alpha}$ are comparable (case B on Figs. 2.6 and 2.1) then $\overline{s}/\overline{W}$ is relatively insensitive to changes in the survival ratios. This poses a challenge for simulating changes to the summer minimum ice area in warming scenarios: there are many combinations of $\overline{\alpha}$, $\overline{\beta^g}$ and $\overline{\beta^m}$ that can provide a realistic simulation of the climatological seasonal cycle of ice area, and each combination has a unique sensitivity to a changing climate. The results of the CICE hindcast are shown in Fig. 2.2 and by point C on Fig. 2.6.

Using Eqs. (2.10) and (2.11), we can evaluate the sensitivities of $\overline{f}$ and $\overline{m}$ to changes in the survival ratios (see the appendix). These sensitivities reflect that if $\overline{\alpha}$ decreases, then $\overline{f}$ decreases because less FY ice survives the summer melt season and $\overline{m}$ decreases because

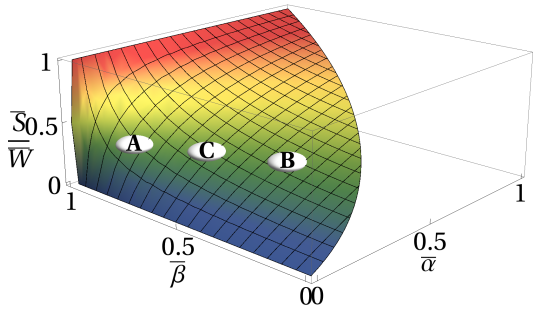

Figure 2.6: Sensitivity of September sea ice cover to changing FY and MY ice survivability. Plot of $\frac{\overline{s}}{\overline{W}} \approx \frac{\overline{\alpha}}{1-\overline{\beta}+\overline{\alpha}\sqrt{\overline{\beta}}}$, which is Eq. (2.12) under the approximation $\overline{\beta^g} \approx \overline{\beta^m} \approx \sqrt{\overline{\beta^g}\,\overline{\beta^m}} = \sqrt{\overline{\beta}}$ (from Table 2.1, the survival ratios of MY ice through the growth season and melt season are similar), over the regime $\overline{\alpha} < \sqrt{\overline{\beta}}$. Points **A-C** denote different regions on the surface with the same value of $\overline{s}/\overline{W}$ but different values of $\overline{\alpha}$ and $\overline{\beta}$. Point **C** is the result of the CICE hindcast 28 year mean ($\overline{\alpha} = 0.203$ and $\overline{\beta} = 0.602$). Point **A** is $\overline{\alpha} \approx 0.1$ and $\overline{\beta} \approx 0.82$. Point **B** is $\overline{\alpha} \approx 0.3$ and $\overline{\beta} \approx 0.36$.

less FY ice is available to replenish the MY ice category each year. If $\overline{\beta^g}$ or $\overline{\beta^m}$ decreases, then $\overline{m}$ decreases because less MY ice survives the growth or melt seasons, respectively, but there is an increase in $\overline{f}$ because more of the Arctic becomes available for FY ice to grow over the winter (Figs. 2.3c and 2.4). Over the CICE hindcast, the FY and MY ice survival ratios decrease at comparable rates, resulting in a large reduction of MY ice area while September FY ice area remains relatively constant (Table 2.1 and Fig. 2.3b). These trends in FY and MY ice areas are consistent with recent observations [17].

The results of the CICE hindcast indicate that the Arctic sea ice system is in a regime where the total summer minimum ice area $\overline{s}$ is more sensitive to changes in $\overline{\beta^m}$ than in $\overline{\beta^g}$ (see the appendix and consider values from Table 2.1). This arises because FY ice may grow in place of the MY ice that is lost during the growth season. Also, $\overline{s}$ is more sensitive to changes in $\overline{\alpha}$ than in either $\overline{\beta^g}$ or $\overline{\beta^m}$ (note the location of point C on Fig. 2.6). This will become increasingly so as the ratio of MY ice area to FY ice area continues to decrease in a warming climate.

2.5.2 Equilibrium ice volume

By use of the reduced model, we can relate trends in ice area to trends in ice volume. In equilibrium, the average sea ice thickness at the summer minimum is

$$\begin{aligned} \overline{t} &= \frac{\overline{v}}{\overline{s}} \\ &= \overline{t^f}\left(1 - \overline{\beta^g}\,\overline{\beta^m}\right) + \overline{t^m}\overline{\beta^g}\,\overline{\beta^m}, \end{aligned} \tag{2.14}$$

and the ice volume is

$$\overline{v} = \frac{\overline{t^f}\,\overline{\alpha}\,\overline{W}}{1 - \overline{\beta^g}\left(\frac{\overline{t^m}}{\overline{t}}\overline{\beta^m} - \frac{\overline{t^f}}{\overline{t}}\overline{\alpha}\right)}. \tag{2.15}$$

Equation (2.14) shows that the average ice thickness $\overline{v}/\overline{s}$ is independent of $\overline{\alpha}$. This can equivalently be expressed as $\frac{1}{\overline{v}}\frac{\partial \overline{v}}{\partial \overline{\alpha}} = \frac{1}{\overline{s}}\frac{\partial \overline{s}}{\partial \overline{\alpha}}$, meaning that the fractional decline in volume is equal to the fractional decline in area under decreasing $\overline{\alpha}$. However, for a decrease in either $\overline{\beta^g}$ or $\overline{\beta^m}$ there will be a larger fractional decline in volume than in area provided that $\overline{t^m} > \overline{t^f}$ (see the appendix). This arises from the larger area loss of the thick, MY ice than the loss of total ice area under a decrease in either of the MY ice survival ratios. Additionally, $\overline{v}$ can decrease due to thinning of ice within the FY and MY categories (Fig. 2.5), while $\overline{s}$ is unchanged with respect to changes in $\overline{t^f}$ and $\overline{t^m}$ (at constant FY and MY ice survivability). We therefore expect a larger percent decrease in volume than area under rising greenhouse gas scenarios. This is seen in the CICE hindcast (from Table 2.1, v declines at an average rate of -21%/decade while s declines at -11%/decade, with respect to their average values over 1979-2006) as well as in simulations with GCMs (over the 70 years of CO_2 ramping in the CCSM3 simulation, shown in Fig. 2.7, v declined at an average rate of -16%/decade while s declined at -12%/decade, with respect to their average values over that period).

2.5.3 Interannual variability in ice area

We now consider how the mean survivabilities of FY and MY ice—which set the total summer ice area and partitioning between ice types—control the response of the system to interannual climate variability. The deviation of summer minimum ice area from its

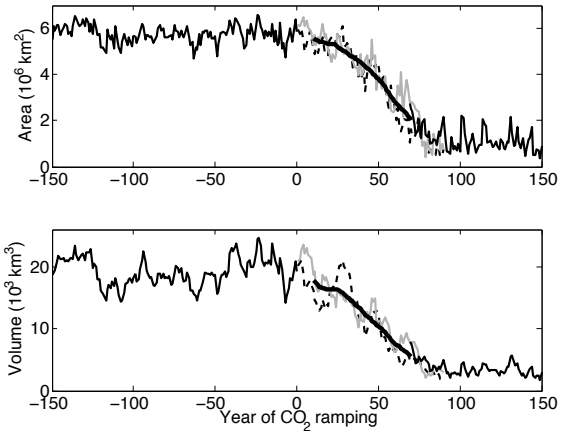

Figure 2.7: Projected September sea ice area and volume trends under increasing CO_2. Arctic September sea ice area and volume from a CCSM3 simulation with 1% per year CO_2 ramping between the years 0 and 70. Two runs are shown over the years 0 to 70. To illustrate the trends under CO_2 ramping, the two runs have been averaged together over this period, and a 20-year running mean has been applied to this average (thick black line).

equilibrium value in year n is

$$\begin{aligned} s'_n &= s_n - \overline{s} \\ &\approx \overline{\beta^g}\left(\overline{\beta^m} - \overline{\alpha}\right) s'_{n-1} + \left(\overline{W} - \overline{\beta^g}\,\overline{s}\right)\alpha'_n \\ &\quad + \overline{\beta^g}\overline{s}\beta_n^{m'} + \left(\overline{\beta^m} - \overline{\alpha}\right)\overline{s}\beta_n^{g'} + \overline{\alpha}W'_n, \end{aligned} \tag{2.16}$$

where we have dropped terms that are second order in the perturbed quantities[2]. The persistence of area perturbations from one summer s'_{n-1} to the next summer s'_n is regulated by the quantity multiplying s'_{n-1} in Eq. (2.16), which is large when $\overline{\beta^g}$ and $\overline{\beta^m}$ are large and when $\overline{\alpha}$ is small. Thus persistence is high when FY ice survivability and MY ice survivability are different from one another (case A in Figs. 2.1 and 2.6) and low when they are comparable (case B in Figs. 2.1 and 2.6).

[2]Using the parameters estimated from the CICE hindcast, the terms that are second order in the perturbations are an order of magnitude smaller than the first order terms. While we expect a similar result for the observed sea ice system and GCM simulations of the modern climate, it should be tested in those cases. Because the variability and mean of each variable could change over time, the relative importance of the second order terms must be further evaluated within GCMs under warming scenarios.

To the extent that the perturbations in the survival ratios and the winter maximum area are described by white noise, Eq. (2.16) is approximately an AR(1) process. Then the characteristic response timescale, defined as the e-folding time over which the ice retains information about a perturbation in the summer minimum area, is given by

$$\tau_s = -\frac{1 \text{ year}}{\ln \overline{\beta^g}\left(\overline{\beta^m} - \overline{\alpha}\right)}. \tag{2.17}$$

For the CICE hindcast, this timescale as calculated from the average survival ratios (Table 2.1) is 1.2 years. Because τ_s is relatively small, the area is never out of equilibrium for long and averaging over only a few years is a sufficient approximation to the current equilibrium state.

This timescale can also be estimated directly from the time series of the minimum ice area from the CICE hindcast. If we assume that the minimum area is an AR(1) process then $\tau_s \approx -\frac{1 \text{ year}}{\ln(R)}$, where $R = 0.24$ is the autocorrelation at lag 1 year of the linearly detrended time series. This gives $\tau_s \approx 0.7$ years, which differs slightly from our first estimate because in Eq. (2.17) we ignored the small correlations among the perturbations[3]. Both estimates of the timescale indicate low year-to-year memory in the minimum sea ice area, consistent with observations [11]. We note that although our analysis is limited to the period 1979-2006, our estimate of memory is qualitatively consistent with the observed September ice extent in more recent years: following the record minimum extent in 2007, subsequent years (2008–2010) show a slight recovery and are consistent with variability about the long-term linear trend.

We can determine which variables most influence the year-to-year perturbations in the summer minimum ice area by considering the correlation of each variable in Eq. (2.16) with s'_n. After linearly detrending the time series of each variable in the CICE hindcast, we find that W'_n is correlated at $R = 0.1$, $\beta_n^{g'}$ at $R = 0.02$, and s'_{n-1} at $R = 0.24$. Because α'_n and $\beta_n^{m'}$ are significantly correlated with each other ($R = 0.63$), we cannot determine which is most responsible for the variations in s'_n. However, together they account for nearly all of

[3]Statistically insignificant correlations arise between $\beta_n^{m'}$ and s'_{n-1} ($R = -0.22$) and between α'_n and s'_{n-1} ($R = -0.17$). The 95% confidence interval on the timescale as calculated from the lagged autocorrelation of the September area time series is 0 years to 1.7 years, which is consistent with our estimate from Eq. (2.17).

the variance in the summer minimum ice area, with α'_n correlated with s'_n at $R = 0.82$ and $\beta_n^{m'}$ at $R = 0.75$. The survival ratios α'_n and $\beta_n^{m'}$ are driven by stochastic weather conditions during the melt season, so it is likely that area anomalies from before about April do not provide predictability for the summer minimum area.

Modeling studies find increasing variability in the summer minimum ice area in a warming climate [104, 105]. From Eq. (2.16), if the average ice survival ratios $\overline{\alpha}$, $\overline{\beta^g}$ and $\overline{\beta^m}$ continue to decline, α'_n will become increasingly dominant in its control of s'_n. From the CICE hindcast, the variance in α' and $\beta^{m'}$ are comparable. It is therefore likely that increasing variability in the survivability of FY ice, as opposed to simply the transition to an Arctic which is dominated by FY ice, is the source of increasing variability in the summer minimum ice area as simulated by GCMs under greenhouse warming.

2.5.4 Interannual variability in ice volume

The perturbations in the summer minimum ice volume about its equilibrium value are given by

$$\begin{aligned} v'_n &= v_n - \overline{v} \\ &= \overline{\beta^g} \left(\frac{\overline{t^m}}{\overline{t}} \overline{\beta^m} - \frac{\overline{t^f}}{\overline{t}} \overline{\alpha} \right) v'_{n-1} + \cdots, \end{aligned} \tag{2.18}$$

where the terms not shown are with respect to the perturbations α'_n, $\beta_n^{g'}$, $\beta_n^{m'}$, W'_n, $t_n^{f'}$, and $t_n^{m'}$. If these perturbations are well approximated by white noise processes, the memory timescale for volume is then

$$\tau_v = -\frac{1 \text{ year}}{\ln \overline{\beta^g} \left(\frac{\overline{t^m}}{\overline{t}} \overline{\beta^m} - \frac{\overline{t^f}}{\overline{t}} \overline{\alpha} \right)}, \tag{2.19}$$

which is longer than that for area (τ_s) provided that $\overline{t^m} > \overline{t^f}$. This longer timescale arises from the fact that the perturbations in the summer minimum ice volume are dominantly controlled by the perturbations in the thicker MY ice, which carries with it the memory of the sea ice anomalies in the previous year. The persistence timescale for volume is likely longer than τ_v because in Eq. (2.19) we have ignored the additional memory of the previous year's volume that arises through the persistence of MY ice thickness anomalies $t_n^{m'}$ (see Bitz *et al.* [106] and L'Heveder and Houssais [107] for autoregressive models of sea ice thickness).

This timescale, estimated from the average values of the variables from the CICE hindcast (Table 2.1) is ≈ 2.7 years, which is longer than the corresponding estimate for τ_s. The longer memory timescale for volume than area is also apparent in the CCSM3 simulation (over years -150 to 0 in Fig. 2.7, $\tau_s \approx 1.4$ years and $\tau_v \approx 7.0$ years). Corresponding to this longer memory timescale is the tendency for ice volume to remain out of equilibrium for much longer periods of time than does area. In contrast to ice area, it is difficult to accurately estimate the equilibrium ice volume with an average over even a large number of years in a volume time series, and care must be taken when determining whether a given change in volume over a short period of time necessarily implies a change in the equilibrium state of the system.

2.6 Discussion

2.6.1 The dependence of Arctic sea ice on FY and MY ice survivability

Through the use of a reduced model for Arctic sea ice and a simulation of sea ice conditions over the period 1979-2006, we have explored the ways in which the survival ratios of FY and MY ice control the summer minimum ice area and volume. The results of the CICE hindcast suggest that perturbations in summer minimum FY and MY ice areas are comparable in magnitude, and so contribute about equally to interannual variations in the total minimum area (Fig. 2.3b). A perturbation analysis showed that variability in summer ice area is dominated by perturbations in the survival ratios α and β^m, which are governed mostly by stochastic weather noise through the melt season. Therefore, prediction of the summer minimum ice area in a given year depends more on the accurate prediction of weather conditions through the melt season than on the accurate representation of the FY and MY ice area anomalies that exist before the melt season.

Under decreasing ice survival ratios, larger loss of summer MY ice area than FY ice area will occur (Fig. 2.3b and appendix). As a result, trends in the total summer ice area are due more to changes in the amount of MY ice surviving the year than to changes in the amount of FY ice surviving the summer. This is consistent with the trend under decreasing MY ice survival ratios toward an Arctic that is increasingly dominated by FY ice (Eq. (2.13)). The

CICE hindcast also indicates that Arctic sea ice is in a regime where the summer ice cover is particularly sensitive to changes in the FY ice survival ratio $\overline{\alpha}$ (Fig. 2.6 and appendix). The fate of the summer sea ice cover in a warming climate is thus governed primarily by the melt season survivability of the winter FY ice cover. It is therefore critical that trends in FY ice and its survivability are monitored and modeled accurately.

2.6.2 Memory, variability, and mean state sensitivity

We have found that September ice area and volume behave approximately as AR(1) processes. There are several properties of AR(1) systems that are relevant to understanding the current state of the Arctic sea ice system and what changes can be expected in a warming climate. Firstly, systems with long memory timescales recover more slowly from perturbations than do systems with short memory timescales (Eq. (2.9)) and exhibit greater variability in response to a forcing of particular variance (Eq. (2.8)). Secondly, systems with longer response times have enhanced sensitivity to long-term forcing compared to systems with shorter response times (see the appendix, Hansen *et al.* [98] and Bitz and Roe [44]).

The relatively short timescale τ_s for Arctic sea ice area, arising from the strong survival of ice that grows each winter, corresponds to a mean state that has relatively little variability about its long-term trend and low sensitivity to trends in the ice survival ratios. The persistence timescale for sea ice volume τ_v is longer than that for ice area, contributing to a relatively greater variance in ice volume than area (Fig. 2.7). This longer memory timescale for volume corresponds to a greater volume sensitivity than area sensitivity to trends in the survival ratios (see appendix). Relatively larger reductions in ice volume than area have been shown to occur in the CICE hindcast (Table 2.1), in GCMs (Fig. 2.7; [108]), and in observations [17].

Because September ice area—averaged over only a few years—is at all times very nearly in equilibrium with the ice survival ratios, the observed decrease in Arctic sea ice area is a clear indicator of a changing climate. Conversely, the relatively long timescale τ_v implies that September sea ice volume can be out of equilibrium with climate forcing for long periods of time. Thus, while sea ice volume has been shown to be relatively more sensitive

to changes in climate forcing than is ice area, its use as an indicator of changing climate conditions is complicated by its long memory timescale—any statistical test for significance of a trend in ice volume is limited by a reduced number of degrees of freedom [109].

2.6.3 Changing memory and the trajectory of sea ice decline

In a warming climate we can expect the thicker MY ice to thin at a greater rate than the thinner FY ice due to the strong thickness-growth feedback of sea ice [44]. Moreover, we can expect the ratio of MY to FY ice entering into the MY ice category each year to continue to decrease (Eq. (2.13) and Fig. 2.3b). The difference between FY and MY ice types (and their respective survival ratios) will thus likely decrease in a warming climate, shaping the trajectory of sea ice decline. If this occurs, the Arctic sea ice system would move toward a regime of decreased memory and decreased sensitivity to climate forcing (consider Fig. 2.6, or the equations in the appendix, as $\overline{\beta^g} \to \overline{\alpha}$ and $\overline{\beta^m} \to \overline{\alpha}$). Indeed, a decrease in the quantity $\overline{\beta^g}\left(\overline{\beta^m} - \overline{\alpha}\right)$ is seen to occur over the CICE hindcast (Table 2.1), implying a reduction in memory and mean state sensitivity over the course of the simulation. The loss of MY ice in the observed Arctic sea ice system [17, 19, 20, 22, 24] suggests that it may be undergoing a similar decrease in memory.

If the memory timescale and mean state sensitivity of Arctic sea ice decrease sufficiently quickly under a warming climate, a slowing in the rate of area and volume loss could occur. This is consistent with the characteristic trajectory of September sea ice area decline in twenty-first century simulations where the rate of change of Arctic sea ice area decreases late in the simulation despite a continued increase in climate forcing (Fig. 2.7). An inflection point in ice decline could alternatively occur if during the warming the ice survival ratios decrease quickly for some time and then slow in their rate of decrease at some later time (e.g., due to pockets of very thick MY ice lingering long into the future). It is the interaction between the trends in the survival ratios (the forcing) and the memory timescale (the sensitivity to forcing) that determines the full trajectory of ice decline, and further study with a FY ice tracer within fully coupled climate models is needed to determine the exact reason for the inflection point seen in climate simulations. To establish whether we should

expect such a trajectory in the observed sea ice system, we should attempt to estimate the mean state and trends in Arctic sea ice survival ratios from observations and compare these with the results of coupled simulations that exhibit such behavior.

The interpretation of sea ice area and volume as AR(1) processes is useful for gaining insight into the current state and recent trends in the Arctic sea ice system. Its use for long-term projections is dependent upon the assumption that the perturbations in FY and MY survivability that force the system continue to be well approximated by white noise.

2.6.4 New metrics for improving sea ice projections

Stroeve *et al.* [5] compare observed Arctic sea ice trends to the results of the models participating in the Intergovernmental Panel on Climate Change Fourth Assessment Report (IPCC AR4) under the SRES A1B emissions scenario. Of the models with a mean Arctic ice extent within 20% of the observed ice extent over the period 1953-1995, the multi-model mean trend in September ice extent over the period 1979-2006 was $-4.3 \pm 0.3\%$/decade—considerably less than the trend in observations of $-9.1 \pm 1.5\%$/decade over that period. This suggests that while an accurate reproduction of the seasonal cycle of ice extent is necessary, it is not sufficient to reproduce the correct sensitivity to changing climate conditions.

The findings of Stroeve *et al.* [5] are consistent with our result that it is possible to accurately model the climatological seasonal cycle of sea ice area and volume without correctly representing the mean state in FY-MY ice area and thickness space (given by $\overline{\alpha}$, $\overline{\beta^g}$, $\overline{\beta^m}$, $\overline{t^f}$ and $\overline{t^m}$) and its corresponding sensitivity to climate forcing (Figs. 2.1 and 2.6). For example, a sea ice model that tends to homogenize FY and MY ice physics by not resolving t^f and t^m effectively lowers the MY ice survival ratio while raising the FY ice survival ratio. Such a model, though it may reproduce the seasonal cycle of ice area, will nonetheless have decreased memory timescales (particularly for volume) and be generally less sensitive to climate forcing. Indeed, two models that are among the most sophisticated (NCAR CCSM3 and UKMO HadGEM) most closely reproduce the observed trend in September Arctic sea ice extent [5].

If we are to make accurate projections of September sea ice area and volume trends it

is important that sea ice models are validated using more than just the observed area and volume. Given the connection between memory timescale and mean state sensitivity, one metric for models might be to correctly reproduce the variance and lag 1 year autocorrelations from observations of summer minimum ice area and volume. However, given the relatively short time series of observed ice area and volume, there are large uncertainties associated with using these values to estimate the underlying mean state of the sea ice system. A more useful metric for establishing skill in sea ice projections would be the direct comparison of FY and MY ice survival ratios between models and observations. While observations of Arctic sea ice are now available for such a comparison [17, 19, 20, 22, 24], the models participating in the IPCC AR4 have not traced FY and MY ice individually. Thus, we have a valuable opportunity to validate models with observations that have not previously been considered in the modeling process.

2.6.5 Concluding remarks

Motivated by recent studies assessing the characteristics of FY and MY sea ice in the Arctic, we have introduced a reduced model for ice area and volume based upon the survivability of FY and MY ice. This model results in a simple picture of summer minimum Arctic sea ice in which its mean state, memory timescale, and sensitivity to climate forcing can be described naturally in terms of the climatological properties FY and MY ice. Through the addition of a FY ice tracer to the sea ice model CICE, we found that small trends in the ice survival ratios explain the decline in total ice area—and the relatively larger loss of MY ice area—over the 1979-2006 hindcast. The simple relations developed here provide a framework with which to interpret changes in observed Arctic FY and MY ice areas as well.

While models agree that increased greenhouse gas concentrations will result in a reduction of Arctic sea ice area and volume, there is much uncertainty in projections of the rate at which this will occur [5]. Observations of FY and MY ice survivability can place constraints on sea ice climate sensitivity, and provide a benchmark for models to establish confidence in sea ice projections. Enabling GCMs to trace FY and MY ice independently may then provide insight into the reasons for the discrepancies between modeled and observed Arctic

sea ice trends, and into what trajectory of ice decline we should expect in a warming climate.

2.7 Appendix: equilibrium sensitivity analysis

Here we perform an analysis of the sensitivity of the summer minimum ice area and volume with respect to trends in the survival ratios and winter maximum area. The equilibrium summer minimum total, FY, and MY ice areas, and total ice volume are given by Eqs. (2.10)–(2.12) and Eq. (2.15). Here we show how each of these changes with respect to changing survival ratios ($\overline{\alpha}$, $\overline{\beta^g}$, $\overline{\beta^m}$) and winter maximum area ($\overline{W}$).

From Eq. (2.10), the change in summer minimum FY ice area is:

$$\begin{aligned}
\frac{\partial \overline{f}}{\partial \overline{W}} &= \left(1 - \overline{\beta^g}\,\overline{\beta^m}\right) \frac{\overline{s}}{\overline{W}} \\
\frac{\partial \overline{f}}{\partial \overline{\alpha}} &= \left(\overline{W} - \overline{\beta^g}\overline{s}\right) \frac{1 - \overline{\beta^g}\,\overline{\beta^m}}{1 - \overline{\beta^g}\left(\overline{\beta^m} - \overline{\alpha}\right)} \\
\frac{\partial \overline{f}}{\partial \overline{\beta^g}} &= -\overline{s} \frac{\overline{\alpha}}{1 - \overline{\beta^g}\left(\overline{\beta^m} - \overline{\alpha}\right)} \\
\frac{\partial \overline{f}}{\partial \overline{\beta^m}} &= -\overline{s} \frac{\overline{\alpha}\overline{\beta^g}^2}{1 - \overline{\beta^g}\left(\overline{\beta^m} - \overline{\alpha}\right)}.
\end{aligned} \tag{2.20}$$

These relations show a decrease in $\overline{f}$ under decreasing $\overline{\alpha}$, and an increase in $\overline{f}$ under decreasing $\overline{\beta^g}$ and $\overline{\beta^m}$. The increase in $\overline{f}$ under decreasing MY ice survival ratios arises as FY ice fills in some of the available area as winter MY ice area decreases.

From Eq. (2.11), the change in summer minimum MY ice area is:

$$\begin{aligned}
\frac{\partial \overline{m}}{\partial \overline{W}} &= \overline{\beta^g}\,\overline{\beta^m} \frac{\overline{s}}{\overline{W}} \\
\frac{\partial \overline{m}}{\partial \overline{\alpha}} &= \left(\overline{W} - \overline{\beta^g}\overline{s}\right) \frac{\overline{\beta^g}\,\overline{\beta^m}}{1 - \overline{\beta^g}\left(\overline{\beta^m} - \overline{\alpha}\right)} \\
\frac{\partial \overline{m}}{\partial \overline{\beta^g}} &= \overline{s} \frac{\overline{\beta^m}}{1 - \overline{\beta^g}\left(\overline{\beta^m} - \overline{\alpha}\right)} \\
\frac{\partial \overline{m}}{\partial \overline{\beta^m}} &= \overline{s} \frac{\left(1 + \overline{\alpha}\overline{\beta^g}\right)\overline{\beta^g}}{1 - \overline{\beta^g}\left(\overline{\beta^m} - \overline{\alpha}\right)}.
\end{aligned} \tag{2.21}$$

These show a decrease in $\overline{m}$ under decreases in both FY and MY ice survival ratios: a decrease in $\overline{\beta^g}$ or $\overline{\beta^m}$ decreases the amount of MY ice surviving the growth or melt seasons, and a decrease in $\overline{\alpha}$ decreases the amount of FY ice that is promoted to the MY ice category each year.

Comparing Eq. (2.20) with Eq. (2.21) shows that under decreases in $\overline{W}$ or $\overline{\alpha}$, the equilibrium areas $\overline{f}$ and $\overline{m}$ decrease in proportion to their respectively values so as to preserve the ratio $\overline{m}/\overline{f}$ (consistent with Eq. (2.13), which shows that the ratio $\overline{m}/\overline{f}$ is independent of $\overline{W}$ or $\overline{\alpha}$). If there is more MY ice than FY ice at the summer minimum (corresponding to $\overline{\beta} = \overline{\beta^g}\,\overline{\beta^m} > 0.5$), then there will be a greater loss of MY ice than FY ice due to decreasing $\overline{W}$ or $\overline{\alpha}$. The results of the CICE hindcast show, on average, more MY ice than FY ice in summer (from Table 2.1, $\overline{\beta} \approx 0.602$). Thus the Arctic is likely in a regime where trends in both FY and MY survival ratios result in a greater change in $\overline{m}$ than $\overline{f}$, as seen in Fig. 2.3b.

From Eq. (2.12), or from the addition of Eq. (2.20) and Eq. (2.21), the change in total summer minimum ice area is:

$$\begin{aligned}
\frac{\partial \overline{s}}{\partial \overline{W}} &= \frac{\overline{s}}{\overline{W}} \\
\frac{\partial \overline{s}}{\partial \overline{\alpha}} &= \left(\overline{W} - \overline{\beta^g}\overline{s}\right) \frac{1}{1 - \overline{\beta^g}\left(\overline{\beta^m} - \overline{\alpha}\right)} \\
\frac{\partial \overline{s}}{\partial \overline{\beta^g}} &= \overline{s} \frac{\overline{\beta^m} - \overline{\alpha}}{1 - \overline{\beta^g}\left(\overline{\beta^m} - \overline{\alpha}\right)} \\
\frac{\partial \overline{s}}{\partial \overline{\beta^m}} &= \overline{s} \frac{\overline{\beta^g}}{1 - \overline{\beta^g}\left(\overline{\beta^m} - \overline{\alpha}\right)}.
\end{aligned} \tag{2.22}$$

From these relations, a change of $\overline{W}$ acts to maintain the ratio $\overline{s}/\overline{W}$ as this ratio depends only on the FY and MY ice survival ratios (Eq. (2.12)). Also, $\overline{s}$ is more sensitive to changes in $\overline{\beta^m}$ than in $\overline{\beta^g}$ because the value $\overline{\beta^m} - \overline{\alpha}$ is smaller than $\overline{\beta^g}$ (from Table 2.1, $\overline{\beta^m} - \overline{\alpha} \approx 0.585$ and $\overline{\beta^g} \approx 0.764$). This arises from the ability of FY ice to grow in place of MY ice that is lost during the growth season. As $\overline{s}$ decreases it becomes increasingly sensitive to changes in $\overline{\alpha}$ since there will be more FY ice at the beginning of each melt season. Because $\overline{\beta^m} > \overline{\alpha}$, the loss of MY ice area is greater than the gain of FY ice area under decreasing MY ice survival ratios, resulting in a decrease in total ice area.

From Eqs. (2.15) and (2.22) the change in total ice volume $\overline{v}$ can be related to the change

in total ice area $\overline{s}$:

$$\begin{aligned}
\frac{1}{\overline{v}}\frac{\partial \overline{v}}{\partial \overline{W}} &= \frac{1}{\overline{s}}\frac{\partial \overline{s}}{\partial \overline{W}} \\
\frac{1}{\overline{v}}\frac{\partial \overline{v}}{\partial \overline{\alpha}} &= \frac{1}{\overline{s}}\frac{\partial \overline{s}}{\partial \overline{\alpha}} \\
\frac{1}{\overline{v}}\frac{\partial \overline{v}}{\partial \overline{\beta^g}} &= \frac{1}{\overline{s}}\frac{\partial \overline{s}}{\partial \overline{\beta^g}} + \frac{\overline{t^m} - \overline{t^f}}{\overline{t}}\overline{\beta^m} \\
\frac{1}{\overline{v}}\frac{\partial \overline{v}}{\partial \overline{\beta^m}} &= \frac{1}{\overline{s}}\frac{\partial \overline{s}}{\partial \overline{\beta^m}} + \frac{\overline{t^m} - \overline{t^f}}{\overline{t}}\overline{\beta^g}.
\end{aligned} \tag{2.23}$$

The fractional change in volume $\overline{v}$ is equal to the fractional change in $\overline{s}$ under changes in $\overline{W}$ and $\overline{\alpha}$, leaving the average thickness unchanged. This results from the fact that changes in $\overline{W}$ and $\overline{\alpha}$ act to preserve the ratio of areas of thick MY ice to thin FY ice (given by Eq. (2.13)). However, changes in either of the MY ice survival ratios act to change $\overline{v}$ and $\overline{s}$ by fractionally different amounts, where this difference is due to the the fact that the thick MY ice (with thickness $\overline{t^m}$) changes in area by a larger amount than does the thin FY ice (with thickness $\overline{t^f}$). Therefore, there is always a greater fractional loss of ice volume than ice area (and a corresponding thinning of the total average ice thickness) under decreasing MY ice survival ratios, provided that a difference in thickness exists between the FY and MY ice types (i.e., $\overline{t^m} > \overline{t^f}$).

Chapter 3

THE REVERSIBILITY OF SEA ICE LOSS IN A STATE-OF-THE-ART CLIMATE MODEL

Kyle C. Armour, Ian Eisenman, Eduardo Blanchard-Wrigglesworth, Kelly E. McCusker and Cecilia M. Bitz (2011) The reversibility of sea ice loss in a state-of-the-art climate model. *Geophysical Research Letters*, 38, L16705, doi: 10.1029/2011GL048739.

3.1 Summary

Rapid Arctic sea ice retreat has fueled speculation about the possibility of threshold (or 'tipping point') behavior and irreversible loss of the sea ice cover. We test sea ice reversibility within a state-of-the-art atmosphere–ocean global climate model by increasing atmospheric carbon dioxide until the Arctic Ocean becomes ice-free throughout the year and subsequently decreasing it until the initial ice cover returns. Evidence for irreversibility in the form of hysteresis outside the envelope of natural variability is explored for the loss of summer and winter ice in both hemispheres. We find no evidence of irreversibility or multiple ice-cover states over the full range of simulated sea ice conditions between the modern climate and that with an annually ice-free Arctic Ocean. Summer sea ice area recovers as hemispheric temperature cools along a trajectory that is indistinguishable from the trajectory of summer sea ice loss, while the recovery of winter ice area appears to be slowed due to the long response times of the ocean near the modern winter ice edge. The results are discussed in the context of previous studies that assess the plausibility of sea ice tipping points by other methods. The findings serve as evidence against the existence of threshold behavior in the summer or winter ice cover in either hemisphere.

3.2 Introduction

Arctic sea ice has undergone rapid changes in recent decades (*Chap. 1*). Observations showing substantial reduction in areal sea ice coverage [5,96] and overall thinning in conjunction

with a loss of older, thicker sea ice [17, 24] have fueled speculation that Arctic sea ice may be at or near a critical threshold (or 'tipping point'), beyond which abrupt and irreversible loss of ice will occur [2, 24, 28–39].

Does the sea ice system show hallmarks of threshold behavior, such as multiple ice-cover states and hysteresis? Direct assessment of sea ice reversibility with theory [43] and indirect assessments with coupled atmosphere–ocean global climate models (GCMs) [46–50] indicate that a tipping point in summer Arctic sea ice cover is unlikely. However, direct assessments within GCMs have yet to be performed. Such a measure could be achieved by looking for hysteresis in sea ice cover when radiative forcing is raised until the oceans become ice-free and subsequently lowered, ideally within a suite of different state-of-the-art coupled GCMs.

This work represents a step toward this goal: we report the results of a simulation with a state-of-the-art coupled GCM in which atmospheric CO_2 is increased at 1% yr^{-1} (compounded) until the Arctic Ocean becomes ice-free throughout the year and subsequently decreased until the initial ice cover returns (Fig. 3.1a). Evidence for sea ice irreversibility in the form of hysteresis outside the envelope of year-to-year variability is examined for the loss of summer and winter ice cover in both hemispheres.

3.3 Model setup and analysis methods

We use version 3 of the Community Climate System Model (CCSM3) at the standard resolution, which is T42 spectral truncation in the atmosphere and a nominally 1° ocean grid [9]. Sea ice conditions in CCSM3 are well described previously [110,111]. The Arctic sea ice cover in this model is the most sensitive to climate changes of the current suite of state-of-the-art GCMs [5, 14, 112], and it has been found to exhibit rapid changes, comparable to recent observations [110], which have been interpreted as evidence for irreversible tipping points [30, 34]. Our simulation branches from a modern-day (1990s) control run with initial CO_2 concentration of 355 ppmv. Carbon dioxide is ramped at +1% yr^{-1} (red line in Fig. 3.1) until the northern hemisphere (NH) becomes perennially ice-free (monthly sea ice area consistently less than 10^6 km^2). This occurs in year 219 of ramping, at which point CO_2 is approximately nine times its initial level and the global-mean surface temperature has increased by about 6.5 °C (red points in Fig. 3.2). While the southern hemisphere (SH)

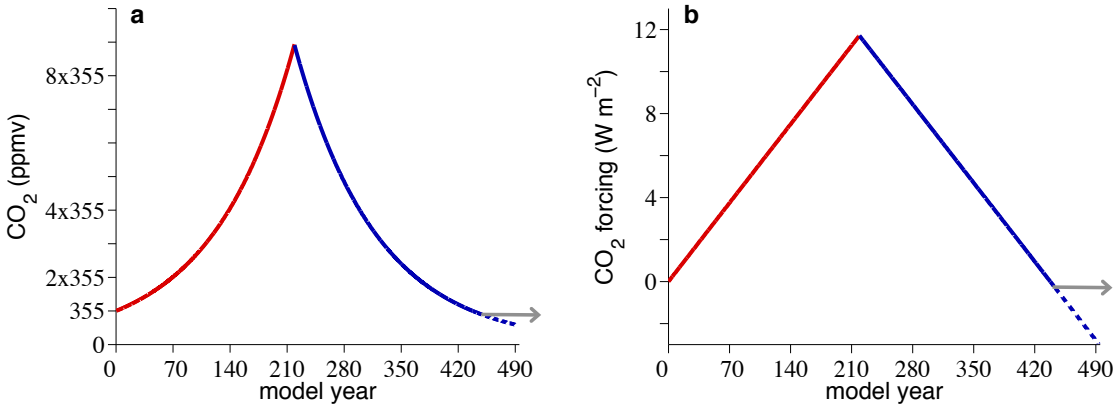

Figure 3.1: Prescribed atmospheric CO_2 concentration and global radiative forcing. **a,** CO_2 is increased at $+1\%$ yr^{-1} (red) until about nine times its initial level, then decreased at -1% yr^{-1} (blue) to a value below its initial concentration (dashed blue). Grey indicates an additional experiment where CO_2 is held fixed upon returning to its initial concentration for a period of 450 years. **b,** As for **a**, but the corresponding CO_2 radiative forcing, which varies approximately linearly with time over the rampings [73].

becomes ice-free in austral summer, its winter ice cover persists throughout the ramping. Upon reaching an ice-free Arctic, CO_2 is decreased at -1% yr^{-1} until both hemispheres are returned to near their initial (1990s) temperatures (blue points in Fig. 3.2), which occurs in year 493 of the simulation when CO_2 is around 205 ppmv.

Global radiative forcing (R) changes approximately linearly with time over the CO_2 rampings, by about 3.7 Wm^{-2} per 70 yr (Fig. 3.1b), which is the period of CO_2 doubling or halving [73]. The offset in Fig. 3.2 between warming (red) and cooling (blue) trajectories implies a lagged response of hemispheric-mean annual-mean surface temperature anomalies (ΔT_{NH} and ΔT_{SH}), as expected from deep ocean heat storage [57]. To approximately account for this lag between hemispheric climate and radiative forcing, we utilize two approaches. First, we consider the evolution of ice area as a function of hemispheric temperature rather than time. A justification for this treatment is that annual-mean Arctic sea ice area has been found to decline linearly with increasing global-mean temperature across a range of GCMs, emissions scenarios, and climates [14, 46–48, 108]. Specifically, we extend the arguments of Winton [14], relating hemispheric ice cover to global forcing through

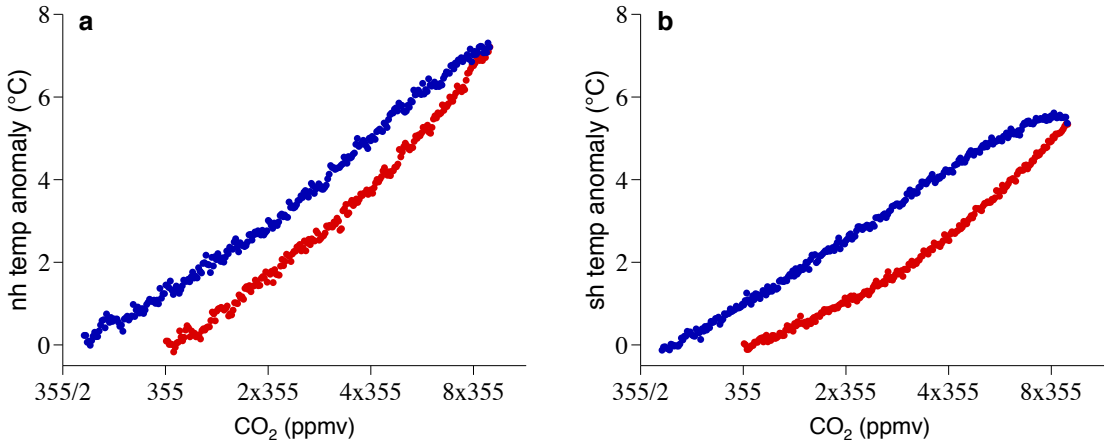

Figure 3.2: Hemispheric surface temperature as a function of CO_2 concentration. (a) NH-mean and (b) SH-mean annual-mean surface temperature anomalies over the CCSM3 simulation. Increasing CO_2 concentration (in red) results in a warming trajectory and decreasing CO_2 concentration (in blue) results in a cooling trajectory. Temperature anomalies are with respect to the 1990 control level, and CO_2 is plotted on a log scale.

$$\Delta A_{\mathrm{NH}} = \frac{\Delta A_{\mathrm{NH}}}{\Delta T_{\mathrm{NH}}} \frac{\Delta T_{\mathrm{NH}}}{\Delta R} \Delta R, \tag{3.1}$$

and

$$\Delta A_{\mathrm{SH}} = \frac{\Delta A_{\mathrm{SH}}}{\Delta T_{\mathrm{SH}}} \frac{\Delta T_{\mathrm{SH}}}{\Delta R} \Delta R, \tag{3.2}$$

where A_{NH} and A_{SH} are monthly- or annual-mean hemispheric ice areas. We define the quantities $\Delta A_{\mathrm{NH}}/\Delta T_{\mathrm{NH}}$ and $\Delta A_{\mathrm{SH}}/\Delta T_{\mathrm{SH}}$ as the sea ice sensitivity in each hemisphere, which is similar to the treatment in Winton [14] except that we consider both hemispheres and use hemispheric-mean rather than global-mean temperature.

Separating the dependence of temperature on forcing ($\Delta T_{\mathrm{NH}}/\Delta R$ and $\Delta T_{\mathrm{SH}}/\Delta R$) from the dependence of ice area on temperature ($\Delta A_{\mathrm{NH}}/\Delta T_{\mathrm{NH}}$ and $\Delta A_{\mathrm{SH}}/\Delta T_{\mathrm{SH}}$) permits a consistent comparison of sea ice sensitivity across climate models and forcing scenarios [14], accounts for contrasting hemispheric climate trends (Fig. 3.2), and effectively isolates the sea ice response to hemispheric climate change for the purposes of evaluating sea ice reversibility. We thus first examine the evidence for hysteresis in hemispheric ice area with respect to hemispheric-mean annual-mean temperature (ΔA_{NH} vs ΔT_{NH} and ΔA_{SH} vs ΔT_{SH}).

Our second approach to account for the lag between hemispheric climate and the imposed radiative forcing relates ΔA_{NH} and ΔA_{SH} directly to CO_2 with a specified memory timescale.

3.4 Results

3.4.1 Reversibility of sea ice loss with respect to hemispheric temperature

We first describe the progression to an ice-free Arctic under NH warming (red points in Fig. 3.3a-c). The strong linearity of annual-mean ice area decline continues throughout the simulation, spanning a range in T_{NH} of over 6 °C (Fig. 3.3a). However, the trajectories of monthly ice cover (Fig. 3.3b-c) show more complex behavior. A large change in March ice cover sensitivity occurs when ice area is approximately equal to that of the Arctic basin ($\sim 9{\times}10^6$ km^2), suggestive of geographic controls on the rate of area loss with warming [116]. Indeed, the March *equivalent ice area* [116], which accounts for geographic effects, is found to vary linearly with T_{NH} over the entire range (Fig. 3.4). Note that the observed relationship between A_{NH} and T_{NH} for the period 1979-2011 (black points in Fig. 3.3a-c) demonstrates model biases in both the mean state [111] and sensitivity [14] of the sea ice cover simulated with CCSM3.

The relationship between warming (red) and cooling (blue) trajectories in Fig. 3.3 illustrates the reversibility of sea ice area loss. Subject to NH cooling, September ice area recovers along a trajectory that is visually indistinguishable from the warming trajectory (Fig. 3.3b). Thus these results suggest that the loss of September Arctic ice cover within CCSM3 is fully reversible over the range of sea ice states between modern and annually ice-free climates.

March ice area, by contrast, recovers along a trajectory that is increasingly distinct from the warming trajectory when the sea ice edge extends beyond the Arctic basin ($A_{\mathrm{NH}} \gtrsim 9 \times 10^6$ km^2 in Fig. 3.3c). This may initially seem to suggest the possibility of hysteresis and hence multiple stable ice-cover states under the same hemispheric-mean temperature. However, comparison between the spatial patterns of March ice cover and annual-mean surface temperature under warming and cooling reveals distinct locations, including the Sea of Okhotsk, where March ice area recovery is substantially delayed (Fig. 3.5a). These

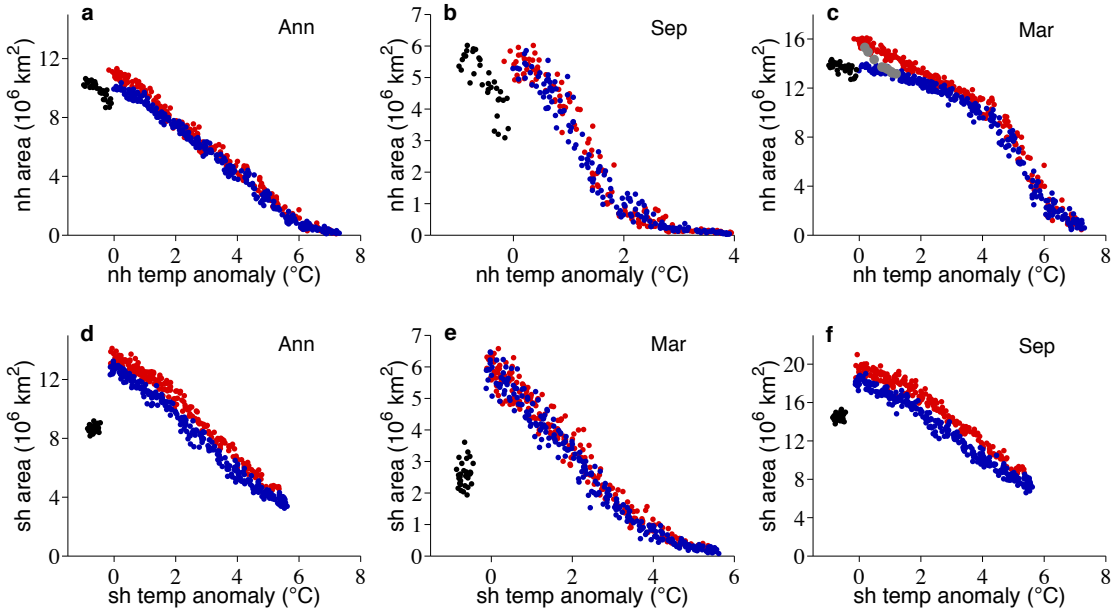

Figure 3.3: Sea ice area as a function of hemispheric surface temperature anomaly. Arctic sea ice **a,** Annual, **b,** September and **c,** March sea ice areas. Antarctic **d,** Annual, **e,** March and **f,** September sea ice areas. The period with increasing CO_2 concentration is shown in red and the period with decreasing concentration is shown in blue. Black points show the observed relationship between ice area [113] and temperature anomalies [114] for the period 1979-2011. Observed temperatures have been normalized to CCSM3 for the period 1950-1980 of a 20th Century CCSM3 simulation. Gray points in **c** show 50-year averages of an additional 450-year long simulation in which CO_2 is held fixed upon returning to the initial concentration of 355 ppmv, instead of continuing to decrease at -1% yr^{-1} to 205 ppmv as in the blue trajectory.

locations largely correspond to regions of the ocean that have been previously noted to exhibit extremely long timescales of response to climate forcing, particularly when cooling [115]. Thus, it is likely that the difference between warming and cooling trajectories is due to spatially varying timescales of adjustment, and is an artifact of the relatively fast rate of CO_2 variation in our simulation.

To verify this interpretation, we examine an additional 450-year long simulation in which CO_2 is held fixed after reaching the initial value of 355 ppmv during the ramp down (gray lines in Fig. 3.1 and gray points in Fig. 3.3c). If multiple ice-cover states were supported by the same T_{NH}, then the ice area would be expected to remain constant or continue to evolve

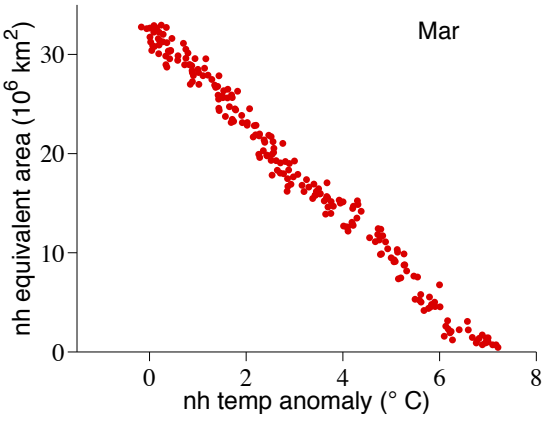

Figure 3.4: March Arctic equivalent sea ice area as a function of surface temperature. Equivalent ice area accounts for the effect of geography on the ice area, and hence its linearity with NH temperature suggests that the change in NH March sea ice sensitivity in Fig. 3.3 is due to the influence of the coastlines. We compute the equivalent ice area by finding the total land plus ocean area poleward of the latitude with poleward ocean area equal to the actual ice area [116].

along the cooling trajectory in $A_{\rm NH}$ vs $T_{\rm NH}$ space. Instead, the ice cover evolves toward its initial (1990s) state as the anomalously warm regions of the ocean slowly attain equilibrium (cf. Fig. 3.5). We thus conclude that March ice area shows no signs of hysteresis, and that the loss of the modern Arctic wintertime sea ice cover appears to be reversible within CCSM3.

We note that even when the March ice edge is within the Arctic basin ($A_{\rm NH} \lesssim 9 \times 10^6$ km^2), there is a small offset between the warming and cooling trajectories which can be seen under close inspection of Fig. 3.3c. However, the offset appears to be relatively constant and hence consistent with a small difference in lag between $T_{\rm NH}$ and $A_{\rm NH}$, rather than a hysteresis window, and it does not occur when a memory timescale is explicitly imposed (*Section 3.4.2*).

The Antarctic sea ice sensitivity in CCSM3 is very similar to the Arctic sea ice sensitivity, as illustrated by the similar slopes in Figs. 3.3a and 3.3d [112]. The SH reaches ice-free conditions in late austral summer (March) during the warming trajectory (Fig. 3.3e), but in contrast to the NH, late austral winter (September) ice cover never disappears completely

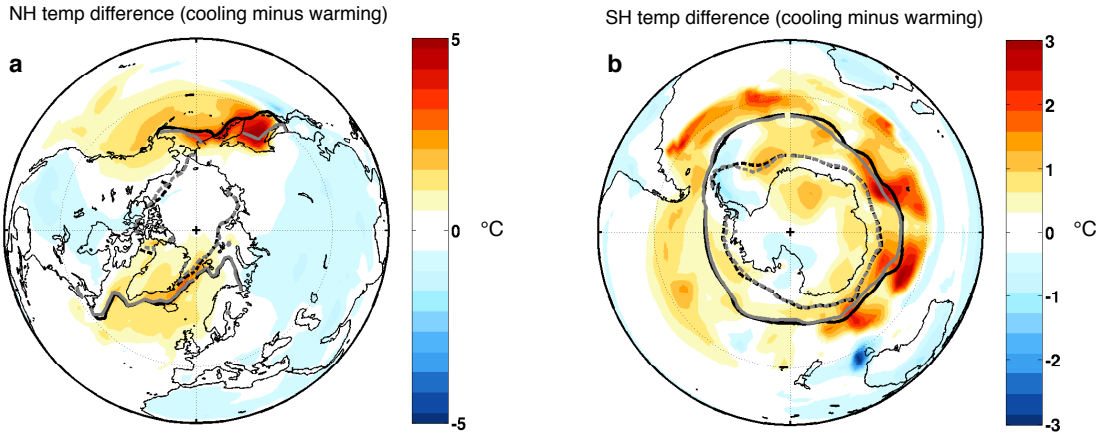

Figure 3.5: Differences in temperature and sea ice between warming and cooling trajectories. **a,** NH and **b,** SH annual-mean surface temperature anomalies (°C) and sea ice extent differences between cooling and warming trajectories, averaged over 30-year periods when hemispheric-mean temperature is comparable (model years 30-60 compared to model years 437-467). Lines show the 15% sea ice concentration contours, with black corresponding to the warming trajectory, gray corresponding to the cooling trajectory, solid lines showing winter sea ice extent, and dashed lines showing summer ice extent.

(Fig. 3.3f). This is associated with a smaller increase in T_{SH} than in T_{NH}. Note that there is a substantial positive bias in current A_{SH} in CCSM3 compared with observations. Acknowledging this, we assess the evidence for Antarctic sea ice irreversibility and compare with the NH results.

Subject to SH cooling, March ice area recovers along a trajectory that is visually indistinguishable from the warming trajectory (Fig. 3.3e), and thus appears to be fully reversible over the range of sea ice states between modern and ice-free climates. The recovery of September ice area, by contrast, occurs along a cooling trajectory that is distinct from the warming trajectory (Fig. 3.3f). However, like NH winter sea ice when it is contained within the Arctic basin, the cooling trajectory appears to simply be lagged behind the warming trajectory, consistent with the relatively slow response of distinct locations in the Southern Ocean (Fig. 3.5b). Thus, the loss of Antarctic winter ice cover appears to be reversible within CCSM3.

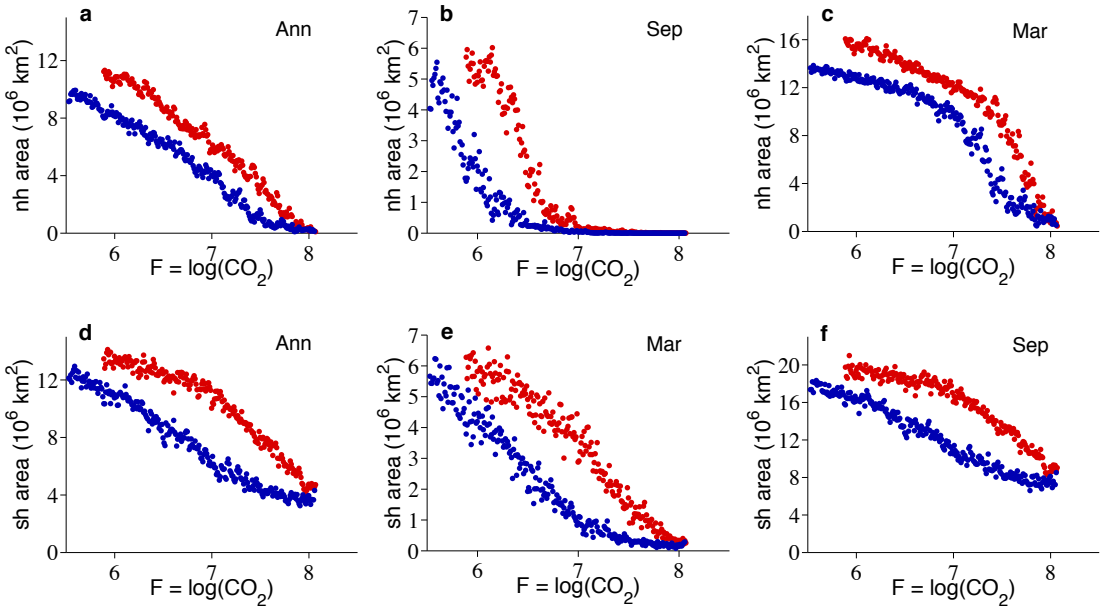

Figure 3.6: Sea ice area as a function of instantaneous CO_2 forcing $F = \log(CO_2)$. Arctic **a,** Annual, **b,** September and **c,** March sea ice areas. Antarctic **d,** Annual, **e,** March and **f,** September sea ice areas. The period with increasing CO_2 concentration is shown in red and the period with decreasing concentration is shown in blue.

3.4.2 Reversibility of sea ice loss with respect to CO_2 forcing

We have assessed the evidence for hysteresis in sea ice area with respect to hemispheric-mean annual-mean surface temperature in order to account for the lag between forcing changes and climate response. A potential limitation of this method is that the memory timescale of hemispheric-mean temperature and of ice area may not depend on the same physical factors. Furthermore, to the extent that hemispheric-mean temperature itself depends slightly on sea ice area, the analysis could plausibly be missing an element of hysteresis in the sea ice cover. We thus assess here the possibility of sea ice irreversibility with respect to CO_2 forcing.

We define as the control parameter we vary

$$F(t) \equiv \log(\mathrm{CO}_2(t)), \tag{3.3}$$

which is linearly related to the radiative forcing R. Since CO_2 increases and decreases at

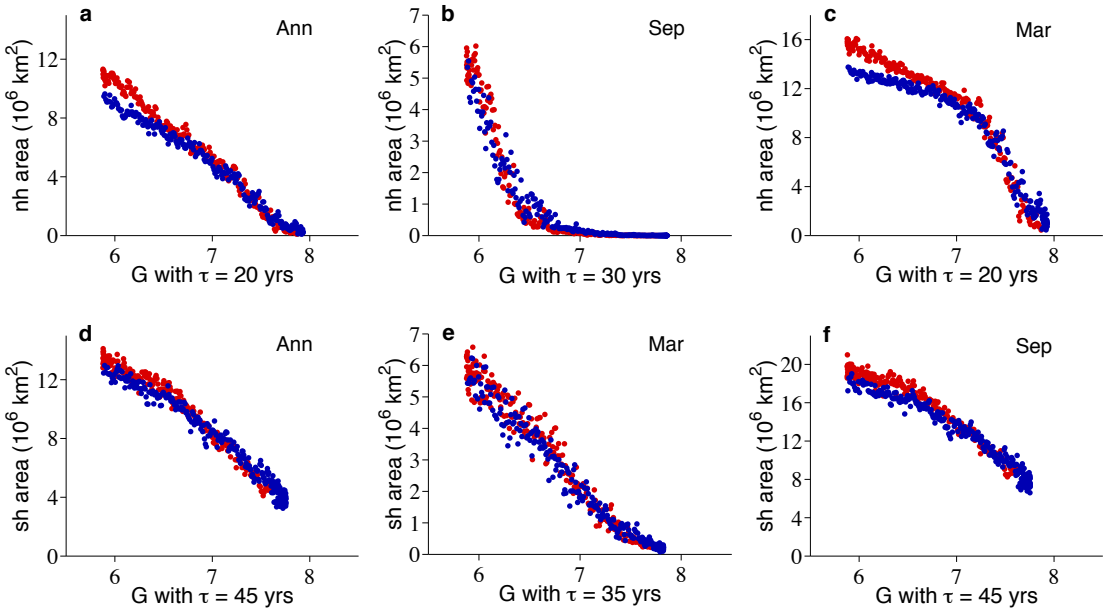

Figure 3.7: Sea ice area as a function of lagged CO_2 forcing G with memory timescale τ. Arctic **a,** Annual, **b,** September and **c,** March sea ice areas. Antarctic **d,** Annual, **e,** March and **f,** September sea ice areas. The lagged forcing G is described by Eq. (3.4). The period with increasing CO_2 concentration is shown in red and the period with decreasing concentration is shown in blue.

1% yr^{-1} over the course of the simulation, F increases and decreases linearly with time (by $+0.01\ \mathrm{yr}^{-1}$ and $-0.01\ \mathrm{yr}^{-1}$, respectively). Fig. 3.6 shows the trajectories of hemispheric sea ice area with respect to $F = \log(\mathrm{CO}_2)$. Because F is ramped relatively quickly, the climate does not maintain a steady state with the forcing and a lag is introduced between changes in F and the sea ice response. To account for this effect, we further define a *lagged forcing*, $G(t)$, as the solution to the differential equation

$$\frac{\mathrm{d}G}{\mathrm{d}t} = \frac{F - G}{\tau}. \tag{3.4}$$

The characteristic memory timescale, τ, is assumed to be constant over the simulation but may take on different values depending on season and hemisphere.

Fig. 3.7 shows hemispheric sea ice area with respect to the lagged forcing G, where values of τ have been chosen to visually maximize agreement between warming and cooling trajectories. Values of τ are longer for the SH than the NH, consistent with the relatively

slower adjustment of the SH climate to changes in forcing (Fig. 3.2). The wintertime ice cover warming and cooling trajectories appear to diverge slightly when the ice cover is near its most extensive, particularly in the NH. As discussed above, this appears to arise because the winter ice edge advances, under reduced CO_2, into regions of the ocean that have anomalously long timescales of adjustment to forcing changes (regionally larger τ), particularly under cooling. Fig. 3.7 demonstrates that accounting for a simple linear memory is sufficient to explain most of the differences between warming and cooling sea ice trajectories under changes in F. These results are thus in general agreement with the analysis in terms of hemispheric-mean temperatures.

3.5 Discussion and conclusions

The central finding of this study is that sea ice loss is fully reversible in a state-of-the-art GCM over a range of CO_2 concentrations from the 1990s level to nine times higher. We find no evidence for threshold behavior in the summer or winter ice cover in either hemisphere. Thus if tipping points exist for future sea ice retreat in nature, it is for subtle reasons, i.e., through processes that are absent or inadequately represented in this model. Our results do not address the possibility of sea ice hysteresis between closely separated states within the envelope of natural variability or in climate regimes with more extensive ice cover [117,118].

These findings can be compared with previous studies. Winton [46] finds that CCSM3 loses all of its Arctic sea ice in a smooth manner, consistent with our results, and that another GCM considered (MPI ECHAM5) also loses its summer ice cover smoothly. Tietsche *et al.* [50] similarly find no evidence of summer Arctic sea ice tipping points in the ECHAM5 model. However, Winton [46] finds that ECHAM5 shows evidence for nonlinearity during the loss of its winter Arctic ice cover. Eisenman and Wettlaufer [43] propose a physical argument that if an irreversible threshold exists for the sea ice cover, it should be expected during the loss of winter ice. It thus seems plausible that some models, such as ECHAM5, may show irreversible threshold behavior during the loss of winter ice cover in a very warm climate, in contrast to the CCSM3 results presented here. This emphasizes the importance of repeating CO_2 ramping experiments such as this one with other state-of-the-art coupled GCMs.

Summer sea ice cover in each hemisphere appears to have a well-defined relationship with hemispheric-mean temperature, under both warming and cooling trajectories, suggesting the possibility of relatively simple thermodynamic controls on summer ice cover. Winter sea ice cover also appears to be related to hemispheric-mean temperature, but its rate of loss and recovery is found to be complicated by the local response of the oceans near the present-day winter ice edge.

A lack of hysteresis in sea ice area may be expected based on the short persistence timescale of ice area anomalies, as found in both models [11, 50, 119] and observations [11, 116]. The short timescale means that sea ice area responds to climate changes on timescales of a few years or less (*Chap. 2*; [108]) and, thus, responds to slow climate variations independently of its history (i.e., without hysteresis). Alternatively, other components of the climate system (e.g., ocean circulation) could plausibly be expected to exhibit hysteretic behavior and, in turn, drive sea ice irreversibility, but such a scenario did not occur within our simulation.

Components of the climate system not represented in CCSM3 (e.g., dynamic land ice) could, in principle, cause sea ice hysteresis. Similarly, the simulation setup in this study does not address the possibility of hysteresis when CO_2 is varied more slowly such that the deep ocean temperature is near steady-state with the forcing. Thus, our findings are expected to be most relevant to the assessment of sea ice thresholds under transient warming over the next few centuries in the absence of substantial land ice sheet changes.

A recent analysis [57] suggests that the climate system can be viewed as comprising a fast upper ocean component with a characteristic timescale of less than 5 years and a slowly evolving deep ocean component. In this view, the surface component is driven by a mixture of radiative forcing and heat exchange with the more slowly evolving deep ocean, which leads to the difference between warming and cooling surface temperature trajectories under the same radiative forcing in Fig. 3.2. Hence the source of the several decade time lags in Fig. 3.7 may be primarily due to forcing of the surface component by heat exchange with the deep ocean. It is thus not surprising that our two methods of assessing reversibility (with respect to hemispheric temperature and lagged climate forcing) give largely similar results.

Due to the rate of radiative forcing changes in the simulation presented here, our results do not address the possibility of hysteresis in deep ocean temperature, but they suggest that there is not hysteresis in the surface climate. An implication of this interpretation is that reduced forcing after modest warming would result in a quick return to initial sea ice conditions, whereas if deep ocean warming is maintained for centennial timescales (as in the scenario presented here), the recovery of the sea ice cover would be substantially delayed even under abrupt reductions in greenhouse gas forcing.

The results presented here illustrate a hazard of using factors such as an increase in variance as generic 'early-warning signals' of an approaching tipping point [32,33,36,37,39, 120]. Although we find that CCSM3 does not show evidence of a summer sea ice tipping point, the variance in summer Arctic sea ice area increases in the model as the climate warms [104, 105]. The increase in variance may plausibly be related to a reduction in stability, or alternatively it may be driven by other factors such as reduced geographic muting of ice edge variability [104,116], an overall thinning of the ice pack [121], or increased variance of first-year sea ice survivability with warming (*Chap. 2*). However, in light of the present findings, it does not appear to be associated with a loss of stability altogether. Given that these same processes are expected to be at work in nature, variance in the observed sea ice cover may similarly be an unreliable indicator of an approaching threshold.

Finally, the coupled GCM that we employ in this study (CCSM3) exhibits periods of rapid sea ice loss under warming [110]—comparable to recent observations—that have often been interpreted as tipping point behavior [30, 34]. However, the reversibility of the sea ice cover within this model suggests that such interpretations are misguided. The lack of evidence for critical sea ice thresholds within a state-of-the-art GCM implies that future sea ice loss will occur only insofar as global warming continues, and may be fully reversible. This is ultimately an encouraging conclusion; although some future warming is inevitable (*Chap. 4*), in the event that greenhouse gas emissions are reduced sufficiently for the climate to cool back to modern hemispheric-mean temperatures, a sea ice cover similar to modern-day is expected to follow.

Chapter 4

THE CLIMATE RESPONSE TO CESSATION OF GREENHOUSE GAS AND AEROSOL EMISSIONS

Kyle C. Armour and Gerard H. Roe (2011) Climate commitment in an uncertain world. *Geophysical Research Letters*, 38, L01707, doi: 10.1029/2010GL045850.

4.1 Summary

Climate commitment—the warming that would still occur given no further human influence—is a fundamental metric for both science and policy. It informs us of the minimum climate change we face and, moreover, depends only on our knowledge of the natural climate system. Studies of the climate commitment due to CO_2 find that global temperature would remain near current levels, or even decrease slightly, in the millennium following the cessation of emissions. However, this result overlooks the important role of the non-CO_2 greenhouse gases and aerosols. Here we show that global energetics require an immediate and significant warming following the cessation of emissions as aerosols are quickly washed from the atmosphere, and the large uncertainty in current aerosol radiative forcing implies a large uncertainty in the climate commitment. Fundamental constraints preclude Earth returning to pre-industrial temperatures for the indefinite future, making climate change from CO_2 emissions essentially irreversible on human timescales. These same constraints mean that observations are currently unable to eliminate the possibility that we are already beyond the point where the ultimate warming will exceed dangerous levels. Global climate models produce a narrower range of climate commitment, but undersample observed forcing constraints.

4.2 Introduction

Our ability to predict future climate changes rests fundamentally on two factors: firstly, how our future human activities will influence climate forcing and secondly, how our models

of the climate system translate that forcing into climate change. The first factor depends on societal choices beyond the scope of science. The second factor depends on our confidence in the climate models. In turn, this confidence is predicated on the ability of the models to reproduce past climate changes, given our knowledge of previous human (and other) influences.

The concept of a 'climate commitment'—the climate change that would still occur given no further human influence—has proven useful in distinguishing between these two factors of climate prediction. It allows for a clear separation between the uncertainties in our physical climate models, which we wish to study, and the highly-uncertain future human influence on climate. The climate commitment can also be regarded as the minimum climate change we are consigned to because of human activities already undertaken.

Early efforts to estimate climate commitment considered the additional warming that occurs as the climate system comes into equilibrium with the present atmospheric composition and radiative forcing. Under this assumption, an additional warming of about 0.6°C is 'in the pipeline' due to the thermal inertia of the world oceans [54–56], committing us to future climate change that approaches 'dangerous' levels [35, 122, 123].

There has recently been a resurgence of interest in the climate commitment [35, 53, 59, 60, 133] in which an alternative, 'zero emissions', definition has been proposed. Under zero emissions, the atmospheric composition changes according to natural processes, and future warming is determined by only the physical inertia of the climate system and the residual greenhouse gas climate forcing. Matthews and Weaver [60] argue that this definition is the correct measure of the present climate commitment. They make the worthwhile and important point that the previous measure—constant climate forcing—conflates the physical response of the climate system to past emissions with the response to the future emissions that are necessary to maintain a constant atmospheric composition.

Several studies [53, 59, 60] consider the zero-emissions commitment with respect to CO_2. Carbon dioxide is naturally removed from the atmosphere on multiple timescales. Under zero emissions, CO_2 would fall off to about 40% of its peak enhancement above pre-industrial levels within a few centuries [53], while full recovery would occur over hundreds of thousands of years [52]. Effectively then, this residual 40% defines the ultimate radiative forcing

($\equiv R_\infty$) with which the climate must come into equilibrium. In such a zero emissions scenario, global average surface temperature is projected to remain near current levels, or even decrease slightly, in the millennium following the cessation of emissions [53, 59, 60]. However, these studies have overlooked the important role of the non-CO_2 greenhouse gases (such as methane and nitrous oxide) and aerosols. Aerosols are widely known to be one of the chief uncertainties in the modern climate, and make a considerable difference to the answer. Ramanathan and Feng [35] do consider the effect of removing anthropogenic aerosols, however they fix CO_2 at modern levels. The full consequences of the cessation of human activities must include both influences.

4.3 Transient and ultimate climate commitment

Following the elimination of emissions, aerosols would fall to their pre-industrial levels on timescales of days to weeks [58], while the non-CO_2 greenhouse gases would persist for decades to centuries [53, 58]. The sudden loss of the cooling effect of aerosols would result in a rapid transient warming as the surface temperature adjusts to the full greenhouse gas radiative forcing. Due to this significant transient warming, we propose two separate measures of climate commitment: a 'transient commitment', defined by the peak temperature following the cessation of emissions; and an 'ultimate commitment', defined by the temperature once the climate system has fully equilibrated with the persistent fraction of the CO_2 radiative forcing.

How well constrained is the climate commitment? Conservation of energy must obviously apply to the global energy budget, a linearization of which is

$$H = \lambda T + R, \tag{4.1}$$

where λ is the climate feedback parameter (simply related to climate sensitivity via Eq. (1.3)), T is the global average surface temperature anomaly (above pre-industrial), R is the radiative forcing, and H is the ocean heat uptake (see *Chap. 1* for details).

For a permanent forcing R_∞, H must ultimately go to zero giving an ultimate commitment of

$$T_\infty = -\lambda^{-1} R_\infty. \tag{4.2}$$

Eliminating λ gives

$$T_\infty = \frac{R_\infty}{R - H} T. \tag{4.3}$$

Thus, T_∞ depends only on observed constraints (T, H, and R) and the ultimate forcing (R_∞).

The IPCC Fourth Assessment Report (AR4) outlines observed constraints for the current climate (see the appendix). Global measurements of surface temperature change since pre-industrial give $T = 0.76 \pm 0.11\,^\circ\mathrm{C}$ (1σ) [138]. Recent observations show a robust warming of the global upper ocean [139] and Antarctic Bottom Water [140], together giving $H = 0.74 \pm 0.08$ W m^{-2} (1σ). Observed R is approximately 1.72 W m^{-2} (0.72 W m^{-2} to 2.52 W m^{-2}, 90% bounds) [58]. Therefore, T and H are well constrained, R less so. Uncertainties in aerosols (-0.5 W m^{-2} to -2.2 W m^{-2}) [58] dominate the uncertainty in R (Fig. 4.5 in the appendix), and thus dominate the uncertainty in T_∞.

4.4 Upwelling-diffusive ocean energy balance model

The time evolution of climate requires a representation of the ocean, for which we use a simple one-dimensional upwelling-diffusion model. The model is the same as that in Baker and Roe [124], which is similar in form to those used in previous studies [125–129]. As described in Baker and Roe [124], the ocean has a simple structure consisting of a surface mixed layer of depth h, density ρ and specific heat C_p. Heat is exchanged between the surface and the ocean layer immediately below according to a thermal conductivity κ. Vertical heat transport throughout the ocean is governed by the combined effects of a diffusivity χ and an upwelling velocity ω.

The time-evolution of surface temperature T is governed by

$$\rho C_p h \frac{dT}{dt} + \kappa \left.\frac{\partial T_o}{\partial z}\right|_{z=0} = R + \lambda T, \tag{4.4}$$

where $T_o(z,t)$ is the ocean temperature anomaly at depth z and $T_o(0,t) = T(t)$. Note that the left hand side of Eq. (4.4) is a representation of the time rate of change of global heat content, equal to H in Eq. (4.1). The temperature anomaly in the interior ocean is governed by

$$\frac{\partial T_o}{\partial t} = \chi \frac{\partial^2 T_o}{\partial z^2} - \omega \frac{\partial T_o}{\partial z}. \tag{4.5}$$

Table 4.1: Upwelling-diffusive ocean model parameters and transient climate response. The standard parameter values are listed in bold. Two sets of perturbed parameter values are listed for use in ocean model sensitivity experiments in Section *4.6*. Transient climate response (TCR) is the warming at CO_2 doubling in 1% yr^{-1} ramping experiments[a].

Model parameter	Units	Symbol	Values
Mixed layer depth	m	h	**75** , 75 , 75
Ocean bottom depth	m	D	**4000** , 4000 , 4000
Ocean diffusivity	$m^2\ s^{-1}$	χ	$\mathbf{1.5 \times 10^{-4}}$, 1.0×10^{-4} , 0.75×10^{-4}
Upwelling rate	$m\ s^{-1}$	ω	$\mathbf{-1.3 \times 10^{-7}}$, -0.8×10^{-7} , -0.55×10^{-7}
Conductivity[b]	$W\ m^{-1}\ K$	κ	**628** , 419 , 314
TCR	°C		**1.3** , 1.5 , 1.7

[a] λ is set to a value of 1.05 $Wm^{-2}K^{-1}$ (corresponding to a 3.5 °C climate sensitivity) when calculating TCR.

[b] We set $\kappa = \rho C_p \chi$ here.

Also included in the model is a term of the form $\rho C_p \omega [T(t) - T_o(D,t)]$, which simulates the effect of changing bottom water properties through the direct transfer of heat from the surface to the ocean bottom at depth D. A zero-flux boundary condition is applied at the ocean bottom.

The ocean model equations are solved numerically given the parameters specified in Table 4.1 and values for λ and $R(t)$ as described below. Such models are robust, and successfully reproduce observations of ocean heat uptake at the global scale [129].

4.5 Results

4.5.1 Climate commitment from past greenhouse gas emissions

The weak bounds on aerosols means a broad envelope of uncertainty in total forcing over the industrial era. This is illustrated in Fig. 4.1a, where an idealized representation of forcing trends has been employed. Forcing reaches its modern value in year 2012, and from then on a climate commitment scenario is assumed. Once emissions are terminated,

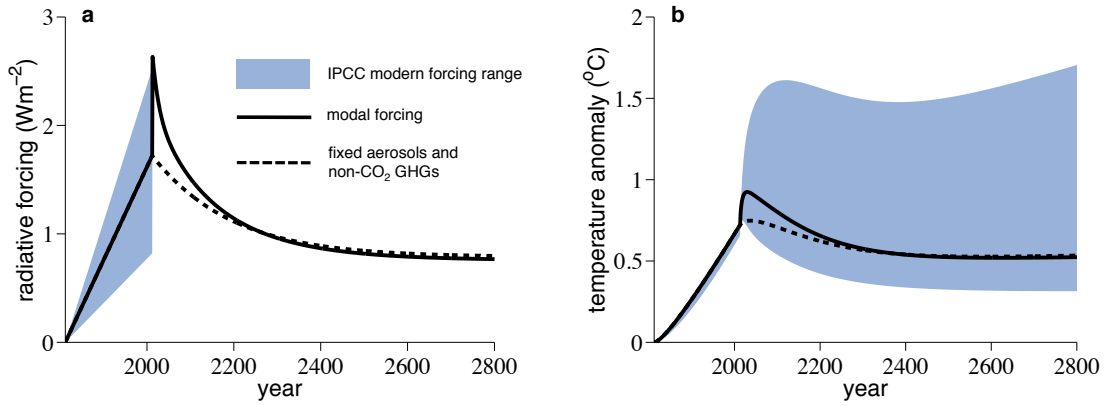

Figure 4.1: Observational constraints on climate forcing and temperature response. **a**, Idealized representation of forcing trends. Forcing is ramped linearly to its modern value in year 200, and a zero emissions scenario is assumed thereafter. The light blue shading is the 90% confidence interval on trajectories of R as allowed by observations, where only uncertainty in aerosols is considered. The solid black line shows the modal value of R. The dashed black line shows a scenario in which aerosols and non-CO_2 greenhouse gases are held fixed at their modern concentrations upon the elimination of CO_2 emissions. **b**, As for **a**, but modeled temperature response. Values of λ have been paired with values of R (through Eq. (4.1)) so that individual temperature trajectories are tightly constrained, analogous to the situation for modern observations.

R is governed by the respective decay timescales of the various atmospheric constituents. Aerosols and tropospheric ozone are specified to fall to pre-industrial levels immediately. Long-lived greenhouse gases decline at their respective (e-folding) timescales [58]: 12 years for methane; 114 years for nitrous oxide; 75 years (a representative lifetime) for halocarbons. Carbon dioxide falls to 40% of its peak value (above pre-industrial) with a decay timescale of 170 years [58]. Radiative forcing is calculated using the simplified expressions of Myhre *et al.* [73].

From Eq. (4.1) the relatively strong constraints on T and H mean that R and λ can be thought of as pairs wherein strong (weak) aerosol forcing is balanced by high (low) climate sensitivity. This compensation occurs within AR4 and older models [130–132]. Figure 4.1b shows temperature trajectories for pairs of R and λ, whereby past temperature trends are approximately reproduced. It is a graphical representation of the inherent trade-off

between uncertainties in climate forcing and uncertainties in global temperature following the cessation of emissions: even though past temperature changes are well constrained and future forcing (under zero emissions) well understood, uncertainty in past forcing implies uncertainty in future temperatures.

It is important to emphasize that R and λ are not independent. In other words, a high climate sensitivity and a low aerosol forcing are inconsistent with the observed constraints on surface temperature and ocean heat uptake. Two recent studies that consider the effects of the loss of aerosols [35, 133] treat R and λ as independent, and also fail to span the full range of either R or λ. This has the effect of producing a narrower range of climate commitment than allowed by propagating the observed constraints through Eq. (4.3).

We next reproduce and explain the results of previous studies [53,59,60] that considered climate commitment with respect to only CO_2 emissions (non-CO_2 greenhouse gases and aerosols remain at their modern concentrations). For modal estimates of modern radiative forcing, this gives $R_\infty \approx 0.8$ W m^{-2}. The dashed black lines in Fig. 4.1 show this forcing and the response—a gentle decline in temperature following the cessation of CO_2 emissions. The result follows directly from surface energetics (Eq. (4.3)): R_∞ is very near the modal value of the current surface forcing ($R - H \approx 1$ W m^{-2}) so the ratio of forcings (i.e., $R_\infty/(R-H)$) and therefore the ratio of the responses (i.e., T_∞/T) is near, but slightly less than, one.

Turning now to the case in which all anthropogenic emissions cease, there is an immediate unmasking of greenhouse gas forcing as aerosols are quickly washed from the atmosphere. The effect is an abrupt rise in climate forcing (Fig. 4.1a) to a peak value of around 2.7 W m^{-2}, which is relatively well constrained as it depends only on greenhouse gases. The response is a rapid warming (Fig. 4.1b), with a transient commitment of up to 0.9 °C above the modern temperature. Thereafter, forcing declines over the next few centuries as greenhouse gases are partially, but not completely, removed from the atmosphere. At the low end of the climate response, temperature falls to less than half of its peak value, but never back to its pre-industrial level. At the high end, temperature continues to increase because the system has not yet attained equilibrium due to the long adjustment timescales of high sensitivity systems [98, 124].

The long-term temperature response depends only on modern surface energetics and R_∞. Figure 4.1 accounts only for uncertainties in aerosols. This gives an ultimate commitment (above pre-industrial) of $T_\infty = 0.6\,^\circ\mathrm{C}$ with a 90% confidence range of $0.3\,^\circ\mathrm{C}$ to $7.2\,^\circ\mathrm{C}$, which follows directly from Eq. (4.3) or by integrating the climate model to equilibrium.

The lower bound on climate commitment is robust due to the form of Eq. (4.3). On the other hand, the upper bound is very sensitive to uncertainties in observed global energetics and R_∞ (see the appendix). We do not account here for uncertainties in the biogeochemical cycle (e.g., uncertainty in the lifetimes of greenhouse gases or the residual atmospheric CO_2 concentration). We also neglect the effects of slow climate feedbacks (e.g., carbon cycle feedbacks or surface albedo changes associated with ice sheet loss and vegetation changes), which would amplify future warming by a potentially large but uncertain amount [122,123]. Moreover, following the IPCC, we have taken the 90% confidence interval on aerosol climate forcing: if one were to factor in other sources of uncertainty, in either ocean heat uptake or greenhouse gas forcing, or use more conventional statistical bounds (i.e., a 95% range), one could not rule out the disconcerting possibility that the observed 20th century warming has transpired with little to no effective surface forcing (i.e., $R \approx H$).

4.5.2 Alternative constraints on committed warming

The above analysis showed that current observational constraints allow the possibility of a very large climate commitment. Do narrower bounds exist? The ultimate commitment can alternatively be expressed as a function of λ (Eq. (4.2)), reasonable bounds on which can be inferred from IPCC AR4 in terms of a 'likely' ($> 66\%$ probability) and 'very likely' ($> 90\%$ probability) range for climate sensitivity [71]. Exploiting the fundamental relationship between R and λ, and reversing the above arguments, these IPCC constraints on λ provide constraints on R (Fig. 4.2a). Any value of λ within the IPCC range still implies a significant transient warming (Fig. 4.2b), and there remains a substantial uncertainty in the ultimate commitment (though the range is smaller than that based on observational constraints).

The ability of the IPCC AR4 fully-coupled climate models (hereafter AR4 models) to reproduce 20th century surface temperature [132] and ocean heat uptake [59], under sub-

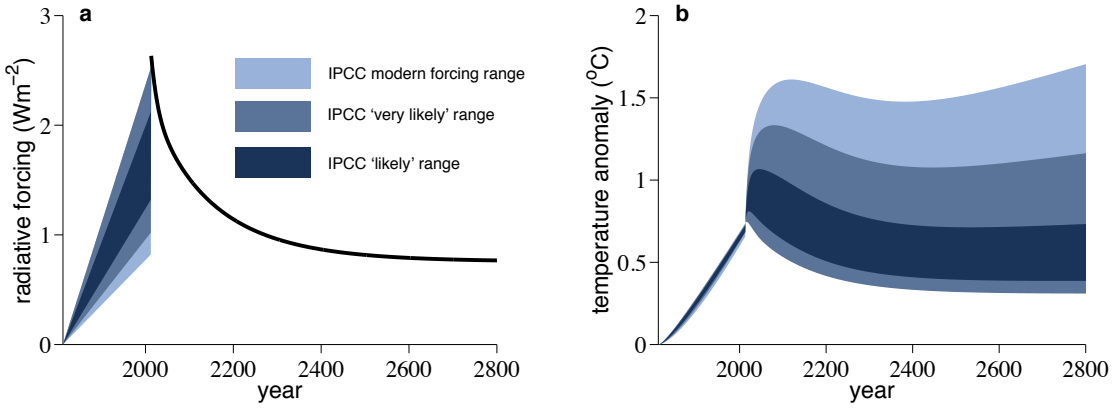

Figure 4.2: Constraints on forcing and temperature response from IPCC climate sensitivity. a, Radiative forcing and **b,** Temperature response, as in Fig. 4.1. The dark blue shading shows the IPCC AR4 'likely' range of climate sensitivity (2 °C to 4.5 °C). The medium blue shading shows the IPCC AR4 'very likely' range of climate sensitivity (1.5 °C to 10 °C—IPCC AR4 [71] truncates the probability distributions of climate sensitivity at 10 °C so we take this value as representative of the upper bound on the 'very likely' range). For comparison, the light blue shading shows the 90% confidence interval as allowed by observations, as in Fig. 4.1. A wedge in the lower range of possible forcing translates to a wedge in the higher range of possible temperature response.

stantial aerosol uncertainty, has been suggested to give a false sense of the accuracy with which future climate can be predicted [131]. However, AR4 models have achieved consistency with the observational record, in part, through compensation between R and λ [132]. As argued by Knutti [132], such model tuning—whether explicit or implicit—is not problematic provided that we interpret models as conditional on observations. In other words, models satisfy Eq. (4.1) subject to relatively tight constraints on T and H. Accurate simulation of 20th century climate may then be viewed as a necessary, but not sufficient, condition for the ability to simulate future climate, and does not alone create overconfidence in model skill. Indeed, the light blue trajectories in Fig. 4.2b clearly demonstrate the ability, with a model, to reproduce the 20th century temperature record yet still span the full range of uncertainty in climate commitment as allowed by observations.

The difference between the AR4 model range of climate commitment and the range allowed by observations can instead be attributed to an inconsistency between R in models

and R in observations (see the appendix)—the range of forcing among the different AR4 models [132] spans only the 'likely' range of forcing in Fig. 4.2a. How can models and observations be reconciled? One way would be to achieve substantially more accurate observations of the Earth's radiative budget. In particular, emphasis should be placed on ruling out the very low values of R that correspond to very high values of committed warming.

The alternative approach is to create populations of climate models that deliberately exploit tuning to fully span the uncertainty in climate forcing (and the implied range of climate sensitivity necessary to reproduce the observed temperature record), and then to demonstrate that some pairs of R and λ are inconsistent with some aspect of either the instrumental record (e.g., interannual variability, seasonal variability, spatial patterns of warming, or volcanic eruptions), or reconstructions of past climates. Studies that pursue this approach produce a variety of distributions for climate sensitivity, many narrower than that inferred from observational constraints, some narrower than even the IPCC 'likely' range [67,68,71,72]. An implication then, would be that the range of uncertainty in the climate commitment could be narrowed as well. Achieving convergence among these different distributions depends on understanding the differing assumptions and structural uncertainties in, and the interdependence of, the respective frameworks [67, 72, 134, 135]. Arguably, an important measure of the value added by models will be when the consensus is reached that such studies provide narrower constraints on the modern climate forcing than that currently provided by direct observations. The discrepancy between the reported ranges of uncertainty in climate sensitivity and observations of aerosol forcing is an important one for future rounds of the IPCC reports to resolve. Until then, model-based estimates should be treated carefully, and probably represent an undersampling of the possible climate commitment.

4.6 Sensitivity of transient climate commitment to ocean model parameters

While simple upwelling-diffusive climate models, such as the one used here, are able to reproduced observed climate trends, they do not accurately capture the complexities of ocean heat uptake at the regional scale [136] and likely underestimate the long-term temperature

response to forcing (see *Chap. 5*). Moreover, the model's rate of global temperature under transient forcing is at the very low end of the range supported by fully-coupled GCMs. A measure of this is the so-called *transient climate response* (TCR), defined as the warming at the time of CO_2 doubling in idealized 1% yr^{-1} CO_2 ramping experiments[1]. Under the standard set of ocean model parameters (Table 4.1) the model's TCR is 1.3 °C, while the range reported by AR4 GCMs is 1.3–2.7 °C [7, 137]. This suggests that the temperature trajectories in Figs. 4.1 and 4.2 should be viewed as lower bounds on the transient climate commitment. Indeed, when the ocean diffusivity and upwelling rate are varied to produce TCRs of 1.5 °C and 1.7 °C (see Table 4.1), the transient commitment over the next century increases to about 1.2 °C and 1.5 °C above the modern temperature, respectively (blue shading in Fig. 4.3)[2].

While the details of any particular temperature trajectory are thus model dependent, the overall form of the temperature response is a fundamental consequence of three basic and robust climate properties: the unmasking of climate forcing by the loss of anthropogenic aerosols, the long lifetime of greenhouse gases in the atmosphere, and the thermal inertia of the ocean. It is important to emphasize that the long-term temperature response depends only on modern surface energetics and the residual CO_2 concentration (Eq. (4.3)) and is thus independent of the timescales of climate response.

4.7 Discussion

4.7.1 A note on CO_2 targets

Evidence from the Earth's climate history indicates that if substantial changes in ice sheets and sea level are to be avoided over the coming centuries, future warming should be limited to less than about 1 °C above the modern temperature (1.7 °C above pre-industrial) [123]. Based on the committed warming from the current atmospheric composition [54] and estimates of the additional warming that would occur due to slow climate feedbacks (e.g., ice

[1] Since TCR depends on λ, we report values of TCR for $\lambda = 1.05$ $Wm^{-2}K^{-1}$ (corresponding to a equilibrium climate sensitivity of 3.5 °C).

[2] A TCR of 1.7 °C requires ocean parameters that lie at the edge the range suggested by previous studies [125–129], as reported in Baker and Roe [124]. Higher values of TCR could be attained by extending the model to include land and other fast components of the climate system.

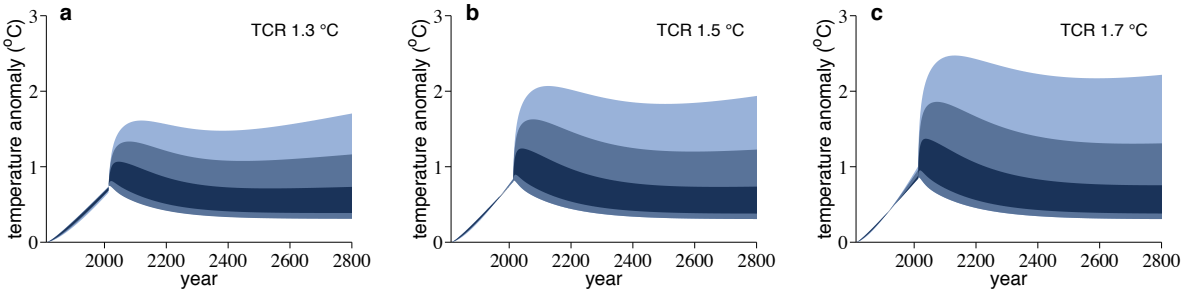

Figure 4.3: Sensitivity of future temperature response to transient climate response. Temperature response to zero emissions for **a,** TCR = 1.3 °C (as in Fig. 4.2b), **b,** TCR = 1.5 °C and **c,** TCR = 1.7 °C. As in Fig. 4.2, the light blue shading shows the 90% confidence interval as allowed by observations, the medium blue shading shows the IPCC AR4 'very likely' range of climate sensitivity (1.5 °C to 10 °C) and the dark blue shading shows the IPCC AR4 'likely' range of climate sensitivity (2 °C to 4.5 °C). Values of λ have been paired with values of R according Eq. (4.1) and observed constraints on T and H.

sheet disintegration, vegetation changes and carbon cycle feedbacks), it has been suggested that avoiding such dangerous levels of warming requires stabilization of atmospheric CO_2 near 350 ppmv [122].

Since lowering atmospheric CO_2 to 350 ppmv or less would require near-zero future emissions, it is natural to reevaluate this target in the context of the results presented here. The radiative forcing at 350 ppmv ($R_{350} \approx 1.2$ Wm^{-2}) can be compared to the current effective surface forcing ($R - H \approx 1$ Wm^{-2} for a modal value of R) suggesting 350 ppmv stabilization at a temperature slightly warmer than the present (by a factor $T_\infty/T = R_{350}/(R - H) \approx 1.2$), neglecting slow climate feedbacks. However, if due to a large aerosol forcing R is near the low end of its observed range, the combined effects of removing all non-CO_2 GHGs and lowering atmospheric CO_2 to 350 ppmv would be more than offset by the loss of aerosol cooling, resulting in a substantially warmer climate than present[3]. Through simple energetic constraints, any target level of CO_2 that constitutes "safe" climate stabilization must depend directly on the modern climate forcing value, and thus share its considerable uncertainty.

[3]The range of possible future climates in a 350 ppmv scenario resembles that in Fig. 4.1 (blue shading), which shows stabilization to an ultimate CO_2 concentration of around 325 ppmv.

4.7.2 Concluding remarks

The results presented here depend only on three straightforward and well-understood aspects of climate: the net cooling effect of aerosols, the large spread of uncertainty in aerosol forcing (or, equivalently, climate sensitivity), and the long atmospheric lifetimes CO_2 and other greenhouse gases. In combination they lead to considerable uncertainty in the transient and ultimate climate commitments. An immediate and significant warming would follow the cessation of emissions as aerosols are quickly washed from the atmosphere, and global temperature would remain elevated (above pre-industrial levels) for the indefinite future, making climate change from CO_2 emissions essentially irreversible on human timescales.

Our focus on the present climate commitment leads to one particular value of R_∞. Of course, in any practical scenario, emissions will continue and R_∞ will grow. In turn, the transient and ultimate climate commitments will increase and become more uncertain. Inasmuch as a substantially improved understanding of the role of aerosols in climate remains elusive, so will our ability to constrain future climate. In order to rule out the possibility that we already face a disturbingly large climate commitment, we need to rule out the possibility that the observed climate change has been driven by a climate forcing at the lower end of the range that is currently permitted by observations.

4.8 *Appendix: estimates of climate sensitivity from observations and model feedbacks*

Gerard H. Roe and Kyle C. Armour (2011), How sensitive is climate sensitivity? *Geophysical Research Letters* 38, L14708, doi: 10.1029/2011GL047913.

Much effort has gone into evaluating global climate sensitivity ($\equiv T_{2\times}$), through both estimates of individual climate feedbacks [74–78] and measurements of past and present global energy budgets [66–70]. However, because both approaches involve inherent uncertainties, we cannot establish a single value of $T_{2\times}$ but only its probability density function (pdf), defined here as $p_{T_{2\times}}$.

Following Roe and Baker [74], computation of $p_{T_{2\times}}$ can be made from estimates of linear feedbacks within climate models. From Eq. (1.3), the pdfs of $T_{2\times}$ and λ are related by:

$$\begin{aligned} p_{T_{2\times}} &= p_\lambda(\lambda(T_{2\times})) \cdot \frac{d\lambda}{dT_{2\times}} \\ &= p_\lambda(-\frac{R_{2\times}}{T_{2\times}}) \cdot \frac{R_{2\times}}{(T_{2\times})^2}. \end{aligned} \tag{4.6}$$

Climate feedbacks calculated individually and summed within a range of GCMs [75, 77, 78] produce an approximately normally distributed p_λ, characterized by $\overline{\lambda} \pm \sigma_\lambda = -1.13 \pm 0.42$ W/m^2/K [74]. The resulting estimate $p_{T_{2\times}}$ (black line in Fig. 4.4) is highly skewed, with finite probabilities of very large climate sensitivity. This result is fundamental to the feedback analysis: due to the form of Eq. (1.3)—with λ in the denominator—symmetric uncertainty in feedbacks leads to asymmetric amplification of the temperature response and skewing of $p_{T_{2\times}}$ [74]. Note that the overall shape of $p_{T_{2\times}}$ does not change substantially under modest narrowing or skewing of p_λ [95].

Alternatively, estimates of $p_{T_{2\times}}$ can be made purely from observations of the modern climate (T_{obs}, R_{obs}, and H_{obs}). From equations (1.3) and (1.8):

$$T_{2\times} = \frac{T_{obs} R_{2\times}}{R_{obs} - H_{obs}}. \tag{4.7}$$

Simplifying notation, let $F_{obs} = R_{obs} - H_{obs}$. Pdfs of these quantities are related by:

$$\begin{aligned} p_{T_{2\times}} &= \int_0^\infty p_{F_{obs}} \cdot p_{T_{obs}}\left(T_{obs}(T_{2\times})\right) \cdot \frac{dT_{obs}}{dT_{2\times}} \cdot dF_{obs} \\ &= \int_0^\infty p_{F_{obs}} \cdot p_{T_{obs}}\left(\frac{T_{2\times} F_{obs}}{R_{2\times}}\right) \cdot \frac{F_{obs}}{R_{2\times}} \cdot dF_{obs}. \end{aligned} \tag{4.8}$$

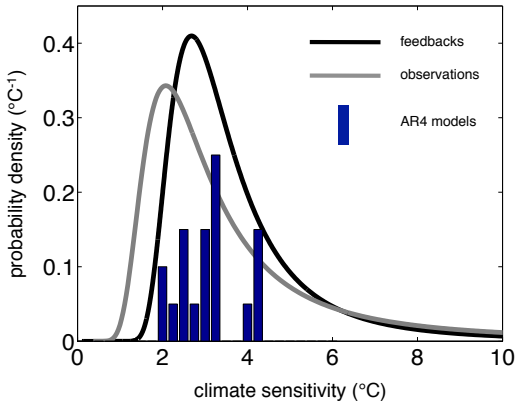

Figure 4.4: Probability distribution functions of climate sensitivity. Computed from model-estimated climate feedbacks (black) [74] and observations of the modern climate (gray). A histogram of $T_{2\times}$ from IPCC AR4 models [6, 7] is also shown for reference. All pdfs are normalized between 0 and ∞.

where $p_{F_{obs}}$ and $p_{T_{obs}}$ are the pdfs of the observations.

The IPCC Fourth Assessment Report (AR4) outlines observed constraints for the current climate. Global measurements of surface temperature change since pre-industrial give $\overline{T}_{obs} \pm \sigma_T = 0.76 \pm 0.11\,^{\circ}\mathrm{C}$ [138]. Recent observations show a robust warming of the global upper ocean [139] and Antarctic Bottom Water [140], together giving $\overline{H}_{obs} \pm \sigma_H = 0.74 \pm 0.08$ W m^{-2}.

Observed R_{obs} is summarized in Fig. 4.5. Solar irradiance changes since the pre-industrial period have caused a small radiative forcing of 0.12 W m^{-2}, with a 90% confidence range of -0.06 W m^{-2} to 0.18 W m^{-2} [58]. Total anthropogenic radiative forcing is approximately 1.6 W m^{-2} (0.6 W m^{-2} to 2.4 W m^{-2}) [58]. Uncertainties in aerosols (-0.5 W m^{-2} to -2.2 W m^{-2}) [58] dominate the uncertainty in R_{obs} (Fig. 4.5), and thus dominate the uncertainty in $T_{2\times}$. Note that this aerosol radiative forcing estimate includes only direct and indirect cloud albedo aerosol effects. The former, involving the direct reflection of sunlight by aerosol particles, is relatively well constrained. The latter, involving the indirect effect of aerosols on planetary albedo through changes in cloud nucleation, is poorly constrained

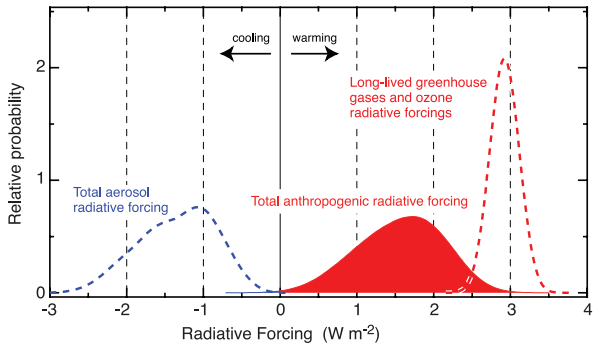

Figure 4.5: IPCC estimates of aerosol, greenhouse gas and total radiative forcing. Reproduced from IPCC AR4 [58]. The aerosol radiative forcing estimate includes only direct and cloud albedo effects.

due to uncertain cloud physics. If the aerosol semi-direct effect, cloud lifetime effect, and indirect effect on mixed phase clouds were included, the aerosol forcing would be more negative and more uncertain [58, 141].

In sum, the observed forcing pdf, $p_{F_{obs}}$, is approximately normally distributed and characterized by $\overline{F}_{obs} \pm \sigma_F = 0.90 \pm 0.55$ Wm^{-2}. The resulting estimate $p_{T_{2\times}}$ (gray line in Fig. 4.4) is again skewed toward high climate sensitvity. This result follows from the form of Eq. (4.7) and the fact that the fractional uncertainty in F_{obs} is much larger than the fractional uncertainty in T_{obs}; it is robust to modest narrowing or skewing of p_F [95]. Note that relatively narrower constraints on temperature than forcing is a common feature of climate observations and reconstructions [67].

Although observation-based and feedback-based approaches rely on very different types of information, they produce remarkably consistent estimates of $T_{2\times}$ (Fig. 4.4). If they differed substantially, it might perhaps imply that there was important unused information, or that there were troubling biases among different methods. Another reason for their similarity is also worth emphasizing. From Eqs. (1.5) and (1.8):

$$\underbrace{R}_{\text{(i)}} - H = -\lambda T = \underbrace{-\sum_{\alpha} \lambda_\alpha}_{\text{(ii)}} T. \tag{4.9}$$

As noted above, H and T are well constrained in the current climate. Term (i) on left-hand

side of Eq. (4.9) reflects the principal source of uncertainty in global-mean energetics (i.e., radiative forcing), and term (ii) on the right-hand side reflects the uncertainty in radiative response to forcing (i.e., climate feedbacks). Eq. (4.9) shows that these two approaches are equivalent to each other. Therefore, because p_R is broad (relative to p_H and p_T) and nearly symmetric (e.g., Fig. 4.5) p_λ should be too. Moreover, to the extent that ensembles of models (1) adequately simulate observed T and H and (2) faithfully represent the observed forcing uncertainties, the modeled p_λ must behave similarly.

Figure 4.4 (blue bars) shows that the AR4 model ensemble undersamples $p_{T_{2\times}}$. From an energy balance perspective (i.e., Eq. (1.8)) this is due to an undersampling of p_R arising from too narrow a range of simulated aerosol forcing [132]. From a feedbacks perspective (i.e., Eq. (1.5)) this is due to an undersampling of p_λ arising from (possibly unphysical) correlations between different climate feedbacks [142].

Chapter 5

TIME-VARYING CLIMATE SENSITIVITY FROM REGIONAL FEEDBACKS

Kyle C. Armour *et al.* (2012) Time-varying climate sensitivity from regional feedbacks. *In preparation.*

5.1 Summary

The sensitivity of global climate with respect to forcing is generally described in terms of global climate feedback, a measure of the global radiative response per degree global annual mean surface temperature change. While the global climate feedback is often assumed to be constant, its value, diagnosed within general circulation climate models (GCMs), shows substantial time-variation under transient warming. The potential for the global climate feedback to vary over time has implications for our ability to constrain future climate changes from observations of past and present climate states, and introduces a substantial source of uncertainty in future climate projections. Using (i) a fully-coupled GCM and (ii) a low-order energy balance model, we show here that the global climate feedback is fundamentally related to the geographic pattern of regional climate feedbacks and the geographic pattern of surface warming at any given time; time-variation of global climate feedback arises naturally when the pattern of surface warming evolves over time, activating regional feedbacks of different strengths. Climate sensitivity at the global scale is thus fundamentally tied to the pattern of warming at the regional scale. The findings have implications for the quantification of radiative forcing, climate feedbacks, and climate sensitivity within both models and observations. We discuss these results in the context of previous studies, and emphasize a strong connection to the concept of 'ocean heat uptake efficacy' [137].

5.2 Introduction

Earth's climate is widely characterized in terms of its global annual mean surface temperature, and its response to forcing is often described in terms of *climate sensitivity* ($\equiv T_{2\times}$), the global equilibrium surface warming under a doubling of atmospheric CO_2. This definition has facilitated direct comparison of different estimates of climate change, be they instrumental, proxy, or model derived (e.g., Hegerl *et al.* [71]; Allen *et al.* [67]; Edwards *et al.* [68]; Knutti and Hegerl [72], and references therein). Moreover, climate sensitivity describes climate changes occurring on centennial and longer timescales [124, 143, 144] and is thus a useful and conceptually convenient diagnostic for the long-term evolution of global climate under forcing.

On decadal to centennial timescales, global climate response to forcing is an inherently transient phenomenon that depends on several factors in addition to the equilibrium climate sensitivity. The rate of heat uptake by the deep ocean strongly influences transient warming by acting as a sink of energy at the surface [145]. Moreover, the stability of global climate with respect to forcing, described by the global climate feedback at any given time [61], may itself be a variable quantity. We thus define the *effective* global climate feedback parameter $\lambda_{eff}(t)$ to be the instantaneous global radiative response per degree global mean surface temperature change (units of $\mathrm{Wm}^{-2}/\mathrm{K}$). Under transient warming, λ_{eff} may be different from the *equilibrium* global climate feedback parameter λ_{eq}, defined as the ratio of the global radiative forcing from CO_2 doubling ($\equiv R_{2\times}$) to the resulting equilibrium response of global mean surface temperature $T_{2\times}$:

$$\lambda_{eq} = -\frac{R_{2\times}}{T_{2\times}}. \tag{5.1}$$

Climate change on a global scale is widely described through a simple linearization of the global top-of-atmosphere (TOA) energy balance:

$$\overline{H}(t) = \lambda_{eff}(t)\overline{T}(t) + \overline{R}(t), \tag{5.2}$$

where the net TOA energy flux $\overline{H}$ is equal to the sum of the radiative forcing $\overline{R}$ (positive downward) and the effective global radiative response $\lambda_{eff}\overline{T}$ (assumed to be proportional

to the global mean surface temperature anomaly $\overline{T}$). Each term in Eq. (5.2) represents a global mean quantity (denoted by an overbar) and is a function of time t. $\overline{H}$ may also be regarded as the rate of global heat content change, which on decadal and longer timescales is approximately equal to the heat flux into the world ocean, the primary heat reservoir in the climate system [84].

The effective climate feedback λ_{eff} is generally framed in terms of its corresponding *effective climate sensitivity* [146], defined by

$$T_{eff}(t) = -\frac{R_{2\times}}{\lambda_{eff}(t)}. \tag{5.3}$$

T_{eff} is the apparent climate sensitivity (equilibrium surface warming due to a CO_2 doubling) as diagnosed by global energy balance (Eq. (5.2)) at any given time, under the assumption that λ_{eff} maintains a constant value as global climate equilibrium is reached [146]. If the effective climate feedback had no time-dependence, as is often assumed for global climate perturbations of a few degrees [72], then $T_{eff} = -R_{2\times}/\lambda_{eq} = T_{2\times}$ at all times. However, substantial time-variation of λ_{eff} under transient global warming has been diagnosed in a wide range of global climate models (GCMs) and forcing scenarios [88, 137, 145–153], implying that T_{eff} may be a substantial misdiagnosis of the climate sensitivity $T_{2\times}$.

While time-dependent λ_{eff} has been widely demonstrated [88, 137, 145–153], there is little agreement on the magnitude or mechanism of its variation. Winton *et al.* [137] show that the time-variation of λ_{eff} is responsible for a substantial portion of the spread in the *transient climate response* (defined as the warming at the point of CO_2 doubling in idealized 1% yr^{-1} ramping simulations) across a range of fully-coupled GCMs. Projection of global climate over the coming centuries thus depends not only on the equilibrium climate feedback parameter within models, but also fundamentally on how the sensitivity of global climate to forcing (λ_{eff}) evolves over time. Moreover, observations of different types of climate change (e.g., the instrumental record of recent warming, the observed climate response to volcanic eruptions, and proxy reconstructions of past climate states) must be interpreted as providing a measure of the effective climate sensitivity, which may take on a distinct value for each type of climatic variation even if a single $T_{2\times}$ meaningfully exists in nature. Variable λ_{eff} thus limits our ability to directly relate knowledge of climate changes from

different periods.

Several mechanisms for time-dependent climate sensitivity have been proposed. Senior and Mitchell [148] suggest that time-dependent cloud feedbacks arise from interhemispheric warming differences associated with the slow response of the Southern Ocean. Williams *et al.* [152] instead argue that time-dependent T_{eff} can be attributed to an 'effective forcing' R_{eff}, wherein local CO_2-induced atmospheric heating rates give rise to non-feedback cloud adjustments on timescales far more rapid than that of global surface warming [152,154–158], producing an effective 'tropospheric-adjusted' forcing that is distinct from the traditional measure of radiative forcing. Recently, Winton *et al.* [137] have proposed an alternative interpretation of T_{eff} and R_{eff} in terms of a time-dependent 'efficacy of ocean heat uptake', analogous to the distinct efficacies of different radiative forcing agents wherein each may drive a different global temperature response (per unit global radiative forcing) depending on its geographic forcing structure [85–87].

Here we show that the effective global climate feedback λ_{eff} (and corresponding effective climate sensitivity T_{eff}) is fundamentally related to the geographic pattern of regional climate feedbacks and the geographic pattern of surface warming at any given time. Time-variation of λ_{eff} emerges naturally as the pattern of warming evolves and regional feedbacks of different strengths are activated. This principle is demonstrated within (i) a state-of-the-art atmosphere–ocean general circulation model and (ii) a low-order energy balance climate model. We show that effective climate sensitivity, usually diagnosed via global energy balance considerations (Eq. (5.2)), can equivalently be calculated from the instantaneous spatial pattern of surface warming in combination with an estimate of the strength of regional climate feedbacks. This approach yields a physical interpretation of λ_{eff} and the mechanism of its time-variation. These findings are discussed in the context of previous studies, and a strong connection to the concept of ocean heat uptake efficacy is emphasized. Time-varying λ_{eff}, arising from regional climate feedbacks, has important implications for the quantification of radiative forcing, climate feedbacks, and climate sensitivity within both models and observations.

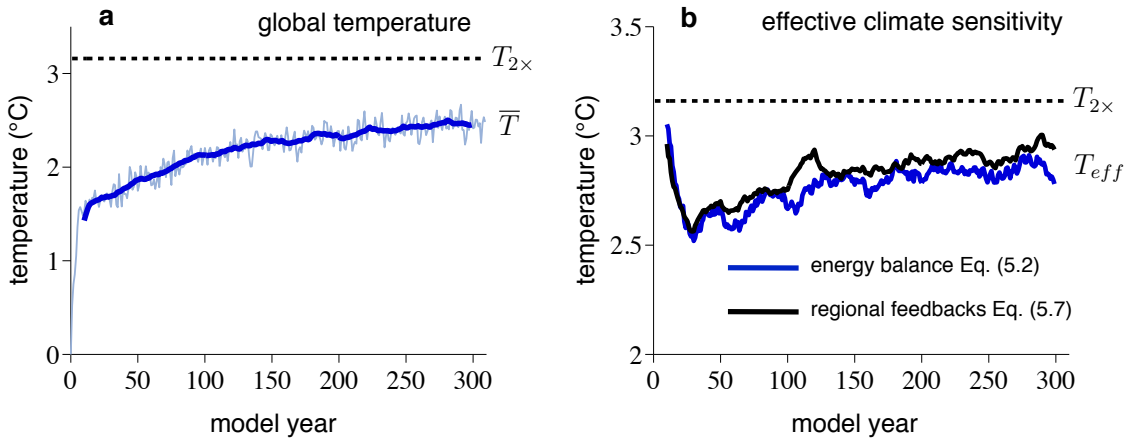

Figure 5.1: Evolution of global temperature and effective climate sensitivity within CCSM4. a, Global annual mean surface temperature $\overline{T}$, and **b,** effective climate sensitivity T_{eff} within CCSM4 following an abrupt doubling of atmospheric CO_2 in year zero. T_{eff} calculated by global energy balance (Eq. (5.2)) is shown in blue, and T_{eff} calculated with regional feedbacks (Eq. (5.7)) is shown in black. Thick lines show 10-year running means. Equilibrium climate sensitivity $T_{2\times}$ is estimated from slab ocean version of the model.

5.3 Time-varying climate sensitivity from global energy balance

Following previous studies [137, 152] we explore here the time-variation of effective climate feedback within an idealized instantaneous CO_2 doubling scenario, which has the property that climate forcing is held constant ($\overline{R} = R_{2\times}$) throughout the analysis. We use the fully-coupled Community Climate System Model version 4 (CCSM4) [159] forced by an abrupt CO_2 doubling in year zero, and measure the perturbed climate state with respect to the long 1850's 'control' simulation from which the simulation was branched. Figure 5.1a shows the global annual surface temperature response of CCSM4 following CO_2 doubling. T_{eff} as diagnosed by global energy balance (Eqs. (5.2)) varies considerably over the simulation (blue line in Fig. 5.1b). Under transient warming, the value of T_{eff} within CCSM4 is generally less than the equilibrium climate sensitivity $T_{2\times}$ (estimated here from the equilibrium temperature change under CO_2 doubling simulated with a 'slab ocean model' (SOM) version of CCSM4 that uses annually-repeating ocean heat flux convergence taken from the fully-coupled 1850's control simulation). This result is qualitatively similar to that in a wide

range of fully-coupled GCMs, though quantitive differences exist across models [137, 152].

Note that we wish to focus here on the mechanisms of T_{eff} variation that are not associated with fast tropospheric adjustment effects discussed by Williams *et al.* [152], and thus use an 'adjusted' CO_2 forcing in our calculation of T_{eff} (Eqs. (5.2) and (5.3)). We estimate the adjusted forcing to be $R_{2\times} \approx 3$ Wm^{-2} within CCSM4 based on feedbacks calculated by radiative kernels (see *Section 5.4.1*), and use this value throughout the analysis. It is in good agreement with estimates of the tropospheric-adjusted forcing diagnosed by other methods within CCSM3, the previous generation of this model (see Webb *et al.* [158], and references therein).

While global energy balance (Eq. (5.2)) allows a diagnosis of effective climate sensitivity within CCSM4, it does not provide insight into the mechanisms by which T_{eff} varies over the simulation. In the following section, we develop a regional feedback framework from which time-dependence of T_{eff} emerges naturally.

5.4 Time-varying climate sensitivity from regional climate feedbacks

We propose an extension of the linear global climate feedback framework to a regional feedbacks perspective, wherein any local TOA radiative response to forcing is assumed to be linearly related to the local surface temperature anomaly $T(\boldsymbol{r}, t)$ through a local climate feedback parameter $\lambda(\boldsymbol{r})$, where $\boldsymbol{r} = (\theta, \phi) =$ (latitude, longitude). Note that local feedbacks $\lambda(\boldsymbol{r})$ are assumed here to be time-invariant quantities that vary geographically due to differences in regional climate properties. Climate change at the regional scale is then described in terms of a local energy balance:

$$H(\boldsymbol{r}, t) = \lambda(\boldsymbol{r})T(\boldsymbol{r}, t) + R(\boldsymbol{r}, t) + \nabla \cdot \boldsymbol{F}(\boldsymbol{r}, t), \tag{5.4}$$

where $\nabla \cdot \boldsymbol{F}$ represents the change in horizontal convergence/divergence of energy due to changes in the combined oceanic and atmospheric heat transport $\boldsymbol{F}$; R is the local radiative forcing; and H is the local energy imbalance, equal to the rate of local heat content change.

The global mean of any quantity $Q(\boldsymbol{r}, t)$ is given by

$$\overline{Q} = \frac{1}{4\pi} \int_0^{2\pi} \int_{-\pi/2}^{\pi/2} Q(\theta, \phi, t) \cos\theta d\theta d\phi, \tag{5.5}$$

and we note that $\overline{\nabla \cdot \boldsymbol{F}} = 0$. Taking the global mean of Eq. (5.4) recovers the global energy balance described by Eq. (5.2):

$$\begin{aligned} \overline{H}(t) &= \overline{\lambda(\boldsymbol{r})T(\boldsymbol{r},t)} + \overline{R}(t) \\ &= \lambda_{eff}(t)\overline{T}(t) + \overline{R}(t), \end{aligned} \tag{5.6}$$

where we have identified

$$\lambda_{eff}(t) = \overline{\lambda(\boldsymbol{r}) \cdot \frac{T(\boldsymbol{r},t)}{\overline{T}(t)}}. \tag{5.7}$$

Equation (5.6) reproduces the traditional measure of λ_{eff}, from which the apparent time-dependence of effective climate feedback has been diagnosed in CCSM4 and other models.

Equation (5.7) represents an alternative measure of λ_{eff} that makes a direct connection to the spatial pattern of climate warming $T(\boldsymbol{r},t)/\overline{T}(t)$ and the strength of regional climate feedbacks $\lambda(\boldsymbol{r})$. It provides a physical interpretation of effective climate feedback and a mechanism for its time-variation: λ_{eff} is determined by the geographic pattern of surface temperature change through the activation of local climate feedbacks, and its time-dependence emerges naturally as the pattern of surface temperature evolves. The sign of each of the terms is such that low values of T_{eff} arise when regions of more positive (destabilizing) feedbacks experience little warming relative to the global mean (i.e., $T/\overline{T}$ is small locally), and when regions of more negative (stabilizing) feedbacks experience enhanced warming relative to the global mean (i.e., $T/\overline{T}$ is large locally).

5.4.1 Effective climate sensitivity in CCSM4

Does the regional feedbacks framework explain the time-dependence of T_{eff} found in CCSM4? The term $T(\boldsymbol{r},t)/\overline{T}(t)$ in Eq. (5.7) is a measure of the pattern of regional warming, normalized by the global mean warming at any given time. It contains the full time-dependence of T_{eff}, under the approximation that each $\lambda(\boldsymbol{r})$ is a time-invariant coefficient relating local surface temperature anomaly to TOA radiative response. We calculate $T(\boldsymbol{r},t)/\overline{T}(t)$ directly from the abrupt CO_2 doubling simulation.

The term $\lambda(\boldsymbol{r})$ in Eq. (5.7) is a measure of the local TOA radiative response per degree local surface temperature change. We estimate its value from feedbacks calculated using the radiative kernel method [75, 76, 78] by Bitz *et al.* [147] from the slab ocean version

of CCSM4 forced by a CO_2 doubling. Following convention, Bitz *et al.* [147] calculate regional feedbacks in terms of the local TOA radiative response per degree global surface temperature change, which we denote $\lambda^g(\boldsymbol{r})$. The relationship between local-temperature and global-temperature regional feedback definitions is

$$\lambda(\boldsymbol{r}) = \lambda^g(\boldsymbol{r}) \cdot \frac{T_{2\times}}{T(\boldsymbol{r})_{2\times}}, \tag{5.8}$$

where $T_{2\times}$ and $T(\boldsymbol{r})_{2\times}$ are the respective global and regional equilibrium temperature response of the SOM under CO_2 doubling. As mentioned above, we use the net global radiative feedback calculated from the SOM to estimate the tropospheric-adjusted radiative forcing within CCSM4 as $R_{2\times} = -\overline{\lambda^g(\boldsymbol{r})}T_{2\times} \approx 3$ Wm^{-2}, which is in good agreement with the adjusted forcing estimated by other methods (see Webb *et al.* [158], and references therein).

Together, $T(\boldsymbol{r},t)/\overline{T}(t)$ and $\lambda(\boldsymbol{r})$ allow an estimate of effective climate sensitivity through Eqs. (5.7) and (5.3), shown by the black line in Fig. 5.1b. The good agreement between T_{eff} calculated by regional feedbacks (black line) and diagnosed by global energy balance (blue line) in CCSM4 is taken as strong evidence that the magnitude and temporal characteristics of T_{eff} can be explained simply in terms of regional climate feedbacks and spatial patterns of warming.

The comparison of regional feedbacks and global energy balance approaches (Fig. 5.1b) may also be viewed as a test of the fundamental assumptions we have made regarding regional feedbacks in *Section 5.4*. We have defined local feedbacks $\lambda(\boldsymbol{r})$ in terms of local surface temperature change, and have thus neglected: (i) non-local contributions to climate feedbacks (e.g., non-local influences on cloud or lapse rate changes under transient warming); (ii) nonlinear contributions to local feedbacks that may arise due to higher order temperature dependencies; and (iii) any time-dependence of local feedbacks that may arise as local climates evolve. We have made the further approximation that feedbacks calculated from the SOM using linear radiative kernel feedback decomposition may be applied linearly to estimate local feedbacks within CCSM4 under transient warming, thus neglecting any correlations between feedbacks (e.g., due to the relationship between sea ice and the overlying lapse rate or cloud cover) and other radiative elements not included in the feedback decomposition. That T_{eff} calculated by regional feedbacks agrees well with T_{eff} diagnosed

by global energy balance (Fig. 5.1b) suggests that these assumptions and approximations are reasonable for the purposes of calculating T_{eff} over the range of climate states considered here.

The above results show that, to a good approximation, effective climate feedback λ_{eff} and climate sensitivity T_{eff} within CCSM4 may be explained simply in terms of the geographic pattern of surface temperature at any given time ($T(\boldsymbol{r},t)/\overline{T}(t)$) through the activation of local, time-invariant climate feedbacks ($\lambda(\boldsymbol{r})$) as described by Eq. (5.7). This suggests that climate feedbacks can be naturally defined with respect to local surface temperature anomalies; climate feedbacks defined in the conventional way (with respect to the global surface temperature anomaly) must inherently vary in magnitude as geographic patterns of surface temperature evolve.

Geographic patterns of warming and feedbacks

In the above section we verified that the effective climate sensitivity could be calculated accurately through Eq. (5.7). We next examine the mechanisms of T_{eff} variation within CCSM4 by considering the two terms, $T(\boldsymbol{r},t)/\overline{T}(t)$ and $\lambda(\boldsymbol{r})$, separately and in combination within three distinct periods following CO_2 doubling: the first decade, when T_{eff} is relatively large; years 20–60 when T_{eff} is near its minimum value; and years 200–300 as T_{eff} when increasing slowly toward $T_{2\times}$ (Fig. 5.1b). For reference, we also show these terms within the slab ocean version of the model from which $T_{2\times}$ and the regional climate feedbacks have been calculated.

Figure 5.2 shows the evolving pattern of surface warming (the change in local temperature normalized by the change in global temperature, $\Delta T(\boldsymbol{r})/\Delta\overline{T}$) between each of the above periods. Several distinct timescales and patterns of climate response to forcing can be identified that are broadly consistent with those found within other GCM simulations of transient climate warming [57, 115, 160]. Following CO_2 doubling: (i) Within several years, temperatures adjust throughout the atmosphere and over land and sea ice (Fig. 5.2a) due to the relatively small heat capacities of these climate components; (ii) Over the following decades, warming is characterized by a more globally uniform pattern, with substantial

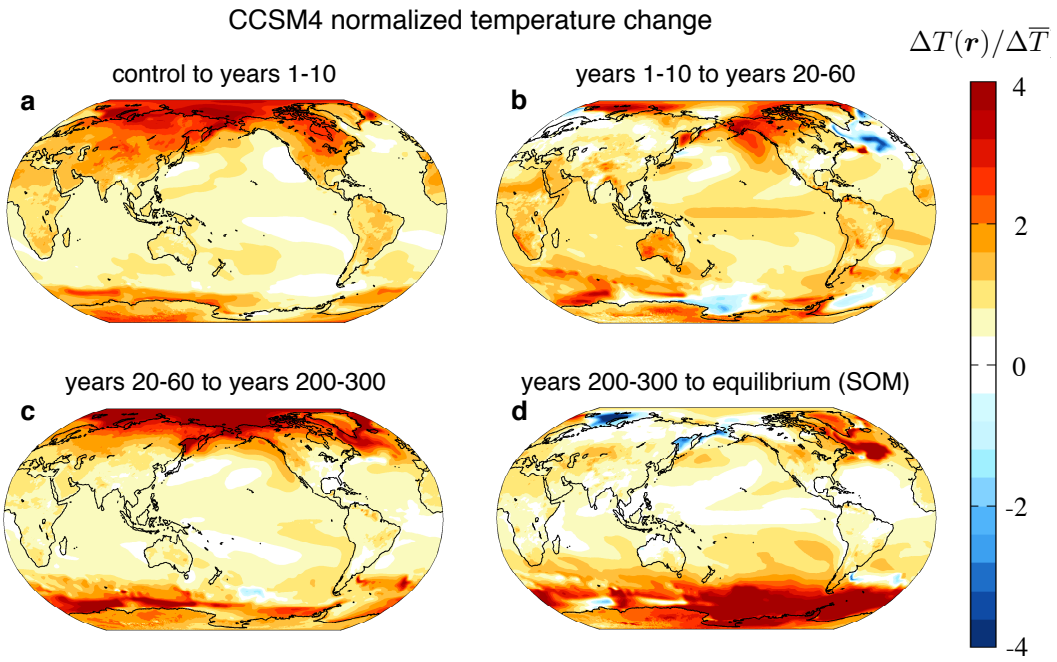

Figure 5.2: Spatial patterns of surface warming within CCSM4. Regional temperature change normalized by global mean temperature change between the periods **a,** 'control' to years 1-10, **b,** years 1-10 to 20-60, **c,** years 20-60 to 200-300, and **d,** years 200-300 to equilibrium (as estimated by the SOM).

warming of the tropical oceans (Fig. 5.2b). On these decadal timescales, ocean circulation changes play an important role in setting regional temperature trends (e.g., reduced meridional ocean heat transport contributes to local surface cooling in the North Atlantic Ocean; reduced convection in some regions of the Southern Ocean leads to local surface cooling due to reduced upward isopycnal mixing of heat into the ocean mixed layer [136, 161]; and increased ocean heat transport into the Arctic Ocean enhances sea ice loss and local surface warming [110]); (iii) Over the following centuries, a pattern of polar-amplified warming emerges in both hemispheres (Figs. 5.2c,d) as global climate slowly attains equilibrium with the imposed forcing [115, 160, 162]. Fig. 5.3a shows zonal means of $T/\overline{T}$ for each of the above periods.

Figure 5.4 displays the net regional feedback $\lambda(\boldsymbol{r})$ within CCSM4, defined in terms of local temperature change, and Fig. 5.3b shows zonal means of the net and individual

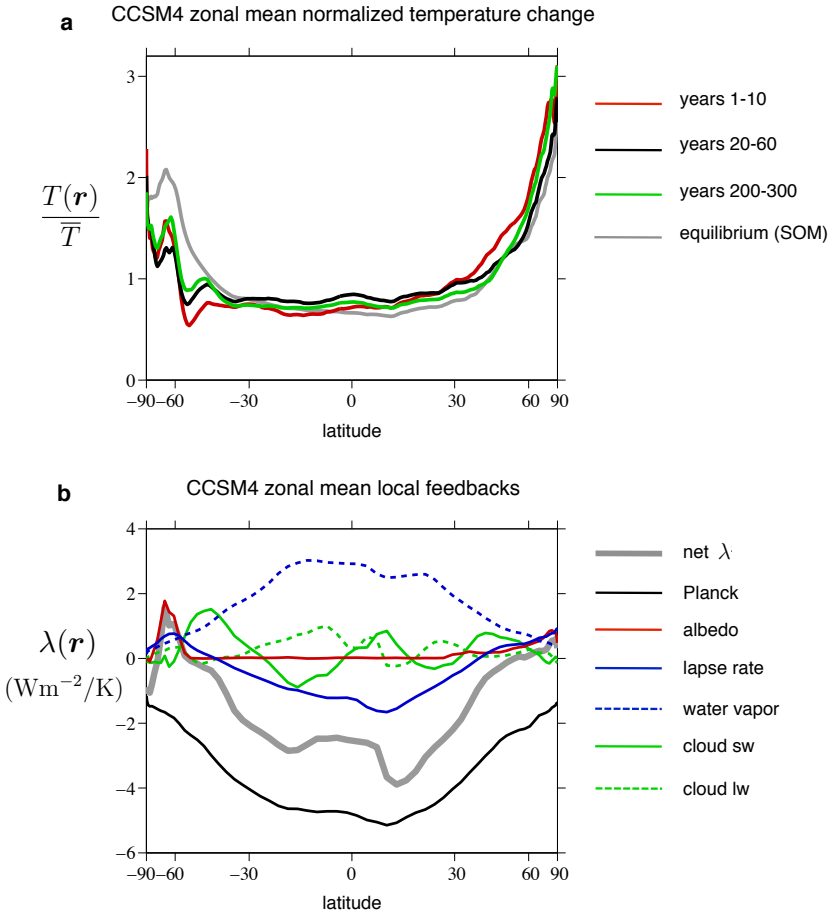

Figure 5.3: Zonal mean surface warming and local feedbacks within CCSM4. a, Regional temperatures normalized by global mean temperature, and **b,** Net local feedback (grey) as in Fig. 5.4, but zonal mean. Zonal means of individual local climate feedbacks, as in Fig. 5.8, are also shown. The individual feedbacks everywhere sum to the net feedback $\lambda(\boldsymbol{r})$.

feedbacks (see Fig. 5.8 in the appendix for spatial maps of individual feedbacks within CCSM4). The net feedback is generally strongly negative (stabilizing) in the low- to mid-latitudes (particularly over the oceans), owing to locally large and negative Planck and lapse rate feedbacks. Net feedback becomes less negative (less stabilizing) toward high-latitudes, due mainly to less-negative Planck and lapse rate feedbacks (though this trend is partially offset by a less-positive water vapor feedback at high-latitudes). In the Arctic and Southern Oceans, feedbacks become locally positive owing to local maxima in surface albedo and lapse rate feedbacks. Net feedback is generally less negative over land, compared to the

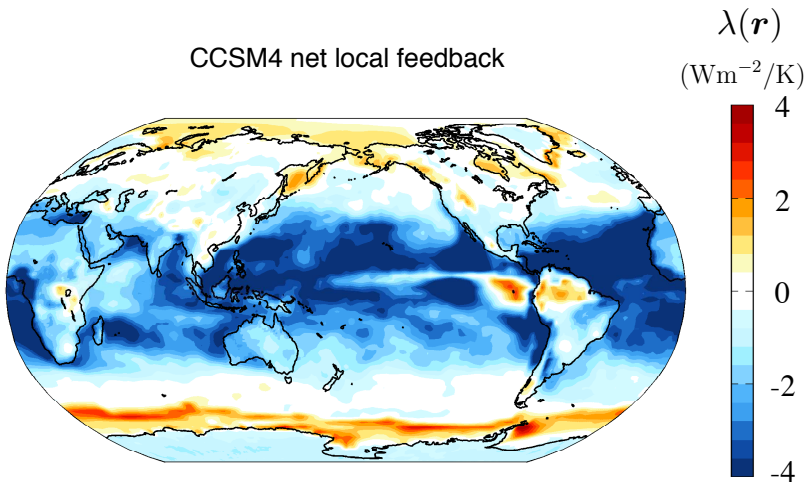

Figure 5.4: Spatial pattern of net local feedback within CCSM4. Net local feedback $\lambda(\boldsymbol{r})$ (TOA response per degree local surface temperature change) estimated by radiative kernels.

oceans, due to (i) reduced Planck and lapse rate feedbacks over land at any given latitude and (ii) positive snow albedo feedbacks, particularly in the northern hemisphere.

A qualitative description of the time-variation of effective climate sensitivity (Fig. 5.1b) is thus readily available. Following CO_2 doubling, abrupt warming over land and sea ice, in the presence of more-positive-than-average regional climate feedbacks, leads to an initially high value of T_{eff}. Over the following decades the tropical oceans warm, activating large and stabilizing tropical feedbacks and reducing T_{eff}. Finally, over the following centuries the slow emergence of polar-amplified warming in the presence of less-negative (or even locally positive) high-latitude feedbacks pushes T_{eff} toward the equilibrium climate sensitivity $T_{2\times}$.

The quantity $[\lambda(\boldsymbol{r}) \cdot T(\boldsymbol{r},t)/\overline{T}(t) - \lambda^g(\boldsymbol{r})]$ is a quantitative measure of the difference between effective regional climate feedbacks (TOA response per degree global warming) calculated within transient (CCSM4) and equilibrium (SOM) simulations; the global mean of this quantity at any given time is equal to $\lambda_{eff} - \overline{\lambda^g}$, the difference between transient and SOM estimated effective global climate feedback parameters. The zonal mean of this quantity for the three distinct time periods considered here (Fig. 5.5) shows that delayed surface warming within the Southern Ocean results in a substantially reduced effective

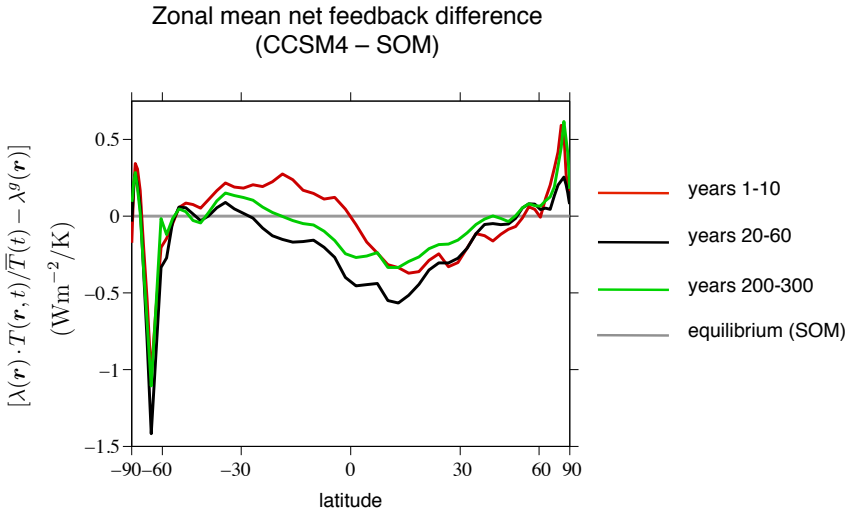

Figure 5.5: Zonal effective climate feedback difference between transient and equilibrium. Net zonal climate feedback (TOA response per degree global surface temperature change) for the three distinct periods following an instantaneous CO_2 doubling, subtracted from the net climate zonal feedback estimated from the SOM simulation. The area-weighted global mean of each curve is equal to $\lambda_{eff} - \overline{\lambda^g}$, the difference between transient and SOM estimated global climate feedback parameters.

local feedbacks under transient warming compared to effective feedbacks estimated within the SOM. Similarly, enhanced surface warming in the tropics results in substantially more negative tropical effective feedbacks and enhanced warming in the Arctic (due to changes in ocean circulation not accounted for in the SOM) leads to more positive Arctic effective feedbacks under transient warming. Thus, T_{eff} is less than $T_{2\times}$ under transient warming due primarily to relatively larger warming in low-latitude regions compared to equilibrium, in the presence of large negative local feedbacks, and secondarily to relatively smaller warming in mid-to-high latitudes compared to equilibrium (particularly in the southern hemisphere), in the presence of less-negative local feedbacks.

5.4.2 Effective climate sensitivity in a low-order energy balance climate model

We have demonstrated the utility of the regional climate feedbacks approach for calculating T_{eff} and identifying the mechanisms of its time-variation within the context of a fully-coupled general circulation model. Here we make use of a low-order model of global climate change, designed to provide a parsimonious demonstration of time-varying T_{eff}

from regional climate feedbacks.

Consider a simple model of climate change wherein Earth is represented by three regions of equal area that can each be described by a local energy balance (Eq. (5.4)):

$$\begin{aligned} c_{\text{land}}\frac{dT_{\text{land}}}{dt} &= H_{\text{land}} = \lambda_{\text{land}}T_{\text{land}} + R, \\ c_{\text{low}}\frac{dT_{\text{low}}}{dt} &= H_{\text{low}} = \lambda_{\text{low}}T_{\text{low}} + R, \\ c_{\text{high}}\frac{dT_{\text{high}}}{dt} &= H_{\text{high}} = \lambda_{\text{high}}T_{\text{high}} + R. \end{aligned} \tag{5.9}$$

For simplicity, each region is characterized by a constant heat capacity c_i and forced by the same radiative forcing R, and changes in heat transport between regions has been neglected. This model is of similar form to that used previously to study the effect of multiple climate regimes, with distinct radiative properties, on the global equilibrium climate sensitivity [163, 164].

We associate the regions 'land', 'low', and 'high' with land, low-latitude oceans, and high-latitude oceans, respectively, and choose regional properties of each to broadly mimic the three distinct timescales and patterns of climate response to forcing found within GCMs as described above: $c_{\text{land}} << c_{\text{low}} < c_{\text{high}}$. We further constrain the equilibrium warming in each region and the global equilibrium climate sensitivity $T_{2\times}$ to be similar to the respective quantities in CCSM4: $|\lambda_{\text{high}}| < |\lambda_{\text{land}}| < |\lambda_{\text{low}}|$, and $T_{2\times} = 1/3(-R_{2\times}/\lambda_{\text{land}} - R_{2\times}/\lambda_{\text{low}} - R_{2\times}/\lambda_{\text{high}}) \approx 3.2\,^{\circ}\text{C}$ for $R_{2\times} = 3\ \text{Wm}^{-2}$.

Figure 5.6 shows the response of this model (Eqs. (5.9)) to an instantaneous doubling of CO_2 in year zero. Effective climate sensitivity $T_{eff} = -R_{2\times}/\lambda_{eff}$ can be calculated by either global energy balance (Eq. (5.2)) or, equivalently, by regional feedbacks (Eq. (5.7)):

$$\lambda_{eff} = 1/3(\lambda_{\text{land}}\frac{T_{\text{land}}}{\overline{T}} + \lambda_{\text{low}}\frac{T_{\text{low}}}{\overline{T}} + \lambda_{\text{high}}\frac{T_{\text{high}}}{\overline{T}}), \tag{5.10}$$

where the time-evolution of temperature in each region is shown in Fig. 5.6c.

The details of T_{eff} (Fig. 5.6b) are sensitive to the model and parameter choices we have made. However, time-dependence of T_{eff} is a robust result that arises naturally from only an evolving geographic pattern of warming (Figs. 5.6a,c) in conjunction with a spatial pattern of regional feedbacks. By resolving three distinct timescales and patterns of climate

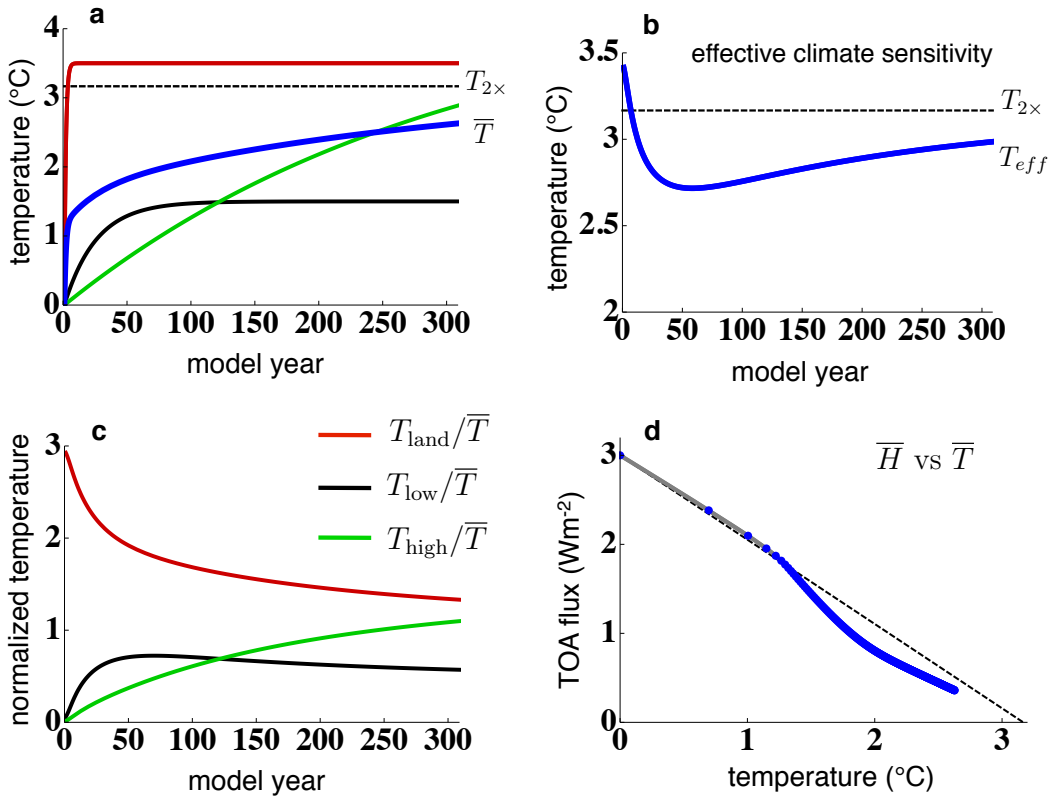

Figure 5.6: Temperature and effective climate sensitivity in a low-order climate model. **a,** Global mean (blue), land (red), low-latitude ocean (black) and high-latitude ocean (green) surface temperatures following an abrupt doubling of CO_2 in year zero, **b,** effective climate sensitivity, **c,** regional temperatures normalized by global mean temperature, and **d,** global annual TOA energy flux plotted against global annual mean temperature.

response (broadly representing the fast response of land, the decadal response of the low-latitude oceans and the centennial response of the high-latitudes oceans) and a geographic pattern of feedbacks (broadly representing large and negative local feedbacks over low-latitude oceans, and less-negative local feedbacks over land and high-latitude oceans) this simple energy balance model is able to qualitatively reproduce the time-dependence of T_{eff} within CCSM4 and other GCMs.

Finally, Fig. 5.6d shows the global TOA flux $\overline{H}$ plotted against global surface temperature $\overline{T}$ over the simulation. The nonlinearity in the relationship between $\overline{H}$ and $\overline{T}$ (under constant $\overline{R} = R_{2\times}$) follows from the time-variation of λ_{eff} in Eq. (5.2) arising from regional

climate feedbacks; if regional feedbacks were uniform everywhere ($\lambda(\boldsymbol{r}) = \lambda_{eq}$) then λ_{eff} would be constant in time and the trajectory of points would follow the dashed line, with slope $1/\lambda_{eq} = -R_{2\times}/T_{2\times}$. From Eq. (5.6) the instantaneous slope of the regression of $\overline{H}$ vs $\overline{T}$ is given by

$$\begin{aligned} \frac{d\overline{H}}{d\overline{T}} &= \frac{d}{d\overline{T}} \overline{\lambda(\boldsymbol{r})T(\boldsymbol{r},t)} \\ &= 1/3(\lambda_{\text{land}} \frac{dT_{\text{land}}}{d\overline{T}} + \lambda_{\text{low}} \frac{dT_{\text{low}}}{d\overline{T}} + \lambda_{\text{high}} \frac{dT_{\text{high}}}{d\overline{T}}), \end{aligned} \tag{5.11}$$

In this simple model, where changes in heat transport between regions has been neglected, only the 'high-latitude ocean' region is still warming substantially beyond a few centuries, at which point $d\overline{H}/d\overline{T} \approx \lambda_{\text{high}}$. In this regime, the $\overline{H}$–$\overline{T}$ regression line in Fig. 5.6d may be extrapolated (with slope λ_{high}) to the point $[\overline{T} = T_{2\times}, \overline{H} = 0]$ to estimate $T_{2\times}$ even before the global equilibrium has been reached. In the following section we discuss the implications of this simple model result for the calculation of climate feedbacks with regression methods within GCMs.

5.5 Discussion

Our central finding is that the effective global climate feedback λ_{eff} is fundamentally linked to the geographic pattern of (approximately time-invariant) regional climate feedbacks and the pattern of surface warming at any given time. Time-variation of global climate feedback, and the corresponding effective climate sensitivity T_{eff}, arises naturally when the pattern of surface warming evolves over time, activating regional feedbacks of different strengths. Within a fully-coupled general circulation model (CCSM4) the geographic pattern of warming, together with an estimate of the magnitude of regional climate feedbacks, allows a calculation of T_{eff} that agrees well with that diagnosed from global energy balance over the course of an abrupt CO_2 doubling simulation. Effective climate sensitivity is found to be lower than the equilibrium climate sensitivity $T_{2\times}$ under transient warming: on decadal timescales, warming of the low-latitude oceans activates strongly negative (stabilizing) regional feedbacks, leading to a low value of T_{eff}; on centennial and longer timescales, a pattern of polar amplified warming emerges, activating less-negative and even positive (destabilizing) high-latitude feedbacks, pushing T_{eff} toward higher values until

global climate equilibrium is attained.

A low-order energy balance climate model, broadly representing three distinct climate regimes and associated timescales of climate response, is able to qualitatively reproduce the time-variation of T_{eff} found within CCSM4. This model is employed here mainly as a demonstration of the robustness of the above results: while the details T_{eff} depend sensitively on the atmospheric and oceanic physics that gives rise to particular geographic patterns of feedbacks and surface temperature change, the general principle that T_{eff} must vary under transient warming is an inevitable consequence of regionally-varying climate feedbacks. Time-varying T_{eff} is thus expected within all models of climate change that represent distinct feedbacks and climate response times within two or more regions. Moreover, T_{eff} can be expected to vary in the observed climate system as the spatial pattern of surface temperature evolves over time.

5.5.1 Connection to previous studies

Our physical interpretation of T_{eff} and proposed mechanism of its time-variation can be compared to those of previous studies. Senior and Mitchell [148] highlight time-dependent cloud feedbacks, arising from interhemispheric warming differences associated with the slow response of the Southern Ocean, as a chief cause of time-dependence in T_{eff}. The slow emergence of high-latitude warming (Fig. 5.2), particularly in the southern hemisphere, plays a central role in the delayed activation of high-latitude feedbacks within CCSM4. However, our results suggest that all feedbacks together contribute to T_{eff} through the net feedback $\lambda(\boldsymbol{r})$ in Eq. (5.7), and that it is those individual feedbacks with the greatest meridional structure that contribute most to the time-variation of T_{eff} as the polar-amplified warming pattern emerges. An analysis of individual climate feedbacks in CCSM4 (Figs. 5.3 and 5.8) shows less-negative Planck and lapse rate feedbacks in high-latitudes to be the chief contributors to the meridional structure in net feedback, with surface albedo contributing locally in the Arctic and Southern Oceans and with water vapor feedback opposing the net feedback meridional structure. Clouds, having little meridional structure in CCSM4 (Fig. 5.3), play a relatively small role in the time-variation of T_{eff}.

Williams *et al.* [152] argue that the time-dependence of T_{eff} can be attributed to an 'effective forcing' R_{eff} that takes into account non-feedback cloud adjustments on timescales far more rapid than that of global surface warming [152, 154–158], and is thus distinct from the traditional measure of radiative forcing $R_{2\times}$ that does not account for tropospheric adjustment. The basic reasoning is that a misdiagnosis of radiative forcing can lead to an apparent time-dependence in λ_{eff} in Eq. (5.2). Using the method of Gregory *et al.* [150], Williams *et al.* [152] perform regression of $\overline{H}$ vs $\overline{T}$ in a range of GCMs under a CO_2 doubling, and note a generally strong linearity as equilibrium is approached (Fig. 5.7). They propose that the slope of this regression gives an estimate of the equilibrium climate feedback parameter, provided that we interpret the intercept of this line with the $\overline{H}$ axis as a measure of the effective forcing R_{eff} and the intercept with the $\overline{T}$ axis as a measure of the equilibrium climate sensitivity $T_{2\times}$ (solid line through points in Fig. 5.7).

If, following Winton *et al.* [137], we define the time-dependent parameter

$$\varepsilon = \overline{R}/R_{eff}, \tag{5.12}$$

then the climate feedback parameter estimated from the $\overline{H}$–$\overline{T}$ regression is equal to λ_{eq}/ε, which is distinct from λ_{eff} as diagnosed from Eq. (5.2) for all nonunitary values of ε (see Fig. 5.7). Williams *et al.* [152] suggest that an apparent time-dependence of T_{eff} can arise when climate evolves along lines of constant ε in $\overline{H}$–$\overline{T}$ space, and that this time-dependence can be largely eliminated by identifying the effective radiative forcing R_{eff} and interpreting the slope of the regression line as the equilibrium climate feedback parameter [152].

The above regression method has been widely used to simultaneously estimate the tropospheric-adjusted radiative forcing and climate feedbacks in models [152, 154, 155, 157, 158, 165–167] and observations [168, 169]. However, fully-coupled GCM simulations (e.g., Fig. 5.7) show that ε varies over decades to centuries, instead of days to weeks as expected from the timescale of tropospheric adjustment, strongly suggesting an explanation for T_{eff} involving slowly evolving spatial warming patterns that occur on decadal and longer timescales [137, 147]. Moreover, in our analysis we have accounted for fast tropospheric forcing adjustments in our value of $R_{2\times}$, and thus we interpret any apparent values of $R_{eff} < R_{2\times}$ in Fig. 5.7 as a consequence of regional climate feedbacks: from Eq. (5.6),

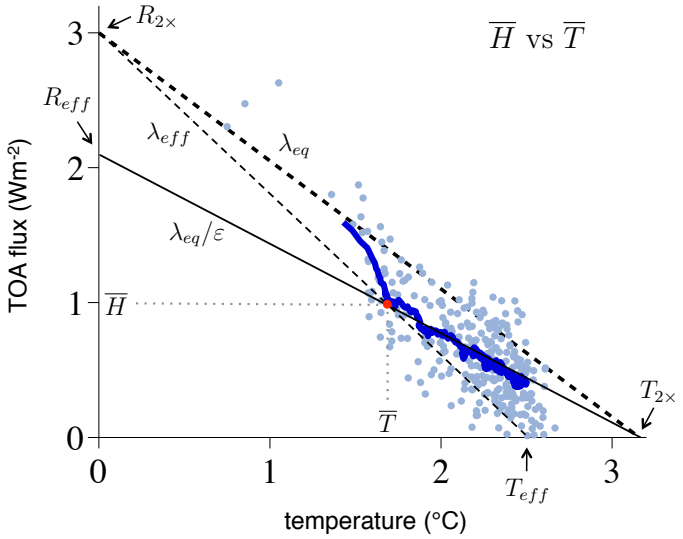

Figure 5.7: TOA energy flux plotted against global mean temperature. Light blue dots show individual years, and dark blue dots show the 10-year running mean from the CCSM4 CO_2 doubling simulation. The red dot indicates a particular decade with global energy imbalance equal to $\overline{H}$ and global mean temperature equal to $\overline{T}$. T_{eff} at this time can be schematically represented as the extrapolation of a line (with slope λ_{eff}) from point [0,$R_{2\times}$] through this dot to [T_{eff},0]. Alternatively, R_{eff} can be determined by extrapolating a line (with slope λ_{eq}/ε) from point [$T_{2\times}$,0] through this point to [0,R_{eff}]. The dashed line (with slope λ_{eq}) connecting points [0,$R_{2\times}$] and [$T_{2\times}$,0] is the expected trajectory of points under the assumption that effective climate feedback is constant in time.

the slope of the $\overline{H}$–$\overline{T}$ regression is an approximation of the instantaneous slope

$$\begin{aligned}\frac{d\overline{H}}{d\overline{T}} &= \frac{d}{d\overline{T}}\overline{\lambda(\boldsymbol{r})T(\boldsymbol{r},t)}, \\ &= \overline{\lambda(\boldsymbol{r})\cdot\frac{dT}{d\overline{T}}},\end{aligned} \tag{5.13}$$

and is thus a measure of the strength of regional feedbacks weighted by the rate of local temperature change with global temperature change. The $\overline{H}$–$\overline{T}$ regression slope estimated from late in CO_2 doubling simulations (Fig. 5.7) is thus a measure of the strength of feedbacks in those regions where surface temperatures are changing most rapidly, namely the high-latitude oceans (Figs. 5.2c,d). Therefore, the $\overline{H}$–$\overline{T}$ regression method does not in general provide an accurate estimate of the global climate feedback λ_{eq}, and instead may greatly overestimate its value, consistent with an underestimation of radiative forcing $R_{eff} < R_{2\times}$.

The results of the simple three-region energy balance model (Fig. 5.6d), wherein forcing and feedbacks are specified explicitly, are consistent with these arguments.

We reemphasize here that since some amount of fast tropospheric adjustment to CO_2 occurs before global surface temperature evolves [85,157,158,170], the tropospheric-adjusted forcing is still important for the estimation of T_{eff} (through the value of forcing in Eqs. (5.2) and (5.3)). The full time-dependence of T_{eff} is thus influenced by both fast tropospheric adjustments to forcing and the slow evolution of the spatial pattern of surface warming, and both effects must be accounted for. By using an estimate of the tropospheric-adjusted CO_2 forcing in our analysis, we focus here on only the latter mechanism.

Winton *et al.* [137] propose an alternative interpretation of T_{eff} and R_{eff} in terms of a time-dependent 'efficacy of ocean heat uptake' that arises due to its geographic structure, analogous to the distinct efficacies of different radiative forcing agents [85–87]. In this view, global ocean heat uptake can be thought of as an effective forcing on the surface components of the climate system (with possibly nonunitary efficacy), such that global surface temperature evolves according to a mixture of radiative forcing and heat exchange with the deep ocean. An alternative form of global energy balance (Eq. (5.2)) can be defined that takes into account ocean heat uptake efficacy ε [137]:

$$\varepsilon(t)\overline{H}(t) = \lambda_{eq}\overline{T}(t) + \overline{R}(t). \tag{5.14}$$

Note that the same parameter ε is used to define both "effective forcing" and "ocean heat uptake efficacy" since the two approaches are mathematically equivalent [137] (this can be seen by dividing both sides of Eq. (5.14) by ε and using Eq. (5.12) to eliminate $\overline{R}$). From Eqs. (5.2) and (5.14), the relationship between efficacy and λ_{eff} at any given time is

$$\lambda_{eff}(t)\overline{T}(t) = \lambda_{eq}\overline{T}(t) - (\varepsilon(t) - 1)\overline{H}(t). \tag{5.15}$$

Thus, an ocean heat uptake efficacy $\varepsilon > 1$ directly corresponds to an effective global climate feedback λ_{eff} that is more negative than the equilibrium global climate feedback λ_{eq}, resulting in $T_{eff} < T_{2\times}$ under transient warming. If the value of ε is approximately constant (and greater than one) over some period of time, the $\overline{H}$–$\overline{T}$ regression is characterized by slope λ_{eq}/ε (Fig. 5.7), and is thus a measure of the equilibrium climate feedback parameter scaled by the ocean heat uptake efficacy ε.

In the Winton *et al.* [137] interpretation, time-varying λ_{eff} is driven by nonunitary efficacy ε. From the regional feedbacks perspective, the nonlinear relationship between $\overline{H}$ and $\overline{T}$, and thus nonunitary ε, is naturally described in terms of the effective climate feedback λ_{eff}. In turn, λ_{eff} is driven by the geographic patterns of $\lambda(\boldsymbol{r})$, ocean heat uptake, atmospheric and oceanic heat transports, and radiative forcing through their respective influences on the geographic pattern of surface temperature at any given time (Eq. (5.4)).

The strong connection between efficacy ε and regional climate feedbacks can be made more explicit. The global mean temperature $\overline{T} = \overline{H/\lambda} - \overline{(\nabla \cdot \boldsymbol{F})/\lambda} - \overline{R/\lambda}$ (from Eq. (5.4)), together with Eq. (5.14), gives an expression for efficacy in terms of regional properties:

$$\varepsilon(t) = \underbrace{\frac{\overline{H(\boldsymbol{r},t)/\lambda(\boldsymbol{r})}}{\overline{H}(t)/\lambda_{eq}}}_{\text{(i)}} - \underbrace{\frac{\overline{\nabla \cdot \boldsymbol{F}(\boldsymbol{r},t)/\lambda(\boldsymbol{r})}}{\overline{H}(t)/\lambda_{eq}}}_{\text{(ii)}} - \underbrace{\frac{\overline{R(\boldsymbol{r},t)/\lambda(\boldsymbol{r})} - \overline{R}(t)/\lambda_{eq}}{\overline{H}(t)/\lambda_{eq}}}_{\text{(iii)}} . \tag{5.16}$$

Over long timescales and over the ocean, the rate of local heat content change, $H(\boldsymbol{r},t)$, is approximately equal to the rate of local ocean heat uptake, and thus term (i) can be interpreted as the contribution to ε arising from a geographic pattern of ocean heat uptake acting on a geographic pattern of regional feedbacks $\lambda(\boldsymbol{r})$—a given global heat uptake $\overline{H}$ may drive a different global surface temperature response depending on its geographic structure. Ocean heat uptake occurring preferentially in regions of less-negative local feedbacks, such as the Southern Ocean, drives ε toward values greater than one, and slow variations in the geographic pattern of heat uptake drive changes in ε over decades to centuries (Fig. 5.7) [137, 147]. Note that in the limit of spatially uniform feedbacks ($\lambda(\boldsymbol{r}) = \lambda_{eq}$ in all regions), term (i) approaches unity.

Term (ii) in Eq. (5.16) can be interpreted as the contribution to ε arising from changes in the dynamical transport of energy between regions of different local feedback strengths, and can thus be described as an 'efficacy of heat transport'. The convergence of energy preferentially out of regions of more-negative feedbacks and into regions of less-negative local feedbacks drives ε toward a higher value. In the limit of spatially uniform $\lambda(\boldsymbol{r})$, term (ii) approaches zero.

Term (iii) in Eq. (5.16) can be interpreted as the contribution to ε arising from a geographic pattern of radiative forcing $R(\boldsymbol{r},t)$ acting on a geographic pattern of regional

feedbacks $\lambda(\boldsymbol{r})$. This term has a direct connection to the traditional concept of 'efficacy of climate forcing', wherein different radiative forcing agents have been found to drive a different global temperature response (per unit global radiative forcing) depending on their distinct geographic forcing structures [85–87]. In particular, ε is driven toward a higher value when relatively stronger forcing occurs preferentially in regions of less-negative local feedbacks. In the limit of spatially uniform $\lambda(\boldsymbol{r})$, term (iii) approaches zero.

Equation (5.16) shows that efficacy ε is inherently linked to the pattern of regional feedbacks, and that a nonunitary value of ε follows directly from non-uniform $\lambda(\boldsymbol{r})$. However, ε, as defined by Winton *et al.* [137], is not driven solely by the structure of ocean heat uptake (term (i)), but depends also on changes in atmospheric and oceanic heat transports (term (ii)) and on the geographic pattern of radiative forcing (term (iii)). This is fundamentally a consequence of the assumption that λ_{eff} can be described entirely by a time-varying efficacy related to ocean heat uptake (Eq. (5.15)): the geographic patterns of heat transport anomalies and radiative forcing, which contribute to λ_{eff} through their effects on the spatial pattern of surface temperature (Eq. (5.7)), become conflated ε.

Ocean heat uptake efficacy thus provides a powerful interpretation of time-varying λ_{eff} when dynamic heat transport changes are small and radiative forcing is uniform. It may also be a useful description of λ_{eff} over the period of slow adjustment toward equilibrium with a fixed radiative forcing (beyond about a century into the CCSM4 simulation in Fig. 5.7), wherein a pattern of polar amplified warming emerges slowly (Fig. 5.2c), resulting in a constant $\overline{H}$–$\overline{T}$ slope (via Eq. (5.13)) and thus constant ε. This adjustment is driven primarily by a slow decrease in ocean heat uptake in high-latitudes [147], and thus time-varying λ_{eff} over this period may be interpreted through ocean heat uptake efficacy (term(i) in Eq. (5.16)). In light of the above arguments, we view the regional feedbacks perspective employed here as a more general description of λ_{eff} that is useful over all timescales, under a spatial pattern of radiative forcing, and under transient forcing scenarios where the spatial pattern of surface warming may vary considerably over decades. Regional feedbacks provide a framework with which to investigate the full time-evolution of ocean heat uptake efficacy, and its variation across climate models. In practice, λ_{eff} can be calculated by Eq. (5.7), and the value of efficacy ε can then be diagnosed by use of Eq. (5.15).

5.5.2 Implications for feedbacks and climate sensitivity in models and observations

We have found that the effective global climate feedback λ_{eff} inherently varies as the geographic pattern of surface warming (acting on constant local feedbacks) evolves. *Section 5.4.1* showed that the chief source of λ_{eff} variation in CCSM4 in the decades following an abrupt CO_2 doubling is a fast warming over land and sea ice, activating destabilizing feedbacks in those regions, followed by a slower warming of the low-latitude oceans, activating strongly stabilizing feedbacks. On centennial timescales, an activation of high-latitude feedbacks due to an emerging pattern of polar amplified warming slowly increased λ_{eff} toward its equilibrium value.

These results suggest that climate feedbacks, defined with respect to global surface temperature change, must in general be interpreted as 'effective' quantities that reflect the particular pattern of surface warming over which they are estimated. This result has several important implications for the estimation and interpretation of climate feedbacks and climate sensitivity. Within models, estimates of climate feedbacks based on transient warming scenarios (e.g., Soden and Held [75] and Zelinka and Hartmann [171]) can be expected to produce different spatial effective feedback patterns, and a different global effective feedback, than those estimates based on equilibrium scenarios (e.g., Bitz *et al.* [147]) (see Fig. 5.5). Defining local feedbacks with respect to local surface temperature change avoids this time-dependence, and thus provide a more consistent measure of the local radiative response to warming, at the expense of requiring the spatial pattern of surface warming to calculate the effective global feedback λ_{eff}.

Within observations, the time-variation of climate feedbacks greatly limits our ability to place constraints on the long-term evolution of global climate. Within CCSM4, $T_{eff} < T_{2\times}$ under transient warming, consistent with other fully-coupled GCMs [137, 152], raising the possibility of a substantially larger climate change commitment than that implied by the estimation of climate sensitivity from the modern climate state (e.g., *Chap. 4*). Moreover, accurate climate projection requires predicting how λ_{eff} will evolve over time.

The potential for different types of climate change to be governed by distinct effective climate feedbacks greatly complicates the comparison of climate change from different periods.

For instance, the climate response to abrupt forcing changes, such as volcanic eruptions, provides a measure of global feedback associated with a fast climate adjustment (i.e., feedbacks are activated over land and sea ice) and thus provides little information about how the global feedback may evolve over long timescales. In contrast, the climate response to very slow forcing changes, such as the orbital and greenhouse gas changes between the Last Glacial Maximum and present day, provides a near-equilibrium measure of global feedback ($\lambda_{eff} \approx \lambda_{eq}$). Bayesian approaches that combine multiple observations of climate change from different periods to derive narrower bounds on climate sensitivity (e.g., Annan and Hargreaves [172]) are predicated on the assumption that each estimate is providing information about the same global climate feedback, and thus are called into question by the finding that λ_{eff} depends fundamentally on the spatial warming pattern in each period.

Finally, *Section 5.5.1* showed that the regression of global TOA energy flux $\overline{H}$ onto global temperature $\overline{T}$, a method widely used to simultaneously estimate the equilibrium climate feedback parameter and 'effective' radiative forcing in models and observations [152,154,155,157,158,165–169], is better interpreted as a measure of local feedbacks weighted by the rate of local surface temperature change (Eq. (5.13)). Regression methods can thus be expected to provide an estimate of global feedback that is biased towards those regions that are changing most rapidly at the time the regression is performed.

5.5.3 Concluding remarks

We have shown here that the effective climate sensitivity is naturally described in terms of a spatial pattern of surface temperature acting on an approximately time-invariant pattern of regional feedbacks. As the geographic pattern of warming evolves, regional feedbacks of different strengths are activated, driving changes in the effective global radiative response to surface warming λ_{eff}, and thus time-dependence in the effective climate sensitivity T_{eff}.

Our focus has been on an idealized instantaneous CO_2 doubling scenario, which cleanly separates 'fast' and 'slow' timescales of climate response and facilitates identification of the mechanisms of λ_{eff} variation within CCSM4. In more realistic forcing scenarios, where climate forcing is ramped more slowly and a range of radiative forcing agents are included,

a different λ_{eff} is expected. The good agreement between λ_{eff} calculated by regional feedbacks and diagnosed by global energy balance suggests that the regional climate feedbacks framework is a powerful tool for calculating and understanding the time-variation of λ_{eff} under a range of forcing scenarios and models. Moreover, a redefinition of regional feedbacks in terms of local temperature change eliminates the influence of the spatial pattern of warming, and may thus permit insight into the sources of spread of future climate projections across climate models.

5.6 Appendix: spatial distribution of individual climate feedbacks within CCSM4

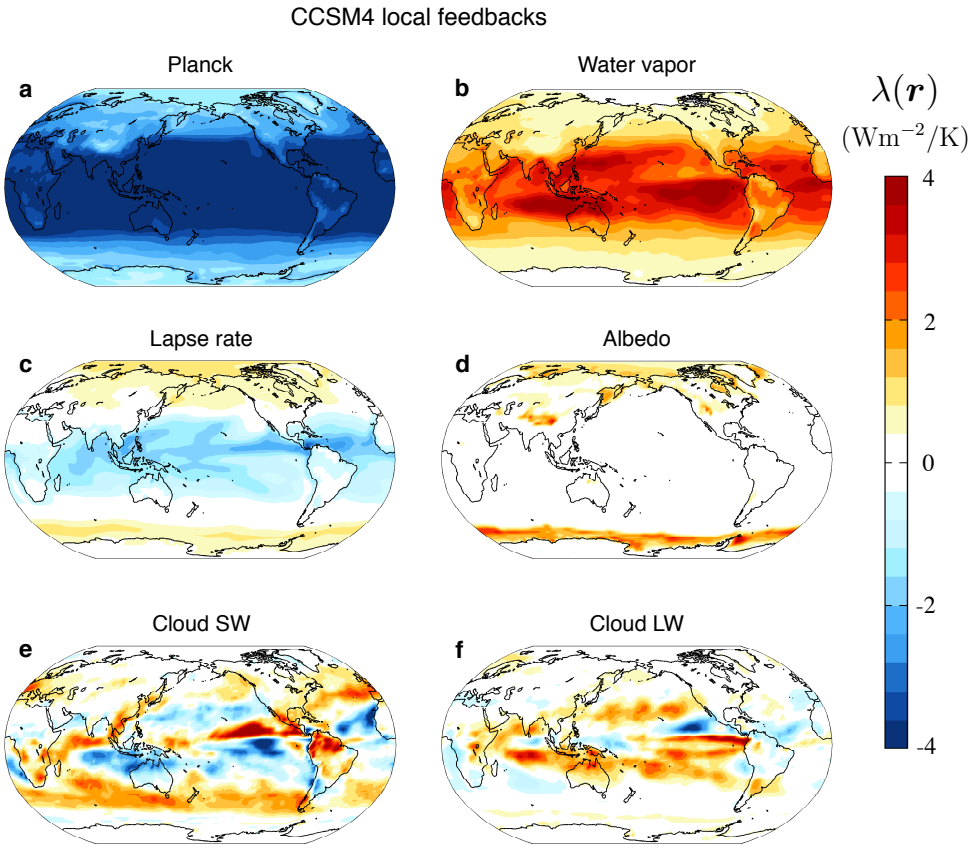

Figure 5.8: Spatial patterns of individual local feedbacks within CCSM4. Local feedbacks (TOA response per degree local surface temperature change) estimated by radiative kernels. **a,** Planck, **b,** water vapor, **c,** lapse rate, **d,** surface albedo, **e,** cloud shortwave, and **f,** cloud longwave feedbacks. Together, these sum to the net local feedback shown in Fig. 5.4.

Chapter 6

CONCLUSIONS

In this thesis we have investigated several topics in physical climatology. In *Chap. 2* we developed a simple model of summer Arctic sea ice area and volume based on the distinct climatological properties of sea ice in the first-year and multiyear age categories, and modified the dynamic-thermodynamic sea ice model CICE to keep an account of first-year (FY) and multiyear (MY) ice types. Several important large-scale sea ice properties, including the sea ice mean state, anomaly persistence timescale, and sensitivity to climate forcing, were shown to be controlled by the partitioning of the total sea ice cover into its FY and MY components.

Based on the above results, we proposed that recent satellite-based observations of Arctic sea ice age [17–24] may offer new insights into large-scale sea ice behavior, and could inform projections of sea ice loss under global warming should global climate models (GCMs) be modified to keep an account of FY and MY ice types individually. In practice, this requires reconciling various estimates of sea ice age derived from a range of observational methods and ice age definitions (see *Chap. 1*).

Since the IPCC Fourth Assessment, the Community Climate System Model version 4 (CCSM4), which uses CICE as its sea ice component, has been modified to trace FY and MY ice. Thus, a critical opportunity is available to validate the sea ice within this model with observed sea ice age characteristics. In future work, we will analyze 20th century and future simulations of sea ice age with CCSM4. In particular, a direct comparison will be made between ice age conditions in CCSM4 (which generates its own Arctic climate and variability) and the observationally-constrained CICE simulation (the 'CICE hindcast') shown in *Chap. 2*. Moreover, analysis of the natural variability of FY and MY ice types in an ensemble of CCSM4 simulations will help to put the recent sea ice age observations in context, and projections of future FY and MY ice conditions over the 21st century will be

made.

In *Chap. 3* we performed a direct test of sea ice reversibility within CCSM3 by increasing atmospheric CO_2 until the Arctic Ocean became ice-free throughout the year and subsequently decreasing it until the initial ice cover returned. The lack of irreversibility or multiple ice-cover states within the model adds to the growing body of evidence suggesting that critical sea ice thresholds, particularly in summer, are unlikely to exist [43,46,47,49,50,121].

We view this work as a step toward the goal of directly assessing sea ice reversibility within a suite of different state-of-the-art coupled GCMs. Since the publication of the work in *Chap. 3*, a similar set of CO_2 ramping experiments were performed within HadCM3 by Ridley *et al.* [173]. Those authors report no evidence of irreversibility under (i) a transient CO_2 ramping scenario similar to the one performed in this thesis and (ii) a scenario where CO_2 is stabilized at its peak for 1000 years before being returned to its initial level. Thus, their results are in good agreement with the work presented here. It would be most useful to see a direct test of sea ice reversibility performed within the ECHAM5 model, which shows hints of critical sea ice threshold behavior during the loss of the winter Arctic ice cover [46].

In *Chap. 4* we quantified the zero-emissions climate commitment—the additional warming that would occur following a cessation of greenhouse gas and aerosol emissions. We found that global temperature would increase rapidly following the elimination of emissions as aerosols are quickly washed from the atmosphere, and that, due to the long atmospheric lifetime of anthropogenic CO_2, global temperature would remain elevated (above pre-industrial levels) for the indefinite future. In this sense, global climate change from anthropogenic greenhouse gas emissions is essentially irreversible on human timescales.

Aerosol radiative forcing was highlighted as the primary uncertainty in observations of the present global energy budget. This was found to imply (i) large uncertainty in the magnitude of forcing increase following the loss of anthropogenic aerosols, and (ii) large uncertainty in global climate sensitivity. Moreover, in order to satisfy strong observational constraints on global surface warming (since pre-industrial) and present ocean heat uptake, climate forcing and climate sensitivity must be inherently linked, wherein strong (weak) aerosol forcing is coupled with high (low) climate sensitivity. Together, these factors were shown to give rise to large uncertainty in both the warming that would occur immediately

following a cessation of emissions, and the long-term climate commitment.

While our focus in this thesis has been on an idealized zero-emissions scenario, the above results apply more generally: under realistic emissions reductions, the loss of aerosols will act to increase global radiative forcing by an uncertain amount, and thus drive a poorly-constrained amount of future warming. Due to the inevitable loss of anthropogenic aerosols under emissions reductions, the level of atmospheric CO_2 that would result in 'safe' climate stabilization must inherently depend on the modern aerosol radiative forcing, and share its considerable uncertainty.

Finally, in *Chap. 5* we showed that the global climate feedback depends directly on the geographic pattern of surface warming through the activation of regional climate feedbacks, and that any variation in the spatial pattern of surface warming necessarily implies time-dependence in the global climate sensitivity to forcing. These findings have important implications for our ability to predict future climate evolution.

The potential for different types of climate change to be governed by distinct global climate feedbacks greatly complicates the comparison of observations from different periods. For instance, the climate response to abrupt forcing changes, such as volcanic eruptions, provides little information about how the global feedback may evolve over long timescales. Likewise, the climate response to very slow forcing changes, such as the orbital and greenhouse gas changes between the Last Glacial Maximum and present day, provides a near-equilibrium measure of global feedback that may have little relevance for transient global warming in the near future. These results call into question Bayesian approaches that assume multiple observations of climate change from different periods can be combined to form narrow bounds on climate sensitivity.

We view the regional feedbacks framework developed here as a step toward a better understanding of climate feedbacks and climate sensitivity within models and nature. Future work will involve the application of regional feedbacks to explain different global feedback time-variations across climate models, particularly under more realistic forcing scenarios. It is hoped is that the quantification of regional feedbacks in terms of local temperature change may ultimately offer insight into those aspects of climate change most relevant for society, namely transient and regional warming over the next few centuries.

BIBLIOGRAPHY

[1] Fetterer F, Knowles K, Meier W and Savoie M (2004, updated 2009) Sea Ice Index. Boulder, CO: National Snow and Ice Data Center. Digital media.

[2] Serreze MC and Francis JA (2006) The Arctic amplification debate. Climatic Change, 76, 241–264.

[3] `http://www.doi.gov/archive/news/08_News_Releases/080514a.html`

[4] `http://alaska.fws.gov/pdf/pb4d.pdf`

[5] Stroeve J, Holland MM, Meier WN, Scambos T and Serreze M (2007) Arctic sea ice decline: Faster than forecast. Geophysical Research Letters, 44, L09501.

[6] Meehl GA, Covey C, Delworth T, Latif M, McAvaney B, et al. (2007) The WCRP CMIP3 multi-model dataset: A new era in climate change research. Bulletin of the American Meteorological Society, 88, 1383–1394.

[7] Meehl GA, Stocker TF, Collins WD, Friedlingstein P, Gaye AT (2007) Global Climate Projections. In: *Climate Change 2007: The Physical Science Basis. Contribution of Working Group I to the Fourth Assessment Report of the Intergovernmental Panel on Climate Change* [Solomon S, Qin D, Manning M, Chen Z, Marquis M, et al. (eds.)]. Cambridge University Press, Cambridge, United Kingdom and New York, NY, USA.

[8] Nakicenovic N, et al. (2000) Special Report on Emissions Scenarios: A Special Report of Working Group III of the Intergovernmental Panel on Climate Change. Cambridge University Press, Cambridge, U.K., 599 pp.

[9] Collins WD, Bitz CM, Blackmon BL, Bonan GB, Bretherton CS, et al. (2006) The Community Climate System Model: CCSM3. Journal of Climate, 19, 2122–2143.

[10] Bitz CM, Holland MM, Hunke EC and Moritz RE (2005) Maintenance of the sea-ice edge. Journal of Climate, 18, 2903–2921.

[11] Blanchard-Wrigglesworth E, Armour KC, Bitz CM and DeWeaver E (2011) Persistence and inherent predictability of Arctic sea ice in a GCM ensemble and observations. Journal of Climate, 24, 231–250.

[12] Kay JE, Holland MM and Jahn A (2011) Inter-annual to multi-decadal Arctic sea ice extent trends in a warming world. Geophysical Research Letters, 38, L15708.

[13] Mahlstein I and Knutti R (2012) September Arctic sea ice predicted to disappear near 2 °C global warming above present. Journal of Geophysical Research, 117, D06104.

[14] Winton M (2011) Do climate models underestimate the sensitivity of Northern Hemisphere sea ice cover? Journal of Climate 24, 3924–3934.

[15] Rothrock DA, Yu Y and Maykut GA (1999) Thinning of the Arctic sea-ice cover. Geophysical Research Letters, 26, 3469–3472.

[16] Rothrock DA, Percival DB and Wensnahan M (2008) The decline in arctic sea-ice thickness: Separating the spatial, annual, and interannual variability in a quarter century of submarine data. Journal of Geophysical Research, 113, C05003.

[17] Kwok R, Cunningham M, Rigor IG, Zwally JH and Yi D (2009) Thinning and volume loss of the Arctic Ocean sea ice cover: 2003–2008. Journal of Geophysical Research, 114, C07005.

[18] Kwok R and Rothrock DA (2009) Decline in Arctic sea ice thickness from submarine and ICESat records: 1958–2008. Geophysical Research Letters, 36, L15501.

[19] Johannessen OM, Shalina EV and Miles MW (1999) Satellite evidence for an arctic sea ice cover in transformation. Science, 286, 1937–1939.

[20] Comiso JC (2002) A rapidly declining perennial sea ice cover in the Arctic. Geophysical Research Letters, 29, 1956.

[21] Comiso JC (2012) Large decadal decline of the Arctic multiyear ice cover. Journal of Climate, 25, 1176–1193.

[22] Nghiem SV, Rigor IG, Perovich DK, Clemente-Colón P, Weatherly JW and Neumann G (2007) Rapid reduction of Arctic perennial sea ice. Geophysical Research Letters, 34, L19504.

[23] Rigor IG and Wallace JM (2004) Variations in the age of Arctic sea-ice and summer sea-ice extent. Geophysical Research Letters, 31, L09401.

[24] Maslanik JA, Fowler C, Stroeve J, Drobot S, Zwally J, Yi D and Emery W (2007) A younger, thinner Arctic ice cover: Increased potential for rapid, extensive sea-ice loss. Geophysical Research Letters, 34, L24501.

[25] Zhang J and Rothrock DA (2003) Modeling global sea ice with a thickness and enthalpy distribution model in generalized curvilinear coordinates. Monthly Weather Review, 131, 845–861.

[26] Hunke EC and Bitz CM (2009) Age characteristics in a multidecadal Arctic sea ice simulation. Journal of Geophysical Research, 114, C08013.

[27] Perovich DK and Polashenski C (2012) Albedo evolution of seasonal Arctic sea ice. Geophysical Research Letters, 39, L08501.

[28] Lindsay RW and Zhang J (2005) The thinning of arctic sea ice, 1988-2003: have we passed a tipping point? Journal of Climate, 18, 4879–4894.

[29] Overpeck JT, Sturm M, Francis JA, Perovich DK, Serreze MC, et al. (2005) Arctic system on trajectory to new, seasonally ice-free state. Eos, Transactions American Geophysical Union, 86, 309.

[30] Serreze MC, Holland MM and Stroeve J (2007) Perspectives on the Arctic's shrinking sea-ice cover. Science, 315, 1533–1536.

[31] Kerr RA (2007) Is battered Arctic sea ice down for the count? Science, 318, 33–34.

[32] Lenton TM and Schellnhuber HJ (2007) Tipping the scales. Nature Reports Climate Change, 1, 97–98.

[33] Lenton TM, Held H, Kriegler E, Hall JW, Lucht W, et al. (2008) Tipping elements in the Earth's climate system. Proceedings of the National Academy of Sciences USA, 105, 1786–1793.

[34] Serreze MC and Stroeve J (2008) Standing on the brink. Nature Reports Climate Change, 2, 142–143.

[35] Ramanathan V and Feng Y (2008) On avoiding dangerous anthropogenic interference with the climate system: Formidable challenges ahead. Proceedings of the National Academy of Sciences USA, 38, 14245–14250.

[36] Lenton TM (2011) Early warning of climate tipping points. Nature Climate Change 1, 201–209.

[37] Lenton TM (2012) Arctic climate tipping points. AMBIO: A Journal of the Human Environment, 41, 10–22.

[38] Wadhams P (2012) Arctic ice cover, ice thickness and tipping points. AMBIO: A Journal of the Human Environment, 41, 23–33.

[39] Duarte C, Lenton TM, Wadhams P and Wassmann P (2012). Abrupt climate change in the Arctic. Nature Climate Change, 2, 60–62.

[40] Budyko MI (1969) The effect of solar radiation variations on the climate of the earth. Tellus, 21, 611–619.

[41] Sellers WD (1969) A global climate model based on the energy balance of the earth–atmosphere system. J Appl Meteor, 8, 392–400.

[42] North GR (1990) Multiple solutions in energy-balance climate models. Global and Planetary Change, 82, 225–235

[43] Eisenman I and Wettlaufer JS (2009) Nonlinear threshold behavior during the loss of Arctic sea ice. Proceedings of the National Academy of Sciences USA, 106, 28–32.

[44] Bitz CM and Roe GH (2004) A mechanism for the high rate of sea-ice thinning in the Arctic Ocean. Journal of Climate, 17, 3622–3631.

[45] Eisenman I (2012) Factors controlling the bifurcation structure of sea ice retreat. Journal of Geophysical Research, 117, D01111.

[46] Winton M (2006) Does the Arctic sea ice have a tipping point? Geophysical Research Letters, 33, L23504.

[47] Winton M (2008) Sea ice-albedo feedback and nonlinear Arctic climate change. In: *Arctic Sea Ice Decline: Observations, Projections, Mechanisms, and Implications*, eds: DeWeaver E, Bitz CM and Tremblay B (American Geophysical Union, Washington DC), Vol 180, pp 111–131.

[48] Ridley J, Lowe J and Simonin D (2008) The demise of Arctic sea ice during stabilisation at high greenhouse gas concentrations. Climate Dynamics, 30, 333–341.

[49] Amstrup SC, DeWeaver E, Douglas DC, Marcot BG, Durner GM, et al. (2010) Greenhouse gas mitigation can reduce sea-ice loss and increase polar bear persistence. Nature, 468, 955–958.

[50] Tietsche S, Notz D, Jungclaus JH and Marotzke J (2011) Recovery mechanisms of Arctic summer sea ice. Geophysical Research Letters, 38, L02707.

[51] Archer D and Brovkin V (2008) Millennial atmospheric lifetime of fossil fuel CO_2. Climatic Change, 90, 283–297.

[52] Archer D (2005) Fate of fossil fuel CO_2 in geologic time. Journal of Geophysical Research, 110, C09S05.

[53] Solomon S, Plattner G-K, Knutti R and Friedlingstein P (2009) Irreversible climate change due to carbon dioxide emissions. Proceedings of the National Academy of Sciences USA, 106, 1704–1709.

[54] Hansen J, Nazarenko L, Ruedy R, Sato M, Willis J, et al. (2005) Earth's energy imbalance: Confirmation and implications. Science, 308, 1431–1435.

[55] Wigley TML (2005) The climate change commitment. Science, 307, 1766–1769.

[56] Meehl GA, Washington WM, Collins WD, Arblaster JM, Hu A, et al. (2005), How much more global warming and sea level rise? Science, 307, 1769–1772.

[57] Held IM, Winton M, Takahashi K, Delworth T, Zeng F and Vallis G (2010) Probing the fast and slow components of global warming by returning abruptly to preindustrial forcing. Journal of Climate, 23, 2418–2427.

[58] Forster P, Ramaswamy V, Artaxo P, Berntsen T, Betts R, et al. (2007) Changes in Atmospheric Constituents and in Radiative Forcing. In: *Climate Change 2007: The Physical Science Basis. Contribution of Working Group I to the Fourth Assessment Report of the Intergovernmental Panel on Climate Change* [Solomon S, Qin D, Manning M, Chen Z, Marquis M, et al. (eds.)]. Cambridge University Press, Cambridge, United Kingdom and New York, NY, USA.

[59] Plattner G-K, Knutti R, Joos F, Stocker TF, von Bloh W, et al. (2008) Long-term climate commitments projected with climate-carbon cycle models. Journal of Climate, 21, 2721–2751.

[60] Matthews HD and Weaver AJ (2010) Committed climate warming. Nature Geoscience, 3, 142–143.

[61] Roe GH (2008) Feedbacks, timescales, and seeing red. Annual Review of Earth and Planetary Sciences, 37, 93–115.

[62] Cess RD (1975) Global climate change: An investigation of atmospheric feedback mechanisms. Tellus, 27, 193–198.

[63] Hansen J, Lacis A, Rind D, Russell G, Stone P, et al. (1984) Climate sensitivity: Analysis of feedback mechanisms. In: *Climate Processes and Climate Sensitivity*, Geophys Monogr, 29, American Geophysical Union, 130–163.

[64] Schlesinger ME (1985) Feedback analysis of results from energy balance and radiative-convective models. In: *The Potential Climatic Effects of Increasing Carbon Dioxide*, DOE/ER-0237, eds: MacCracken MC and Luther FM, U.S. Department of Energy, 280–319.

[65] Bony S, Colman R, Kattsov VM, Allan RP, Bretherton CS, et al. (2006) How well do we understand and evaluate climate change feedback processes? Journal of Climate, 19, 3445–3482.

[66] Hansen J, Lacis A, Ruedy R, Sato M and Wilson H (1993) How sensitive is the world's climate? Research and Exploration, 9,142–158.

[67] Allen MR, Andranova N, Booth B, Dessai S, Frame D, et al. (2007) Observational constraints on climate sensitivity. In: *Avoiding Dangerous Climate Change*, eds: Schellnhuber HJ, et al. (Cambridge Univ. Press), pp 281–289.

[68] Edwards TL, Crucifix M and Harrison SP (2007) Using the past to constrain the future: how the palaeorecord can improve estimates of global warming. Progress in Physical Geography, 31, 481–500.

[69] Kohler P, Bintanja R, Fischer H, Joos F, Knutti R, et al. (2010) What caused Earth's temperature variations during the last 800,000 years? Data-based evidence on radiative forcing and constraints on climate sensitivity. Quaternary Science Reviews, 29, 129–145.

[70] Wigley TML, Ammann CM, Santer BD and Raper SCB (2005) Effect of climate sensitivity on the response to volcanic forcing. Journal of Geophysical Research, 110, D09107.

[71] Hegerl GC, Zwiers FW, Braconnot P, Gillett NP, Luo Y, et al. (2007) Understanding and Attributing Climate Change. In: *Climate Change 2007: The Physical Science Basis. Contribution of Working Group I to the Fourth Assessment Report of the Intergovernmental Panel on Climate Change* [Solomon S, Qin D, Manning M, Chen Z, Marquis M, et al. (eds.)]. Cambridge University Press, Cambridge, United Kingdom and New York, NY, USA.

[72] Knutti R and Hegerl GC (2008) The equilibrium sensitivity of the Earth's temperature to radiation changes. Nature Geoscience, 1, 735–743.

[73] Myhre G, Highwood EJ, Shine KP, Stordal F (1998) New estimates of radiative forcing due to well mixed greenhouse gases. Geophysical Research Letters, 25, 2715–2718.

[74] Roe GH and Baker MB (2007) Why is climate sensitivity so unpredictable? Science, 26, 629–632.

[75] Soden BJ and Held IM (2006) An assessment of climate feedbacks in coupled ocean-atmosphere models. Journal of Climate, 19, 3354–3360.

[76] Shell KM, Kiehl JT, Shields CA (2008) Using the radiative kernel technique to calculate climate feedbacks in NCAR's Community Atmospheric Model. Journal of Climate, 21, 2269–2282.

[77] Colman R (2003) A comparison of climate feedbacks in GCMs. Climate Dynamics, 20, 865–873.

[78] Soden BJ, Held IM, Colman R, Shell IM, Kiehl JT and Shields CA (2008) Quantifying climate feedbacks using radiative kernels. Journal of Climate, 21, 3504–3520.

[79] Held IM and Shell KM (2012) Using relative humidity as a state variable in climate feedback analysis. Journal of Climate, 25, 2578–2582.

[80] Jonko AK, Shell KM, Sanderson BM and Danabasoglu G (2012) Climate feedbacks in CCSM3 under changing CO_2 forcing. Part I: Adapting the linear radiative kernel technique to feedback calculations for a broad range of forcings. Journal of Climate, doi:10.1175/JCLI-D-11-00524.1, in press.

[81] Feldl N and Roe GH (2012) Do feedbacks work? In prep.

[82] Hall A, Qu X (2006) Using the current seasonal cycle to constrain snow albedo feedback in future climate change. Geophysical Research Letters, 33, L03502.

[83] Flanner MG, Shell KM, Barlage M, Perovich DK and Tschudi MA (2011) Radiative forcing and albedo feedback from the Northern Hemisphere cryosphere between 1979 and 2008. Nature Geoscience, 4, 151–155.

[84] Levitus S, Antonov JI, Wang J, Delworth TL, Dixon KW, Broccoli AJ (2001) Anthropogenic warming of Earth's climate system. Science 292, 267–270.

[85] Hansen J, Sato M, Rudy R, Nazarenko L, Lacis A, et al. (2005) Efficacy of climate forcings. Journal of Geophysical Research, 110, D18104.

[86] Hansen J, Sato M and Ruedy R (1997) Radiative forcing and climate response. Journal of Geophysical Research, 102, 6831–6864.

[87] Yoshimori M and Broccoli AJ (2008) Equilibrium response of an atmosphere–mixed layer ocean model to different radiative forcing agents: Global and zonal mean response. Journal of Climate, 21, 4399–4423.

[88] Boer G and Yu B (2003) Climate sensitivity and climate state. Climate Dynamics, 21, 167–176.

[89] Colman R, Power SB and McAvaney BJ (1997) Non-linear climate feedback analysis in an atmospheric general circulation model. Climate Dynamics, 13, 717–731.

[90] Crucifix M (2006) Does the Last Glacial Maximum constrain climate sensitivity? Geophysical Research Letters, 33, L18701.

[91] Hewitt CD and Mitchell JFB (1997) Radiative forcing and response of a GCM to ice age boundary conditions: Cloud feedback and climate sensitivity. Climate Dynamics, 13, 821–834.

[92] Wetherald RT and Manabe S (1975) The effects of changing the solar constant on the climate of a general circulation model. Journal of Atmospheric Science, 32, 2044–2059.

[93] Colman R and McAvaney BJ (2009) Climate feedbacks under a very broad range of forcing. Geophysical Research Letters, 36, L01702.

[94] Yoshimori M, Hargreaves JC, Annan JD, Yokohata T and Abe-Ouchi A (2011) Dependency of feedbacks on forcing and climate state in physics parameter ensembles. Journal of Climate, 24, 6440–6455.

[95] Roe GH and Armour KC (2011) How sensitive is climate sensitivity? Geophysical Research Letters, 38, L14708.

[96] Meier WN, Stoeve J and Fetterer F (2007) Whither Arctic sea ice? A clear signal of decline regionally, seasonally, and extending beyond the satellite record. Annals of Glaciology, 46, 428–434.

[97] Deser C and Teng H (2008) Recent trends in Arctic sea ice and the evolving role of atmospheric circulation forcing, 1979-2007, In: *Arctic Sea Ice Decline: Observations, Projections, Mechanisms, and Implications*, eds DeWeaver E, Bitz CM and Tremblay B (American Geophysical Union, Washington DC), Vol. 180, pp 7–26.

[98] Hansen J, Russel G, Lacis A, Fung I, Rind D and Stone P (1985) Climate response times: Dependence on climate sensitivity and ocean mixing. Science, 229, 857–859.

[99] von Storch H and Zwiers FW (1999) *Statistical Analysis in Climate Research*. Cambridge University Press, Cambridge, 484 pp.

[100] Hunke EC and Lipscomb WH (2008) CICE: The Los Alamos Sea Ice Model, Documentation and Software User's Manual, version 4.0. Tech. Rep. LA-CC-06-012, Los Alamos National Laboratory, Los Alamos, New Mexico.

[101] Large W and Yeager S (2004) Diurnal to decadal global forcing for ocean and sea-ice models: The data sets and flux climatologies. NCAR Tech. Note NCAR/TN-460+STR, CGD Division of the National Center for Atmospheric Research.

[102] Bitz CM, Gent PR, Woodgate RA, Holland MM and Lindsay R (2006) The influence of sea ice on ocean heat uptake in response to increasing CO_2. Journal of Climate, 19, 2437–2450.

[103] Holland MM, Bitz CM, Hunke EC, Lipscomb WH and Schramm JL (2006) Influence of the sea ice thickness distribution on polar climate in CCSM3. Journal of Climate, 19, 2398–2414.

[104] Goosse H, Arzel O, Bitz CM, de Montety A and Vancoppenolle M (2009) Increased variability of the Arctic summer ice extent in a warmer climate. Geophysical Research Letters, 36, L23702.

[105] Holland MM, Bitz CM, Tremblay B and Bailey DA (2008) The role of natural versus forced change in future rapid summer Arctic ice loss. In: *Arctic Sea Ice Decline: Observations, Projections, Mechanisms, and Implications*. eds: DeWeaver E, Bitz CM and Tremblay B (American Geophysical Union, Washington DC), Vol 180, 133–150.

[106] Bitz CM, Battisti DS, Moritz RE and Beesley JA (1996) Low-frequency variability in the Arctic atmosphere, sea ice, and upper-ocean climate system. Journal of Climate, 9, 394–408.

[107] L'Heveder B and Houssais MN (2001) Investigating the variability of the arctic sea ice thickness in response to a stochastic thermodynamic atmospheric forcing. Climate Dynamics, 17, 107–125.

[108] Gregory JM, Stott PA, Cresswell DJ, Rayner NA, Gordon C and Sexton DMH (2002) Recent and future changes in Arctic sea ice simulated by the HadCM3 AOGCM. Geophysical Research Letters, 29, 2175.

[109] Flato GM (1994) Spatial and temporal variability of Arctic ice thickness. Annals of Glaciology, 21, 323–329.

[110] Holland MM, Bitz CM and Tremblay B (2006) Future abrupt reductions in the summer Arctic sea ice. Geophysical Research Letters, 33, L23503.

[111] Holland MM, Bitz CM, Hunke EC, Lipscomb WH and Schramm JL (2006) Influence of the Sea Ice Thickness Distribution on Polar Climate in CCSM3. Journal of Climate, 19, 2398–2414.

[112] Eisenman I, Schneider T, Battisti DS and Bitz CM (2011) Consistent changes in the sea ice seasonal cycle in response to global warming. Journal of Climate, 24, 5325–5335.

[113] Meier W, Fetterer F, Knowles K, Savoie M, Brodzik MJ (2006, updated quarterly) Sea ice concentrations from Nimbus-7 SMMR and DMSP SSM/I passive microwave data, 1979–2010. Boulder, Colorado USA: National Snow and Ice Data Center. Digital media.

[114] Hansen J, Ruedy R, Sato M and Lo K (2010) Global surface temperature change. Reviews of Geophysics, 48, RG4004.

[115] Stouffer RJ (2004) Time scales of climate response. Journal of Climate, 17, 209–217.

[116] Eisenman I (2010) Geographic muting of changes in the Arctic sea ice cover. Geophysical Research Letters, 37, L16501.

[117] Marotzke J and Botzet M (2007) Present-day and ice-covered equilibrium states in a comprehensive climate model. Geophysical Research Letters, 34, L16704.

[118] Rose BEJ and Marshall J (2009) Ocean heat transport, sea ice, and multiple climate states: Insights from energy balance models. Journal of Atmospheric Science, 66, 2828–2843.

[119] Holland MM, Bailey DA, Vavrus S (2010) Inherent sea ice predictability in the rapidly changing Arctic environment of the Community Climate System Model, version 3. Climate Dynamics, 36, 1239–1253.

[120] Scheffer M, Bascompte J, Brock WA, Brovkin V, Carpenter SR, et al. (2009) Early-warning signals for critical transitions. Nature, 46, 53–59.

[121] Notz D (2009) The future of ice sheets and sea ice: Between reversible retreat and unstoppable loss. Proceedings of the National Academy of Sciences USA, 106, 20,590–20,595.

[122] Hansen J, Sato M, Kharecha P, Beerling D, Masson-Delmotte V, et al. (2009) Target atmospheric CO_2: Where should humanity aim? Open Atmospheric Science Journal, 2, 217–231.

[123] Hansen J, Sato M, Ruedy R, Kharecha P, Lacis A, et al. (2007) Dangerous human-made interference with climate: a GISS modelE study. Atmospheric Chemistry and Physics, 7, 2287–2312.

[124] Baker MB and Roe GH (2009) The shape of things to come: Why is climate change so predictable? Journal of Climate, 22, 4574–4589.

[125] Hoffert MI, Callegari AJ and Hsieh C-T (1980) The role of deep sea heat storage in the secular response to climatic forcing. Journal of Geophysical Research, 85, 6667–6679.

[126] Wigley TML and Schlesinger ME (1985) Analytical solution for the effect of increasing CO_2 on global mean temperature. Nature, 315, 649–652.

[127] Wigley TML and Raper SCB (1990) On the natural variability of the climate system and detection of the greenhouse effect. Nature, 344, 324–327.

[128] Lindzen RS and Giannitsis C (1998) On the climatic implications of volcanic cooling. Journal of Geophysical Research, 103, 5929–5941.

[129] Raper SCB, Gregory JM and Osborn TJ (2001) Use of an upwelling-diffusion energy balance climate model to simulate and diagnose A/OGCM results. Climate Dynamics, 17, 601–613.

[130] Kiehl JT (2007) Twentieth century climate model response and climate sensitivity. Geophysical Research Letters, 34, L22710.

[131] Schwartz SE, Charlson RJ and Rodhe H (2007) Quantifying climate change—too rosy a picture? Nature Reports Climate Change, 2, 23–24.

[132] Knutti R (2008) Why are climate models reproducing the observed global surface warming so well? Geophysical Research Letters, 35, L18704.

[133] Hare B and Meinshausen M (2006) How much warming are we committed to and how much can be avoided? Climatic Change, 75, 111–149.

[134] Knutti R (2010) The end of model democracy? Climatic Change, 102, 395–404.

[135] Frame DJ, Booth BBB, Kettleborough JA, Stainforth DA, Gregory JM, et al. (2005) Constraining climate forecasts: The role of prior assumptions. Geophysical Research Letters, 32, L09702.

[136] Gregory JM (2000) Vertical heat transports in the ocean and their effect on time-dependent climate change. Climate Dynamics, 16, 501–515.

[137] Winton M, Takahashi K and Held IM (2010) Importance of ocean heat uptake efficacy to transient climate change. Journal of Climate, 23, 2333–2344.

[138] Trenberth KE, Jones PD, Ambenje P, Bojariu R, Easterling D, et al. (2007) Observations: Surface and Atmospheric Climate Change. In: *Climate Change 2007: The Physical Science Basis. Contribution of Working Group I to the Fourth Assessment Report of the Intergovernmental Panel on Climate Change* [Solomon S, Qin D, Manning M, Chen Z, Marquis M, et al. (eds.)]. Cambridge University Press, Cambridge, United Kingdom and New York, NY, USA.

[139] Lyman JM, Good SA, Gouretski VV, Ishii M, Johnson GC, et al. (2010), Robust warming of the global upper ocean. Nature, 465, 334–337.

[140] Purkey SG and Johnson GC (2010) Warming of global abyssal and deep southern ocean waters between the 1990s and 2000s: Contributions to global heat and sea level rise budgets. Journal of Climate, 23, 6336–6351.

[141] Isaksen ISA, Granier C, Myhre G, Berntsen TK, Dalsoren SB, et al. (2009) Atmospheric composition change: Climate-chemistry interactions. Atmospheric Environment, 43, 5138–5192.

[142] Huybers P (2010) Compensation between model feedbacks and curtailment of climate sensitivity. Journal of Climate, 23, 3009–3018.

[143] Knutti R, Stocker TF, Joos F, Plattner G-K (2002) Constraints on radiative forcing and future climate change from observations and climate model ensembles. Nature, 416, 719–723.

[144] Wigley TML and Raper SCB (2001) Interpretation of high projections for global-mean warming. Science, 293, 451–454.

[145] Raper SCB, Gregory JM and Stouffer RJ (2002) The role of climate sensitivity and ocean heat uptake on AOGCM transient temperature response. Journal of Climate, 15, 124–130.

[146] Murphy JM (1995) Transient response of the Hadley Centre coupled ocean–atmosphere model to increasing carbon dioxide. Part 1: Control climate and flux adjustment. Journal of Climate, 8, 36–56.

[147] Bitz CM, Shell KM, Gent PR, Bailey DA, Danabasoglu G, et al. (2012) Climate Sensitivity in the Community Climate System Model, Version 4. Journal of Climate, 25, 3053–3070.

[148] Senior CA and Mitchell JFB (2000) Time-dependence of climate sensitivity. Geophysical Research Letters 27, 2685–2688.

[149] Watterson IG (2000) Interpretation of simulated global warming using a simple model. Journal of Climate, 13, 202–215.

[150] Gregory JM, Ingram WJ, Palmer MA, Jones GS, Stott PA, et al. (2004) A new method for diagnosing radiative forcing and climate sensitivity. Geophysical Research Letters, 31, L03205.

[151] Kiehl JT, Shields CA, Hack JJ and Collins WD (2006) The climate sensitivity of the Community Climate System Model Version 3 (CCSM3). Journal of Climate, 19, 2584–2596.

[152] Williams KD, Ingram WJ and Gregory JM (2008) Time variation of effective climate sensitivity in GCMs. Journal of Climate, 21, 5076–5090.

[153] Li C, von Storch J-S and Marotzke J (2012), Deep-ocean heat uptake and equilibrium climate response. Climate Dynamics, doi: 10.1007/s00382-012-1350-z, in press.

[154] Gregory JM and Webb MJ (2008) Tropospheric adjustment induces a cloud component in CO_2 forcing. Journal of Climate, 21, 58–71.

[155] Andrews T and Forster PM (2008) CO_2 forcing induces semi-direct effects with consequences for climate feedback interpretations. Geophysical Research Letters, 35, L04802.

[156] Colman RA and McAvaney BJ (2011) On tropospheric adjustment to forcing and climate feedbacks. Climate Dynamics 36, 16491658.

[157] Andrews T, Gregory JM, Forster PM and Webb MJ (2012) Cloud adjustment and its role in CO_2 radiative forcing and climate sensitivity: A review. Surveys in Geophysics, doi: 10.1007/s10712-011-9152-0.

[158] Webb MJ, Lambert FH and Gregory JM (2012) Origins of differences in climate sensitivity, forcing and feedback in climate models. Climate Dynamics, doi: 10.1007/s00382-012-1336-x.

[159] Gent PR, Danabasoglu G, Donner LJ, Holland MM, Hunke EC, et al. (2011) The Community Climate System Model, Version 4. Journal of Climate, 24, 4973–4991.

[160] Manabe S, Stouffer RJ, Spelman MJ and Bryan K (1991) Transient response of a coupled atmosphere–ocean model to gradual changes of atmospheric CO_2. Part I: Annual mean response. Journal of Climate, 4, 785–818.

[161] Kirkman C and Bitz CM (2011) The effect of the sea ice freshwater flux on Southern Ocean temperatures in CCSM3: Deep ocean warming and delayed surface warming. Journal of Climate, 24, 2224–2237.

[162] Holland MM and CM Bitz (2003) Polar amplification of climate change in the coupled model intercomparison project. Climate Dynamics, 21, 221–232.

[163] Bates JR (2007) Some considerations of the concept of climate feedback. Quarterly Journal of the Royal Meteorological Society, 133, 545–560.

[164] Bates JR (2012) Climate stability and sensitivity in some simple conceptual models. Climate Dynamics, 38, 455–473.

[165] Andrews T, Gregory JM, Webb MJ and Taylor KE (2012) Forcing, feedbacks and climate sensitivity in CMIP5 coupled atmosphere–ocean climate models. Geophysical Research Letters, 39, L09712.

[166] Forster PMD and Taylor KE (2006) Climate forcings and climate sensitivities diagnosed from coupled climate model integrations. Journal of Climate, 19, 6181–6194.

[167] Boer GJ (2011) The ratio of land to ocean temperature change under global warming. Climate Dynamics, 37, 2253–2270.

[168] Forster PMD and Gregory JM (2006) Diagnosing the climate sensitivity and its components from Earth Radiation Budget data. Journal of Climate, 19, 39–52.

[169] Murphy DM, Solomon S, Portmann RW, Rosenlof KH and Forster PM (2009) An observationally based energy balance for the Earth since 1950. Journal of Geophysical Research, 114, D17107.

[170] Shine KP, Cook J, Highwood EJ, Joshi MM (2003) An alternative to radiative forcing for estimating the relative importance of climate change mechanisms. Geophysical Research Letters, 30, 2047.

[171] Zelinka MD and Hartmann DL (2012) Climate feedbacks and their implications for poleward energy flux changes in a warming climate. Journal of Climate, 25, 608–624.

[172] Annan JD and Hargreaves JC (2006) Using multiple observationally-based constraints to estimate climate sensitivity. Geophysical Research Letters, 33, L06704.

[173] Ridley JK, Lowe JA and Hewitt HT (2012) How reversible is sea ice loss? The Cryosphere, 6, 193–198.

VITA

Kyle Armour grew up in San Diego, California. After completing degrees in Physics and Mathematics at the University of California, San Diego in 2005, he moved to Seattle, Washington to attend graduate school. There he studied particle physics for several years under the advisement of Dr. Stephen Ellis; conducted extensive field work on snow and ice dynamics for several years under the direction of Master Robert Hahn; and, upon retiring from skiing and mountaineering, studied the physics of sea ice and climate for several years under the guidance of Drs. LuAnne Thompson, Cecilia Bitz and Gerard Roe. In 2012 he graduated with a Doctor of Philosophy in Physics from the University of Washington, Seattle.